Title
Spatial and Color Vision in the Absence of Retinal Motion

Author
Boehm, Alexandra Elizabeth

Publication Date
2019

Peer reviewed|Thesis/dissertation

Spatial and Color Vision in the Absence of Retinal Motion

By

Alexandra Elizabeth Boehm

A dissertation submitted in partial satisfaction of the

requirements for the degree of

Doctor of Philosophy

in

Vision Science

in the

Graduate Division

of the

University of California, Berkeley

Committee in charge:

Professor Austin Roorda
Professor Dennis M. Levi
Professor Richard Ivry

Spring 2019

Spatial and Color Vision in the Absence of Retinal Motion

by Alexandra Elizabeth Boehm

Abstract

Spatial and Color Vision in the Absence of Retinal Motion

by

Alexandra Elizabeth Boehm

Doctor of Philosophy in Vision Science

University of California, Berkeley

Professor Austin Roorda, Chair

In the mid-19th century, Johannes Peter Müller first proposed what has become known as the law of specific nerve energies, where sensory perception is understood in the context of underlying physiological mechanisms which create an internal representation of an external stimulus. In the *Handbuch der Physiologie des Menschen für Vorlesungen* he wrote, "Sensation is not the conduction of a quality of state of external bodies to consciousness, but the conduction of a quality or state of our nerves to consciousness, excited by an external cause," (translated by Clarke & O'Malley, 1996). While it has long been appreciated that visual perception and the underlying physiology are inextricably linked, scientific research has been limited in its ability to provide direct comparisons between the two. Perception is the culmination of multiple levels of neural processing involving millions of cells, but physiological models are often limited to data from a single or few cells in nonhuman primates. In contrast, what we know about perception has largely been gathered from psychophysical experiments performed in humans, where behavior is quantified and related to controlled differences in external stimuli, but the underlying physiological mechanisms can only be inferred.

For vision, this is further complicated by the fact that the eye is constantly in motion. Even when fixated, the eye makes microscopic eye movements which cause light from a stationary stimulus to be moved across many light-sensitive cells on the retina, and consequently across many receptive fields of downstream neurons. Recent advances in optics and eye tracking technology have made it possible to perform psychophysical experiments in human observers with cellular resolution where stimuli are fixed on the retina even in the presence of eye motion. This has brought about a new generation of experiments attempting to unify physiology and behavior. The work described here utilizes and expands upon these methodologies toward a better understanding of color and spatial vision in the absence of retinal motion. Chapter 1 provides a background on the origins of color and spatial vision in the retina, in addition to a review of the methodology. Chapter 2 explores the spatial extent of desensitization to stabilized stimuli and compares this to the known constraints to spatial vision imposed by anatomy and physiology. Chapter 3 expands upon previous work, looking at the contribution of individual cone photoreceptors to color vision, toward the construction of physiologically relevant color space from multiple cone-targeted stimulation. Finally, Chapter 4 demonstrates novel methodology to compensate for stimulus motion on the retina that is due to dynamic changes in transverse chromatic aberration.

Dedication

This thesis is dedicated with love and affection to Steven Edward Boehm
(November 20, 1951 – February 14, 2013)
Loving father, lifetime scholar, and best friend.

Table of Contents

List of Figures

List of Abbreviations

AO	Adaptive optics
AOM	Acousto-optic modulator
AOSLO	Adaptive optics scanning laser ophthalmoscope
Arcmin(s)	Arcminutes
a.u.	Arbitrary units
CMOS	Complementary metal oxide semiconductor
Deg(s)	Degree(s)
d’	d-prime, a sensitivity index
Eq.	Equation
FFT	Fast Fourier transform
FOV	Field of view
FPGA	Field programmable gate array
FPS	Frames per second
FWHM	Full width at half maximum
GCL	Ganglion cell layer (of the retina)
Hz	Hertz
IR	Infrared
ISI	Inter-stimulus-interval
INL	Inner nuclear layer (of the retina)
IPL	Inner plexiform layer (of the retina)
LCA	Longitudinal chromatic aberration
LGN	Lateral Geniculate Nucleus
L-cone	Long-wavelength sensitive cone
logTD	log Trolands
OFF	Off-center type cell
ON	On-center type cell
ONL	Outer nuclear layer (of the retina)
OPL	Outer plexiform layer (of the retina)
RMS	Root mean squared
SNR	Signal-to-noise ratio
M-cone	Medium-wavelength sensitive cone
ms	Millisecond(s)
ND	Neutral density
PMT	Photomultiplier tube
S-cone	Short-wavelength sensitive cone
SLD	Super luminescent diode
SLO	Scanning laser ophthalmoscope
SLR	Stimulus location recovery
SPA	Stimulus placement accuracy
TCA	Transverse chromatic aberration
TSLO	Tracking scanning laser ophthalmoscope

Acknowledgements

I was once told that success often has more to do with luck than skill. If I have any luck at all, it is mostly to do with the people I have been fortunate enough to encounter during my scholarly activities. Any humble success I might have is undoubtedly their due.

Foremost, I would like to thank my graduate mentor, Professor Austin Roorda, for his continued support during my graduate studies. There are many lessons I will keep from my time as Austin's student. Particularly, his ingenuity in technological advancement and commitment to both clinical and basic science applications demonstrated to me the importance of keeping an eye on the bigger picture, a valuable lesson for those of us who spend so much time fixated on small-spot stimuli. I would be fortunate to achieve even a fraction of his success in my own career.

Appreciation is also due to the members of my committee, Professors Dennis Levi and Richard Ivry, for their feedback and time taken in review of this document. A special thank you to Dennis who provided much insight during the conception and interpretation of the work presented in Chapter 2.

I would also like to thank my faculty advisor, Dr. Christine Wildsoet, whom I have often looked to as a role model for addressing the challenges faced by women in science.

A special thank you is also due to my undergraduate research mentor, Professor Donald MacLeod, for his cultivation and support of my naive interests in vision science. The work I participated in while under his mentorship provided the inspiration behind many of the experiments presented here. I'd also like to express my heartfelt gratitude for the mentorship I received from Drs. Jenny Bosten (now a professor at University of Sussex) and Alan Robinson, who were both postdocs in the MacLeod lab at the time.

I would like to acknowledge specifically a few of the collaborators I worked closely with as a graduate student, Drs. Christy Sheehy, Claudio Privitera, and Brian Schmidt. A special thanks is required for Brian. Without his keen scientific and technical abilities, much of the work in this dissertation would not have been possible.

Thank you to the other members of the Roorda lab, past and present, who have offered their support both intellectually and personally, including Kavitha Ratnam, Sanam Mozaffari, Ethan Bensinger, Kat Foote, Swati Bhargava, Norick Bowers, Taras Litvin, Francesco LaRocca, Volker Jaedicke, Will Tuten, Ram Sabesan, Natalie Stepien, Nicolas Bensaid, Brandon Lujan, and Jim Ma. A most enthusiastic thank you to Pavan Tiruveedhula for his patience and technical support.

I am also very grateful to my closest friends for their support, Vanessa Christensen, Francine Reid, Courtney Monfort, Kelly Byrne, Cecile Fortuny, Katie Tregillus, Vasha Dutell, Dar Dahlen, Yves Lamson (the littlest hobo) and Monk (the littlest doggo).

Finally, I would like to thank my family for always offering love and encouragement, especially to my stepfather, Michael Marquardt, my aunt, Phyllis Crow, my cousin Carson Ballou, and most of all, to my mother, Melinda Boehm Marquardt. Mom, thank you for teaching me about rainbows. None of this would be possible without you.

Chapter 1. Introduction

The visual system's reconstruction of the physical world relies on complex neural processes which transform the retinal image, a map of light intensities projected on the back of the eye, to units of space, color and time. Vision begins in the retina where light signals are transduced to electrical potentials. These signals travel through the retina, lateral geniculate nucleus (LGN), and finally to the visual cortex, where the images from the two eyes are combined and further processed by later visual areas. Along the way, neural mechanisms transform the visual representation as it exists at the photoreceptors into a rich, meaningful percept.

Most of what is known about the physiological underpinnings of human perception has been inferred from primate studies. This is because the methodologies used to identify cell types and their corresponding functional roles are invasive and not suitable for human subjects. Still, visual psychophysics, which seeks to quantitatively relate behavior to light stimuli, has found reasonable success in relating known primate physiology to human perception, though many questions about how neural mechanisms relate to perception remain unanswered. This is in part due to the technical difficulty of performing psychophysical experiments at the fine spatial scale required to access cellular function.

The optical quality of the human eye precludes single-cell stimulation near the fovea, arguably the most important area of the retina for human vision. Here photoreceptor cells are densely packed, and light is blurred across multiple adjacent receptors. Additionally, fixational eye motion, which occurs even when the eye is steadily fixated, moves a stimulus across multiple photoreceptors. Recent advancements in high-resolution retinal imaging and eye tracking have made it possible, for the first time, to simultaneously image, track and present stabilized stimuli to the retina, making it possible to probe visual function at a cellular scale. This has brought about a new wave of perceptual experiments with the goal of measuring psychophysical behavior at the level of individual cells, with the hope that a more direct relationship between perception and low-level physiology can be established.

This dissertation is focused around the study of spatial and color vision, two areas particularly important in human vision with their origins in the low-level visual system. The first section of this chapter provides a brief review of the known circuitry sustaining color and spatial vision, with a focus on the low-level mechanisms which impose the fundamental limits to chromatic discrimination and spatial resolution in the human visual system. Section 1.2 provides a review of the technologies supporting psychophysical experimentation at a cellular scale, the same techniques utilized in the experiments presented in the remaining chapters of this dissertation.

1.1 Basic Low-Level Circuitry Sustaining Color and Spatial Vision

Vision begins in the retina, the light sensitive tissue at the back of the eye, where photons of light are captured by photoreceptor cells. There are two classes of photoreceptors, rods and cones. The rods vastly outnumber the cones, with a typical human retina containing 92 million rod photoreceptors and about 4.8 million cones (Curcio et al., 1990). The rod photoreceptors are highly sensitive and support vision at low light levels, whereas

cones are most sensitive at daylight levels. There are three types of cone photoreceptors in the human retina sensitive to short (S), medium (M) and long (L) wavelengths of the light, which, as discussed in more detail below, provide the basis for human trichromatic color vision. There is only one type of rod photoreceptor. Figure 1.1 shows relative absorbance spectra for the four types of photoreceptor. The spectral absorbance functions for each photoreceptor type are broad and overlap with one another, such that no wavelength elicits activity in only a single receptor type.

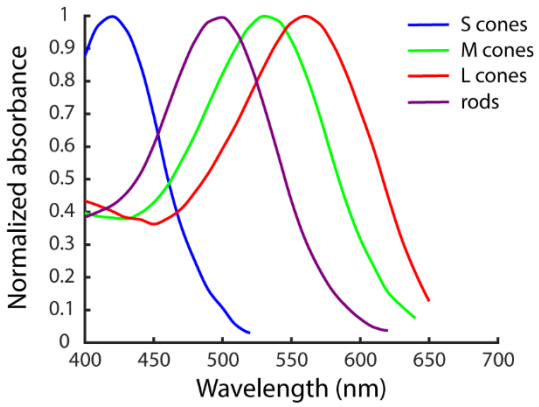

Figure 1.1. Normalized absorbance spectra for cone and rod photoreceptors. Rod photoreceptors are most sensitive at low light levels and support night vision. There is only one type of rod cell; therefore, night vision is monochromatic (colorblind). Cone photoreceptors are most sensitive at daylight levels. There are three types of cone photoreceptors, sensitive to short (S), medium (M) and long (L) wavelengths of light, which provide the basis for trichromatic color vision in humans. (Data are from Dartnall et al. (1983) and obtained from cvlr.org).

The topography of photoreceptor cells is not uniform across the retina (Curcio et al., 1990). Cone photoreceptors are densely packed in the fovea, the central 2 degrees (deg) of the retina that corresponds to fixation, and this area is devoid of rods. At greater eccentricities, rods make up an increasingly greater percentage of the cell density. Figure 1.2 shows images taken with an adaptive optics scanning laser ophthalmoscope (AOSLO), an optical imaging instrument which is used to take high-resolution images of the living human retina, described in more detail in the following section. The insets show normalized images at the foveal center and 6 deg, highlighting the changes in cell topography from the fovea to the near periphery. In the periphery, tiny rod cells can be seen surrounding the cones which are much larger and less densely packed than in the fovea. The high sampling density of the cones, lack of rods, and avascularity of the fovea make it optimal for high spatial vision.

Only 5-6% of all cones are S-cones, while L- and M-cones make up the other 95% in ratios varying between individuals, although there are typically more L- than M-cones (Roorda & Williams, 1999; Hofer et al., 2005a). There is also variation in spectral topography of the cone mosaic across the retina. The L- and M-cones appear to be mostly randomly arranged in the mosaic, with some evidence of clumping near the fovea. The S-cones are more regularly but sparsely spaced (Roorda & Williams, 1999; Hofer et al., 2005a). they do not exist in the very center of the fovea, but are at peak density in a ring around the foveal center (Curcio et al., 1991).

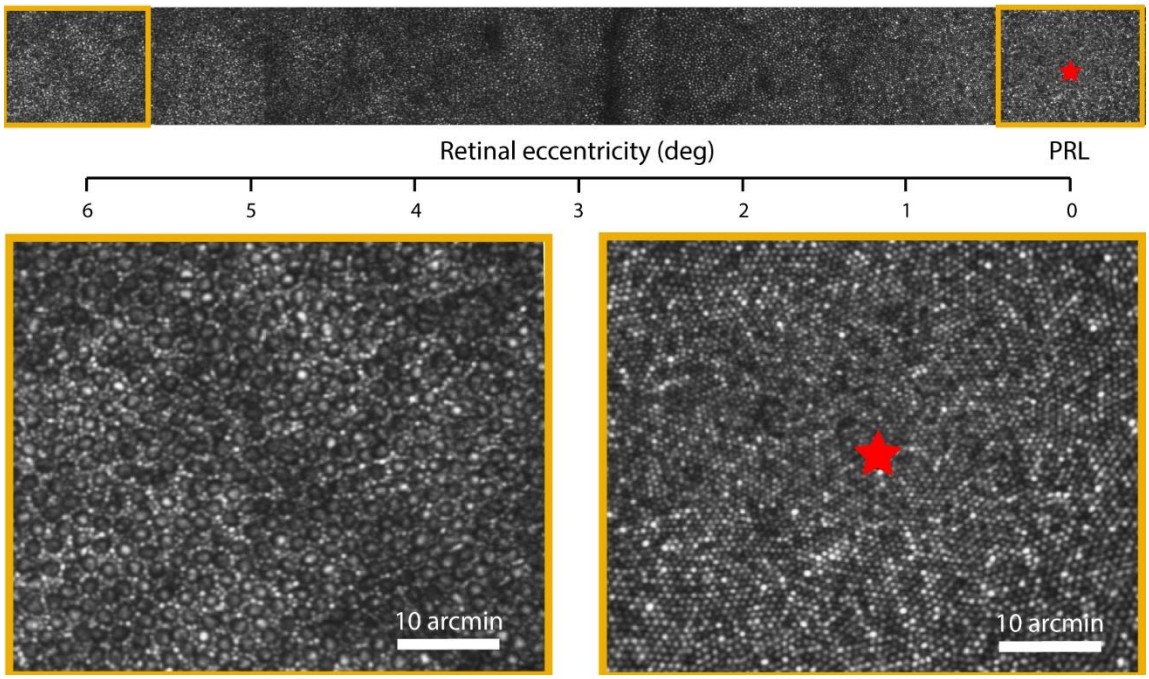

Figure 1.2. Photoreceptor mosaic (fovea to 6 deg) along the temporal retinal meridian. Retinal eccentricity is defined here as the angular distance on the retina from the preferred retinal locus (PRL), where we constantly direct our gaze for central vision. Images were taken with an AOSLO (described in more detail in the following section). The top row is a series of normalized images taken along the temporal retinal meridian and stitched together. The right-hand inset shows the foveal center, with the PRL indicated by the red star. Note the high packing density of the foveal cones, providing the basis for high spatial acuity vision. In the left inset is an image at 6 deg, where the larger cells are cone photoreceptors, and the smaller cells forming rings around the cones are rod photoreceptors. Additionally, retinal vasculature can be seen in the darker regions at 6 deg, which appears in the image because light is absorbed by blood vessels as it passes through the retinal tissue to the photoreceptor layer at the very back of the retina. Note the absence of vasculature and rods in the fovea. (Subject 20076R).

The retina is made up of multiple cell layers, with the photoreceptors oriented at the backmost layer. This means that light traveling through the eye on its way to the photoreceptors must pass through several layers of transparent neural tissue before reaching the receptors. The schematic in Figure 1.3 shows the basic organization of the retina. The outer nuclear layer (ONL) contains the photoreceptor cell bodies. The synaptic terminals of the photoreceptors are found in the outer plexiform layer (OPL), in addition to the dendrites of horizontal and bipolar cells, whose cell bodies are found in the inner nuclear layer (INL) of the retina, in addition to the cell bodies of some amacrine cells. The axon terminals of the bipolar cells are found in the inner plexiform layer (IPL). Also present in the IPL are the dendrites of the retinal ganglion cells, which have synaptic connections to the bipolar cells. The IPL is organized in several sublayers, with the different types of ganglion cells (described in more detail below) stratifying at different sublevels. Finally, the ganglion cell bodies are found in the ganglion cell layer (GCL). Their axons travel along the nerve fiber layer of the retina to form the optic nerve.

The functional organization of the retina includes both feedforward and lateral processing mechanisms, achieved by the synaptic connections within and between retinal layers. The basic feedforward organization is as follows: The photoreceptors synapse to

bipolar cells, which synapse unto the retinal ganglion cells. The collection of cones that are synaptically connected to a downstream ganglion cell via bipolar cells comprises the center of the ganglion cell receptive field.

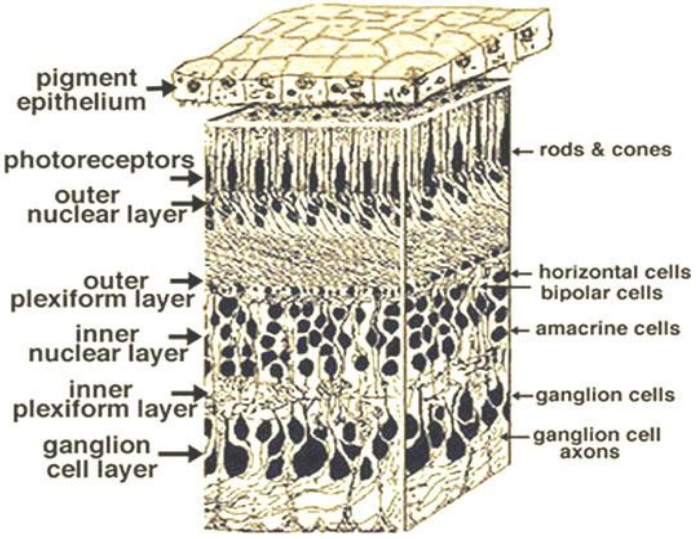

Figure 1.3. Basic cell architecture of the retina. The retina is shown here as a three-dimensional block section, with the photoreceptors at the top. Light would enter from the bottom in this illustration, passing through several layers of cells before reaching the rods and cones in the photoreceptor layer at the very back of the retina. (From *Webvision,* http://webvision.med.utah.edu/, Creative Commons License: Attribution, Noncommercial 4.0 International (CC BY-NC)).

The receptive fields of these cells have center-surround antagonistic organization (Kuffler, 1953), drawing either excitatory (ON cell) or inhibitory (OFF cell) input directly from their cone to bipolar cell connections with the opposing signal from the surround (Schiller, 1992). The ON cell types stratify in the inner portion of the IPL, and the OFF types in the outer portion (Famiglietti & Kolb, 1976). As we will see later in this section, the receptive field characteristics of the different types of ganglion cells provide the basic structure of chromatic, luminance, and spatial input to later brain regions.

Lateral connections in the retina fall broadly under three categories: gap junctions (electrical coupling between photoreceptors), horizontal cell contacts between cones and downstream neurons, and amacrine cell connections between bipolar and/or ganglion cells. Gap junctions exist between neighboring L- and M-cone photoreceptors, while these junctions only rarely include S-cones (Tsukamoto, et al., 1992; O'Brien et al., 2004; Massey 2008). Gap junctions may have functional consequences for vision, for example, by increasing luminance sensitivity or decreasing red-versus-green chromatic sensitivity (Hornstein et al., 2004).

In addition to gap junctions, lateral connections between photoreceptors are found in the horizontal cells, which provide inhibitory feedback in order to regulate receptor sensitivity to varying light levels. In general, horizontal cells fall into two types known as H1 and H2 cells. These cells have cone-specific wirings, but are not spectrally opponent (Dacey et al., 1996; Kolb & Nelson, 1995). H1 cells generally make dense contacts exclusively with L- and M-cones. The H2 cells directly contact S-cones, and have sparser connections with the L- and M-cones. The specificity of H1 and H2 cell connections with

the three cone types implies a functional role in color vision. For example, it is believed that the inhibitory feedback to L- and M-cones by the H1 horizontal cells is responsible for the surround opponency in midget retinal ganglion cells, with midget bipolar cells already displaying opponency (Crook et al., 2011).

Amacrine cells in the IPL interact with bipolar and retinal ganglion cells. There are several different types of amacrine cells with a variety of functional purposes, but, importantly, they may have a role in forming the surrounds of the larger, diffuse bipolar cells (Dacey et al., 2000).

The functional architecture is set up to form the receptive fields of retinal ganglion cells through feedforward connections of cones to bipolar and retinal ganglion cells, and the lateral connections which modify the signals at each level. Hartline (1938) first used the term “receptive field” to describe the area of the retina which corresponds to changes in a single retinal neuron’s firing rate. Their specific center-surround spatial structures were later identified by Kuffler (1953). Since then much work has been done to characterize the different retinal ganglion cell types and identify their functional roles in visual processing.

There are many types of retinal ganglion cells, with 15 to 20 distinct types identified in the primate retina (Gollisch & Meister, 2010; Rhoades et al., 2018). Of these, about 75% are ON or OFF midget, ON or OFF parasol, or small bistratified retinal ganglion cells. They project to functionally distinct subdivisions of the lateral geniculate nucleus of the thalamus (Hubel & Wiesel, 1972), the so-called parvocellular, magnocellular and koniocellular layers, respectively (Kaplan, 2004), which operate in parallel to relay information via the LGN to area V1 in the cortex (Shapley, 1990; Chatterjee & Callaway, 2003). These cells have been studied most extensively, and they are believed to provide the vast majority of input to the later visual system, being particularly important in chromatic, luminance, and spatial processing.

The magnocellular pathway is often implicated in luminance perception, though it plays roles in other visual processes as well (e.g., motion perception, though this is controversial; Merigan et al., 1991). The parasol retinal ganglion cells, comprising approximately 10% of all retinal ganglion cells (Dacey, 2000), have large receptive fields characterized by their large dendritic arbors (Dacey & Peterson, 1992) and spatial response properties (Dacey et al., 2000), collecting the input of many cone photoreceptors through synapses to diffuse bipolar cells (Boycott & Wässle, 1991). They are thought to have predominantly L- and M-cone inputs and very weak, if any, S-cone input (Lee & Grünert, 2007; Field et al., 2010).

The chromatic visual system is believed to be subserved by the parvo- and koniocellular pathways, with their origins in the retina (Dacey, 1993). The midget retinal ganglion cells draw their center input from the midget bipolar cells, which are connected to a single L- or M-cone throughout the central retina and near periphery. The midget retinal ganglion cell surround signal is modified by horizontal and amacrine cells, although their surround inputs do not appear to be selective with regard to L- or M-cone type (Dacey et al., 1996; Calkins & Sterling, 1996; Crook et al., 2011). L-ON cells are excited by L-cone activity in their center and have inhibitory surrounds. L-OFF cells are inhibited by L-cone activity in their center and have excitatory surrounds. Similarly, there are M-ON and M-OFF cell types. Together, the spectrally opponent behavior of these cells is

thought to provide the basis for red-versus-green color vision through formation of the parvocellular pathway (Shapley & Perry, 1986; Dacey, 1993).

An analogous origin for blue-versus-yellow opponency of the koniocellular pathway has also been established in the retina. An S-ON bipolar cell was originally identified in the primate retina, with its selective cone contacts matching the known sparse density of S-cones (Mariani, 1984; Kouyama & Marshak, 1992). The small bistratified ganglion cell, with characteristics of blue/yellow spectral opponency (Dacey & Lee, 1994), has been shown to contact S-cones through their connections to the S-ON bipolars (Calkins et al., 1998; Herr et al., 2003). It has also been proposed that the H2 horizontal cells, with their strong contacts to S-cones and weaker connections to L- and M-cones, may be involved in the formation of an inhibitory surround mechanism for the blue/yellow opponent system (Dacey, 2000).

Additionally, the surround mechanism of S-cones may be mediated by inhibitory contacts between diffuse bipolar cells (which contact L- and M-cones almost exclusively) and the small bistratified cells (De Valois et al., 2000). For a long time, the origin of a corresponding S-OFF pathway in the retina remained elusive, but it has recently been shown that an S-cone selective OFF pathway may exist through connections of S-cones to OFF midget bipolar cells (Klug et al., 2003; Field et al., 2010; Dacey et al., 2017; Wool et al., 2018).

The spectral opponency achieved by the retinal processes described in the above paragraphs is preserved in the LGN (De Valois et al., 1966), where the signals inherited from the midget and small bistratified cells in the retina remain functionally segregated in the respective parvocellular and koniocellular pathways. Similarly, signals from parasol retinal ganglion cells project to the distinct magnocellular pathway of the LGN. Together, the three pathways operate in parallel to relay information about color and luminance to the visual cortex (Shapley, 1990; Chatterjee & Callaway, 2003).

Much work has been done toward the representation of color in a physiologically relevant coordinate space where stimuli of any color or luminance are represented as discrete points in three dimensions, with axes corresponding to red-versus-green (L-M), blue-versus-yellow (S-L+M), and dark-versus-light (L+M). These are derived from the known spectral sensitivities of human cone photoreceptors, often called the cone fundamentals (e.g., Smith & Pokorny, 1975; Stockman et al., 1993; Stockman, et al., 1999; Stockman & Sharpe, 2000), which differ from direct estimates of pigment absorbance spectra (shown in Figure 1.1) in that they represent light at the cornea, prior to the spectral filtering by the lens and macular pigment, and they depend on photoreceptor optical density (relating to the amount of pigment available in the cell).

Because individuals vary in these aspects, a different set of cone fundamentals may be useful for different observers, although standard observer estimates are used in most experimental situations. Additionally, there are changes in macular pigment density and optical density of the photoreceptors at different retinal eccentricities, which are corrected for by employing a different set (2 or 10 degree) of cone fundamentals.

With knowledge of the cone fundamentals, stimuli can be represented in a cone excitation space, where the color of any light is expressed as the relative S-, M- and L-cone activities in response to the stimulus. The post-receptoral representation of color is captured by defining specific planes in this space. The MacLeod-Boynton chromaticity diagram (1979), for example, is shown in Figure 1.4B, where equiluminance in cone

excitation space is found along any plane where the sum of L- and M-cone activity is constant (since S-cones contribute very little, if at all, to luminance perception). The cardinal axes in this space, L/(L+M) and S/(L+M), represent the two chromatic mechanisms, red-versus-green (by comparison of L-cone activity to the combined activity of L- and M-cones) and blue-versus-yellow (by comparisons of S-cone activity to the activity of L- and M-cones). An extension of this space in three dimensions is shown in Figure 1.4A, where the third axis, L+M, defines luminance, and any orthogonal plane represents equiluminance (Krauskopf et al., 1982; Derrington et al., 1984). DKL space has the additional benefit of representing changes in chromaticity and luminance relative to the adapted state, with an arbitrary white point at the origin, with any deviation from this point representing the corresponding change in one or more of the post-receptoral processes.

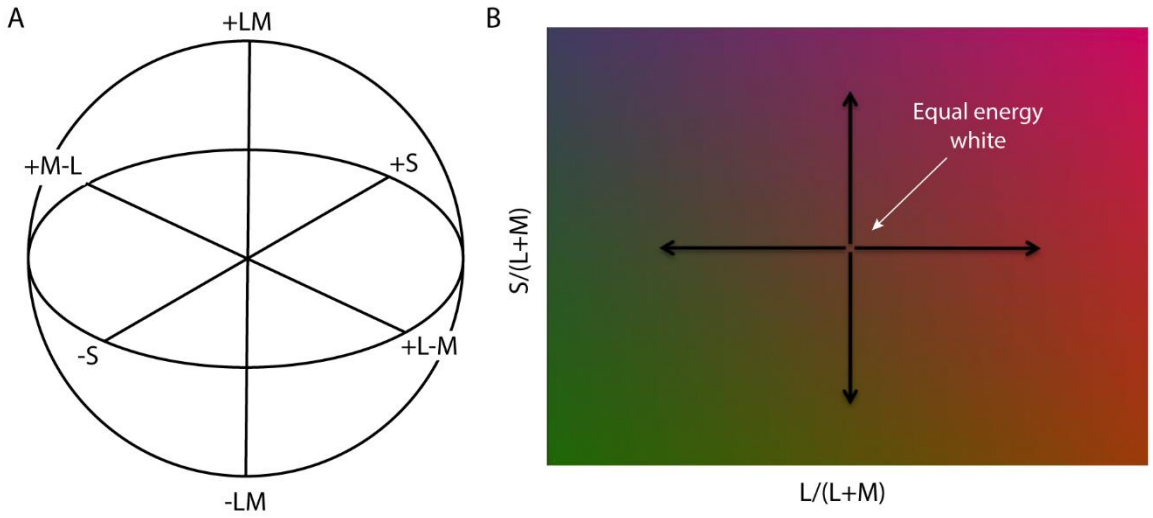

Figure 1.4. Physiologically relevant color space. Panel A shows a three-dimensional color space, known as DKL space, where chromaticity and luminance are specified as comparisons of the three cone types, S, M, and L. Luminance (+LM/-LM), red-versus-green (+L-M or +M-L) and blue-versus-yellow (+/-S), correspond to the proposed mechanisms of the distinct magnocellular, parvocellular and koniocellular pathways of the LGN, respectively (Krauskopf et al., 1982; Derrington et al., 1984). DKL color space is based on the MacLeod-Boynton chromaticity diagram (1979) shown in Panel B. The chromaticity diagram represents a plane in cone excitation space where L+M (luminance) activity is constant; thus, the cardinal axes correspond to changes in L-versus-M or S-cone activity with constant luminance. It is believed that modulating activity along a single axis in this space (L+M, L/(L+M) or S/(L+M)) relative to the background chromaticity isolates function in the corresponding (magnocellular, parvocellular or koniocellular) pathway. In this example, modulations relative to equal energy white (flat spectrum) in the horizontal or vertical directions correspond to chromaticity changes perceived as red-versus-green and chartreuse-versus-violet. (Though this is typically referred to as the “blue/yellow” axis.)

The representation of color in this way predicts the spectral tuning of low-level visual neurons in the retina and LGN (Derrington et al., 1984), in addition to showing special status in chromatic discrimination (e.g., Boynton & Kambe, 1980; Krauskopf et al., 1982; Krauskopf & Gegenfurtner, 1992; Miyahara et al., 1993; Yeh et al., 1993; Smith & Pokorny, 1995). In general, V1 neurons do not exhibit the same preferential tuning to the cardinal color directions (Lennie et al., 1990; Johnson et al., 2004; Horwitz et al.,

2007). Cardinal tuning of a few cells has been revealed through nonlinear considerations of their cone inputs (Horwitz & Hass, 2012), but near detection threshold V1 neurons do not reveal the special status of the supposed cardinal mechanisms (Hass & Horwitz, 2013). The close relationship between measures of chromatic discrimination and the spectral tuning characteristics of neurons in the retina and LGN suggests the ability to probe these low-level mechanisms behaviorally.

The majority of the visual signal as it exists at the retinal output is formed through the receptive field structures of the cell types described above, providing a spatial mapping of photoreceptors to visual field locations. The retinotopic organization is preserved throughout much of the visual hierarchy. The seminal work of Hubel and Wiesel (1959-1968) showed that receptive fields become increasingly complex at higher visual areas. Despite this increasing complexity of the representation of the visual signal, human psychophysics has been directly associated with low-level primate physiology, most often in the macaque monkey (e.g., Kalloniatis & Harwerth, 1991; Lee et al., 1989), a species known to have a visual system similar to that of humans with a fully developed fovea, a characteristic not found, for example, in rodent models.

The fovea is particularly important for human spatial vision. The dense packing of L- and M-cone photoreceptors, absence of rods, and avascularity of the fovea, as shown in Figure 1.2, make it optimal for high spatial vision. To preserve the highest spatial detail afforded by the photoreceptor sampling, minimal convergence to downstream receptive fields would seem a reasonable goal for the involved post-receptoral processes. The midget retinal ganglion cells have the smallest receptive fields in the retina (De Monasterio & Gouras, 1975; Dacey, 1993), and in the fovea, it is believed that these cells have 1:1 connections with cone photoreceptors through the midget bipolar cells. This is often referred to as the “private-line” hypothesis. The complex and dense anatomy of the fovea, where photoreceptors are densely packed and displaced laterally from their connecting inner retinal neurons, makes direct observations of the wiring between foveal cones and ganglion cells difficult with conventional techniques (Drasdo et al., 2007). Support for the private-line hypothesis is typically found indirectly by cell density and displacement estimates (for example, see Ahmad et al., 2003), and there are conflicting reports from anatomy as to how far the 1:1 relationship between cones and midget retinal ganglion cells extends beyond the central fovea.

For example, Dacey performed intracellular tracer injections of midget cells, and by examination of their dendritic field diameters, he inferred a 1:1 relationship between cones and midget retinal ganglion cells as far as 6 deg from the foveal center (Dacey, 1993). Kolb and Marshak (2003) reconstructed foveal connections with electron microscopy to view directly the synaptic connections between midget bipolars and ganglion cells. Surprisingly, they found that the OFF-type cells had a 1:1 relationship with bipolars, but ON-type cells shared the input of two or sometimes three bipolars. In the parafovea, all cells displayed a 1:1 relationship. The discrepancy in wiring patterns between the central fovea and parafovea has been attributed to crowding of neurons and neuropil in the central fovea (Kolb, 2012). A recent study using block-face electron microscopy traced the foveal wiring scheme of a single donor retina, and found both convergence (more than one cone connecting to downstream neurons) and divergence (one cone connection to more than one downstream neuron), suggesting that foveal organization may be more complicated than originally presumed (Dacey, 2018). However,

the retina was from a prematurely born donor, and thus it remains unclear whether such a wiring pattern is typical of the fully developed human fovea.

Whether, or to what extent, the 1:1 relationship between cones and midget ganglion cells exists in the fovea is still an open topic of debate, but it is generally understood that outside of the fovea, receptive field size increases linearly as a function of eccentricity due to the greater convergence between cones, bipolars, and ganglion cells in the peripheral retina. Much work has been done to demonstrate the close relationship between fine spatial resolution across the visual field (e.g., grating acuity) and the sampling density of the midget retinal ganglion cells across the peripheral retina (e.g., Thibos et al., 1987a; Williams & Coletta, 1987; Wilkinson et al., 2016), indicating that these cells provide the bottleneck to spatial sampling at the output of the retina.

The work reviewed in the previous paragraphs represents the combined efforts of anatomists, physiologists and psychophysicists toward bridging the gaps in understanding the relationship between low-level neural circuitry, physiology and perception. Though many of the details were omitted, this research relied on the development of clever techniques to overcome the many hurdles to single-cell investigation. Efforts to relate function in single neural units to perceptual phenomena are particularly daunting due to the difficulty of probing vision with the precise spatial control required to access cellular function. Interference fringes, for example, have been used to project stimuli directly to the retina, bypassing the eye's optics to present stimuli at the high resolution required to match, or even exceed, the neural sampling limit (e.g., Green, 1970; Enoch & Hope, 1973; Williams, 1985a and 1985b; Williams & Coletta, 1987; Thibos et al., 1987a and 1987b; McMahon et al., 2000; Wilkinson et al., 2016).

Additionally, numerous techniques have been employed to compensate for fixational eye motion, which occurs even when the eye is steadily fixated, in order to investigate visual mechanisms in the absence of retinal motion (e.g., Yarbus, 1954 and 1967; Ditchburn & Ginsborg, 1952; Riggs et al., 1953; Kelly, 1979; Poletti et al., 2013). In the last decade, advances in adaptive optics and tracking scanning laser ophthalmoscopy have made it possible to perform behavioral experiments with precisely controlled stimuli, overcoming the challenges of optical blur and eye motion and allowing for more direct investigations of visual mechanisms at the cellular level. The following section of this chapter reviews the technologies supporting this work.

1.2 Methodology for Controlling Optical Quality and Stabilization of Small-Spot Stimuli on the Retina

There are several hurdles to investigating the behavioral correlates of perception with cellular resolution. These fall broadly into two categories, challenges introduced by the optical quality of the human eye (Liang & Williams, 1997) and challenges due to fixational eye motion (Martinez-Conde et al., 2004). Much work has been done over the last decades to overcome the hurdles to stabilization of optically controlled stimuli on the human retina. When the proper techniques are employed, psychophysical experiments can now be performed at the resolution of single cone photoreceptors (Harmening et al., 2014; Sabesan et al., 2016; Tuten et al., 2017; Schmidt et al., 2018a and 2018b; Schmidt et al., 2019). The recently developed technologies supporting this work are described below.

The optical quality of the human eye is poor. Before light reaches the retina, it travels through the components of the anterior eye: the lens, cornea and vitreous fluid. In the emmetropic eye, light is focused by the optics of the eye to a point on the retina, but if light is instead focused to a plane either in front of or behind the retina, it will be blurred. This is typically due to mismatch between the eye's optics and its axial length, which position the retina outside of the focal plane of the eye, and results in the most common forms of optical disorder (Hyman, 2007), myopia and hyperopia. Myopia is often referred to as "nearsightedness," a condition where light from a distant object is blurred on the retina. Hyperopia, or "farsightedness," describes the condition where light from near objects is blurred. Astigmatism, due to irregularities in the shape of the cornea or lens, is another common form of degradation of optical quality (Read et al., 2007). Uncorrected astigmatism causes light to be blurred both in front of and behind the retina, and results in blurry vision for both near and far distance viewing. These forms of ocular aberration can be corrected with external lenses prescribed by an optician.

Defocus and astigmatism account for the majority of blur caused by optical imperfections, and are known as lower-order aberrations. Ever after correction for lower-order aberrations, higher-order aberrations further blur the image on the retina, but usually by an amount unnoticeable for human vision (Liang & Williams, 1997). Optical imaging of the living retina, however, requires higher resolution. The resolution of a retinal image will depend on both the optical quality of the imaging system and the optical quality of the eye, with the aberrations of the eye precluding single-cell resolution in the fovea where photoreceptor cells are most densely packed.

In order to correct for blur introduced by higher-order aberrations, the effect of these imperfections on retinal image quality must first be measured. The aberrations can be described as the deviations from a planar wavefront, where all light rays travel in parallel (i.e., a flat wavefront). When collimated light enters the eye, the rays of light become distorted. The wavefront of light back-reflected from the retina can be used to characterize the aberrations of the eye. In high-resolution optical imaging systems, this is done with a Shack-Hartmann wavefront sensor (Platt & Shack, 2001), consisting of a tiny array of lenslets, with equal focal length, which focus the light reflected back from the retina to a light sensor. The position of each focused spot on the sensor can then be used to measure local distortions in the wavefront.

With knowledge of the wavefront function, optical correction for higher-order aberrations can be achieved with a deformable mirror, which consists of a reflective surface supported by an array of actuators. The deformable mirror dynamically updates its shape based on real-time wavefront measurements in a closed-loop system. This is known as adaptive optics (AO), a technique first introduced in in the field of astronomy in order to correct for wavefront aberrations caused by atmospheric distortions (Hardy et al., 1977). AO was first used for retinal imaging in 1989 by Dreher et al., but it wasn't until 1997, after the development of the Shack-Hartmann wavefront sensor, that AO was implemented in a closed-loop system with a flood-illuminated ophthalmoscope (Liang et al., 1997). The higher numerical aperture afforded by a dilated pupil increases the angular resolution that can be achieved in a diffraction-limited optical system, and with the use of adaptive optics, retinal imaging could now be performed over a large pupil without compromising optical quality. This provided the first high-resolution images

of the human photoreceptor mosaic *in vivo*. Roorda & Williams (1999) used AO imaging techniques combined with retinal densitometry, revealing for the first time the spectral mosaic of L-, M- and S-cones in the human retina. Additionally, presenting visual stimuli with AO correction and the observation of improved performance in visual tasks demonstrated that the optical quality of the eye could be improved in ways that were meaningful for vision, particularly high spatial vision (Liang et al., 1997; Yoon & Williams, 2002).

AO was later integrated into a scanning laser ophthalmoscope (SLO) by Roorda et al. (2002), the advantage being that SLOs (Webb et al., 1980; Webb & Hughes, 1981), in comparison to flood illuminated systems, attained higher contrast images through the use of a scanning laser source and confocal pinhole (Webb et al., 1987), which increased the efficiency of light collection and improved resolution axially by rejection of light from retinal layers not of interest. The implementation of AO in a scanning laser ophthalmoscope further increased axial resolution by removing the effects of aberrations over the fully dilated pupil. Additionally, the scanning nature of the system, where the light source is scanned point by point on the retina to form an image over time, increased the rate of image acquisition sufficiently for real-time stabilization of the acquired images (Arathorn et al., 2007; Yang et al., 2010) which would otherwise introduce distortions in the image to be removed post hoc (e.g., Vogel et al., 2006; Stevenson et al., 2010).

Real-time motion estimation was the final step toward delivery of stabilized retinal stimuli in the SLO when a single wavelength is used. The relevant algorithms and methodologies for stimulus stabilization in the SLO are detailed in Arathorn et al. (2007) and Yang et al. (2010), and will be described briefly here.

AOSLO systems are equipped with fast and slow scanning mirrors which raster scan the light source on the retina. The frame rate of the AOSLO is limited by the slow galvo scanner, which operates at 30 Hz. Motion estimation from the acquired images, however, can operate at a much faster rate using strip-based algorithms (Mulligan, 1998; Stevenson et al., 2010). In this method, distortions in the image caused by fixational eye motion are recovered by cross-correlation of individual strips of each frame as they are acquired to a reference frame using an FFT-based algorithm. The lateral (x and y) displacements between strips and the reference frame caused by eye motion can then be used to generate stabilized videos of the retina in real time (Arathorn et al., 2007; Yang et al., 2010). This is achieved with a custom field programmable gate array (FPGA; Xilinx, San Jose, CA) board, which enables immediate strip acquisition.

Real-time eye motion traces allow for stimuli to be targeted to identified retinal locations in the reference frame. The latency between prediction and stimulus delivery is 2-3 milliseconds (Yang et al., 2010; Sheehy et al., 2012), with any eye motion occurring during this period resulting in displacements from the targeted retinal location. Stimulus placement accuracy was measured experimentally in the AOSLO and found to be 0.15 arcmin (Yang et al., 2010). Of course, this is dependent on the spatial sampling frequency of each pixel in the retinal image in addition to strip size, and can vary between systems. For example, Sheehy et al. (2012) introduced a tracking SLO without adaptive optics which employed the same stabilization and targeted stimulus delivery described above. With a smaller aperture than is typically used in the AOSLO (i.e., a

restricted pupil), this system is capable of resolving cones in the peripheral retina where cells are larger and packing is less dense. The larger field of view (3-10 deg) used in the TSLO, in comparison with the 1 to 2 deg field typical of AOSLO systems, results in lower pixel sampling and, therefore, a larger error in stabilization accuracy. In the peripheral retina, where neural sampling is coarser, this system may be sufficient for behavioral testing at cellular resolution.

The breadth of work described in the previous paragraphs has culminated in the ability to stabilize stimuli to the retina with unprecedented accuracy (for comparison of various stabilization techniques, see Table 1 in Sheehy et al., 2012). Additionally, the simultaneous retinal imaging, tracking, and stimulus delivery capabilities of these systems offers numerous benefits for psychophysical experimentation, making these investigations possible at a cellular scale. However, one final consideration, that of chromatic aberration, is required for retinal stimulation in the complete absence of stimulus motion on the retina.

Chromatic aberrations occur because the optical elements of the eye vary in refractive power for different wavelengths of light, a consequence of chromatic dispersion (Thibos et al., 1992). These are distinct from monochromatic aberrations, which are mostly independent of wavelength (Marcos et al., 1999; Fernández et al., 2005) and are present even after adaptive optics correction. There are two types of chromatic aberration, longitudinal chromatic aberration (LCA) and transverse chromatic aberration (TCA). LCA manifests as a difference in focus between wavelengths, and TCA as a lateral displacement in the imaging plane.

In multiwavelength SLO systems, infrared (IR) wavelengths are typically used for retinal imaging and visible wavelengths in the 500-700 nm range are used for retinal stimulation. LCA is corrected for by adjustment of the source vergences (Grieve et al., 2006; Harmening et al., 2012). Because LCA varies little between individuals, a fixed vergence adjustment between wavelengths is sufficient to account for differences in the eye's refraction with wavelength (Atchison & Smith, 2005). Using one wavelength as the reference, the expected difference in refraction is calculated for each wavelength channel. A model eye is then used to simulate an equal and opposite refractive state by positioning of the retina within the model eye. The vergence of each source at its point of entry to the AOSLO system is then adjusted to focus the scanning beam on the model retina. The position of the confocal pinholes in the respective light detection path are then adjusted to optimize the images obtained with each wavelength.

Unlike LCA, TCA varies substantially between individuals (Simonet & Campbell, 1990; Rynders et al., 1995; Marcos et al., 1999 and 2001) and therefore cannot be corrected by alignment of the various wavelengths in the system. Instead, the lateral offsets between images acquired with the different wavelengths are estimated by cross-correlation, and the targeted stimulus position is updated to incorporate the estimated image offsets (Harmening et al., 2012). Using these techniques, psychophysical experiments have been performed at single cell resolution, shown quantitatively by Harmening et al., 2014. However, TCA varies with pupil position when stimuli are viewed through an external limiting aperture (Simonet & Campbell, 1990; Thibos et al., 1990 and 1992), and may vary as much as 3-4 arcminutes per millimeter pupil displacement (Harmening et al., 2014; Privitera et al., 2016; Boehm et al., 2019). Thus cellular resolution is typically only achieved in practiced observers using a bite bar to

minimize head movements. In Chapter 4, we introduce novel methods for compensation of TCA in the presence of pupil displacements.

To summarize, much work in the past decades has been successful in overcoming the various obstacles associated with retinally targeted, optically controlled stimulus delivery. When the appropriate techniques are used to overcome blur from the eye's optics and uncertainties in stimulus placement due to eye motion and TCA, cellular resolution can be achieved for behavioral experimentation.

1.3 Why Study Spatial and Color Vision in the Absence of Retinal Motion?

Given that fixational eye motion is natural to vision, and may even impart some functional benefit (Poletti et al., 2013; Ratnam et al., 2017), it is reasonable to question the scientific value of studying two integral parts of visual perception, spatial and color vision, in the absence of retinal motion. With that consideration in mind, the role of fixational eye motion in these areas remains mostly unknown. Even if data acquired in the absence of retinal motion are not representative of visual perception under more natural viewing conditions, they may inform us about the role that fixational eye motion plays in supporting these mechanisms. This was elegantly demonstrated by Ratnam et al., (2017), who measured spatial acuity under various conditions of retinal motion and stabilization, showing that acuity improves with fixational eye motion.

Secondly, the lower-level representation of the visual signal exists in units of receptive fields which may sample for one or only a few cone photoreceptors (as described in Section 1.1 of this chapter), making it difficult to assess the functional roles of post-receptoral circuits in the human visual system with conventional techniques. Revealing the behavioral correlates of low-level circuitry will provide a better understanding of how the visual system performs computations on discrete samples of space and light intensity in order to reconstruct a rich, multidimensional percept. For example, Tuten and colleagues (2017) recently showed that thresholds for individual cone photoreceptors against different chromatic adapting backgrounds were consistent with cone type, but were also influenced by the local spectral topography of the cone mosaic. Modeling of their results in comparison with known horizontal cell anatomy and physiology revealed estimates of horizontal cell receptive fields in the living human retina, emphasizing the potential of these methodologies for investigation of post-receptoral neural circuits and, most importantly, their behavioral consequences (Kling et al., 2019).

Chapter 2. The Spatial Extent of Desensitization to Stabilized Stimuli in the Periphery

2.1 Abstract

Fixational eye motion, which describes the ever-present microscopic movement of the eye, traverses a stimulus across many photoreceptor cells in the retina, even when the eye is steadily fixated on a target. When a stimulus is stabilized to the retina under abnormal viewing conditions, it fades completely from perception. It is generally thought that fading is due to adaptation of post-receptoral neurons which become habituated to static stimuli. Interestingly, stimuli that are stabilized in retinal space but modulated in intensity over time, i.e., flickered or pulsed stimuli, also fade and result in large reductions in visual sensitivity.

We hypothesized that the spatial extent of desensitization might reflect the spatial characteristics of the receptive fields of the adapted post-receptoral mechanism. To investigate this, we used a scanning laser ophthalmoscope to simultaneously image, track and deliver stabilized stimuli to the retina. With precise spatial control of our stimuli, we measured the spatial extent of desensitization on the retina. We found that the areas of desensitization extended beyond the local area where the stimulus was delivered. Though larger than the stimulus area, the areas of desensitization were small, and sensitivity increased sharply at their borders. These characteristics were roughly consistent with the receptive fields of midget retinal ganglion cells at the eccentricities tested (6-10 deg). Taken together, these observations are consistent with a high-level suppression of signals from a low-level post-receptoral mechanism with tiled receptive fields, possibly in the retina or lateral geniculate nucleus.

2.2 Introduction

Fixational eye motions are tiny, microscopic eye movements which move a stimulus across dozens of photoreceptor cells and, consequently, across the receptive fields of many downstream neurons (Martinez-Conde et al., 2004). These are thought to be distinct from larger eye motions in that they are unintentional and occur even under steady fixation. It is now believed that fixational eye motions are a supportive feature of the visual system, for example, to enhance fine spatial vision (Poletti et al., 2013; Ratnam et al., 2017) or to refresh the neural signals to prevent fading of retinal images from perception (Martinez-Conde et al., 2006), a known consequence of adaptation to retinally stabilized stimuli.

In the visual periphery, where receptive field sampling of the photoreceptor mosaic is relatively coarse, fading is experienced even in the presence of fixational eye motion (e.g., Friedman et al., 1999; Sakaguchi, 2001; Sakaguchi, 2006). This was first reported by Ignaz Troxler in 1804, while other techniques have since been used to more precisely stabilize stimuli to the retina, e.g., by means of a mirror attached to a suction

cup (Yarbus, 1954; Yarbus, 1967) or contact lens (Ditchburn & Ginsborg, 1952; Riggs et al., 1953) and fixed to the anterior eye, or more recently using dual-Purkinje eye trackers (Kelly 1979; see also Poletti et al., 2013). In general, these techniques rely on the compensation of stimulus motion on the retina such that a stimulus remains stationary (or approximately so) even in the presence of fixational eye motion.

Fading of stabilized stimuli has been hypothesized to be the result of adaptation to luminance edges, either by the lower-level visual system (Clarke, 1961; Clarke & Belcher, 1962), or higher-level edge detectors (Ramachandran & Gregory, 1991), which become fatigued, thus causing the surround to be filled in to the missing region of perceptual space. However, fading occurs with more complex stimuli (Simons et al., 2006) and is facilitated by dynamic backgrounds (Anstis, 1989; Ramachandran & Gregory, 1991; Spillmann & Kurtenbach, 1992; Ramachandran et al., 1993), exhibiting different behavior with a variety of stimuli, which suggests that fading and the subsequent filling-in may occur at multiple distinct levels of the visual system, dependent on the stimulus characteristics (Welchman & Harris, 2001).

The present view is that signals representing the stimulus and surround spread about lateral connections within a cortical layer and through feedback connections between layers, a process normally interrupted by edge detection (Spillmann & Werner, 1996; Sakaguchi, 2001). Small eye motions which move an edge to a receptive field of a separate, unhabituated detector refreshes the neural representation of the edge and causes the stimulus to instantly reappear.

It has been proposed that another important factor governing fading is the balance in signals representing the stimulus and its surround which are normally separated by representation of an edge (De Weerd et al., 1995). When edges become adapted, the strongest signal dominates both regions of perceptual space. This was based on observations that fading occurs more rapidly against backgrounds larger in size, which is inconsistent with an edge adaptation explanation alone. Whatever the mechanism(s), it is generally agreed upon that fading is the result of habituation in neurons with receptive fields that sample from the area of the retina where a stimulus is stabilized.

In the present study, we were interested in whether we could measure the spatial extent of adaptation that results in perceptual fading of a stimulus. More specifically, we measured sensitivity to light stimulation in retinal locations within a few arcminutes of the adapting stimulus. Our hypothesis was that if the desensitization was the result of adaptation in post-receptoral neurons, then the spatial profile of sensitivity in the area surrounding the adapted location might reveal signatures of the spatial receptive fields of the adapted neurons.

The idea of a psychophysical analog to the receptive field was first termed a “perceptive field” by Jung & Spillmann (1970), but has typically been reserved in reference to population receptive fields (e.g., Neri & Levi, 2006) due to the impracticality of isolating individual neural receptive fields. However, recent advancements in retinal imaging and eye tracking have made it possible to simultaneously image, track and present stabilized stimuli to the retina (Roorda et al., 2002; Arathorn et al., 2007; Yang

et al., 2010; Sheehy et al., 2012; Harmening et al., 2014), providing the precise spatial control of stimuli required for this type of experiment.

To measure spatial areas of desensitization, we employed an adapting stimulus that was stabilized on the retina spatially but modulated in intensity over time. It has been previously reported that adaptation to flickered or pulsed stimuli results in perceptual fading (Schieting & Spillmann, 1987) and large reductions of visual sensitivity that cannot be explained by light adaptation at the receptor level (Frome et al., 1981).

We opted to use a pulsed stimulus in the current study for both practical and theoretical reasons. First, the scanning nature of the SLO system necessarily impedes presentation of time-invariant stimuli. A small-spot stimulus is only presented for a fraction of each frame, with a 30 Hz frame rate in our current setup.

Second, it is well known that the visual system is highly sensitive to temporal transient signals (e.g., Breitmeyer & Julesz, 1975). By making the adapting stimulus transient itself, we removed the ability of the visual system to detect the probe stimulus by novelty of a transient signal.

Third, reductions in sensitivity that occur following adaptation to repeated light stimulation in the periphery (Frome et al., 1981) are thought to be post-receptoral in origin, providing a psychophysical metric for the spatial extent of adaptation.

Two experiments are described in the following sections. In the first, we used a tracking SLO (or TSLO) to measure the spatial extent of desensitization to repeated light stimulation of the visual periphery (10 deg eccentricity) with small-spot stimuli that were stabilized to the retina. We found that the spatial areas of desensitization were not confined to the adapted area, but were small with sensitivity increasing sharply for probe stimuli only a few arcmin away from the adapted retinal location.

In the second experiment we used an adaptive optics SLO (or AOSLO), a system which corrects for monochromatic blur due to higher-order aberrations, to probe this effect on a finer spatial scale, at the level of individual cones. Here we report preliminary evidence for fading transfer between cone photoreceptors at 6 and 9 deg eccentricities, with larger areas of desensitization encompassing more cones at 9 deg than at 6 deg, consistent with known increases in receptive field size with eccentricity (Drasdo, 1977; Smith et al., 2001).

Additionally, we discuss the potential of this paradigm, or one similar, as a tool for *in vivo* receptive field mapping in the human.

2.3 Experiment 1: The Spatial Extent of Desensitization to Repeated Stimulation of the Retina with Small Flickered Spots

Two subjects (20106 and 20109) participated in the experiment. Both were naïve to the purposes of the experiment and had normal or corrected-to-normal refractive error. All procedures were approved by the University of California, Berkeley Committee for Protection of Human Subjects and adhered to the tenets of the Declaration of Helsinki. Informed consent documents were signed prior to participation.

2.3.1 Apparatus

The tracking scanning laser ophthalmoscope (TSLO) system used in this study was the same as described in a previous publication (Sheehy et al., 2012), with the addition of a light delivery arm used for visible light stimulation onto the retina (λ = 532 nm; CrystaLaser, Reno, NV). A superluminescent diode (λ = 840 nm; Superlum, Moscow, Russia) was used for retinal imaging and eye tracking. The visible and infrared (IR) light sources were fiber-coupled into acousto-optic modulators (AOMs; Brimrose) before entering the optical system. The light from the two input arms was combined at a dichroic beamsplitter before passing through a 4 mm entrance aperture. The field of view (FOV) was set to 3.2 deg, corresponding to a pixel sampling rate of 0.375 arcmins/pixel. A chinrest and temple pads were used to maintain the alignment of the subjects' pupils.

Stimulus delivery with the visible wavelength (λ = 532 nm) was achieved by switching on the light source with the AOM at the appropriate points in the raster scan. Stabilization of stimuli to the retina was achieved in the same way as described in previous publications (Sincich et al., 2009; Arathorn et al., 2007; Yang et al., 2010), and as described in the preceding chapter of this document. Briefly, image-based eye tracking was performed in real time by strip-based cross-correlation of each frame to a reference image as it is acquired. A prediction algorithm is then used to trigger delivery of the stimulus via the AOM at the strip preceding the targeted retinal location with a latency of ~2-3 milliseconds (Sheehy et al., 2012). Any motion of the eye during this time results in placement error, which can be quantified offline in a frame-by-frame analysis of retinal position relative to the digitally recorded stimulus position, described in further detail below.

TCA was corrected in the TSLO system by subjectively aligning the raster patterns formed by each input channel under foveal viewing conditions. This was necessary due to the lack of a light detection arm for imaging with the 532 nm light source in the TSLO. The magnitude of TCA at the tested eccentricity is therefore unknown and represents a fixed offset between the targeted retinal position and true stimulus location. However, when a stimulus is viewed through an external limiting aperture, as it is in the TSLO system, the magnitude of the lateral image offset between focused wavelengths on the retina depends on the location of the center of the aperture with respect to the center of the eye's pupil (Thibos et al., 1990). To combat this, we used real-time pupil tracking to keep the position of the pupil fixed with respect to the limiting aperture of the system. A pupil camera (CMOS color board; DFM 61BUC02-ML, Imaging Source Inc., Charlotte, NC) was aligned coaxially with the TSLO beam path via a beamsplitter placed before the eye. Pupil images were acquired at a rate of 10 Hz. Real-time auditory feedback from the pupil tracker was then used to alert the subject if the pupil became displaced by more than 0.3 mm, and the subject was instructed to briefly pause the experiment until they were realigned.

Longitudinal chromatic aberration (LCA) of the human eye was corrected by adjusting the vergence of the visible light source at its input to the system until the raster patterns formed by both channels were simultaneously perceived to be in best focus.

2.3.2 Stimulus & Procedure

The subjects' pupils were dilated and cyclopleged at least 30 minutes prior to the beginning of the experiment using one to two drops of 1% tropicamide and 2.5% phenylephrine ophthalmic solutions.

The experiment was performed at approximately 10 deg eccentricity along the superior retinal meridian. A green laser pointer was projected on the wall behind the TSLO system for fixation and appeared directly above the raster. Retinal eccentricity was determined for 20106 by montaging of images from the preferred retinal locus (as defined by Putnam et al., 2005) to the tested location. The fixation point was kept in the same location for subject 20109.

The stimulus was a small spot, Gaussian windowed (σ = 0.56 arcmin), with peak intensities reported below. This was done in order to blur the edges of the stimulus and minimize light spread beyond the center of the targeted stimulus location. Because the voltage response curve of the AOM is nonlinear, a lookup table was generated to linearize the light intensity output with an operational range of 1,000 intensity steps. Stimulus intensities are reported below in linear arbitrary units (a.u.) normalized to the maximum light output of the system; i.e., 1 a.u. corresponds to 3.85 log Trolands (log Td), including light from the imaging and stimulus sources. The background was composed of the raster pattern from the 840 nm imaging source, in addition to leak through the AOM fiber coupled to the visible stimulus wavelength (λ = 532 nm), which occurs even when zero voltage is applied (Domdei et al., 2018). The combined intensity of the background was 1.56 log Td, which is the floor (0 a.u.) on the normalized intensity scale. That is, all stimulus intensities are reported as an increment relative to the background.

The study comprised two parts which took place over five experimental sessions. In the first session, full psychometric functions were obtained from both subjects in order to determine the intensity corresponding to 95% probability of detection in the TSLO setup. Stimuli were unstabilized in order to measure thresholds under conditions of minimal adaptation. Stimuli were delivered over three frames (30 Hz frame rate), although, note that the stimulus is only presented for a fraction of the full frame duration in scanning systems (Sincich et al., 2009; Tuten et al., 2012).

Thresholds for 95% probability of detection were measured using a method of constant stimuli, with eight stimulus intensities, specified in a.u.: 0.15, 0.26, 0.39, 0.53, 0.68, 0.8, 0.91, 1. On each trial, subjects indicated whether or not the stimulus was visible with a key press. Between 120 to 130 trials were completed at each stimulus intensity, with intensities pseudo-randomly interleaved.

Second, we employed a novel paradigm to estimate the spatial extent of desensitization to repeated light stimulation. The stimulus was the same as described above, except that the intensity was fixed to the supra-threshold value determined to be detectable 95% of the time, and the stimulus was then targeted to a location determined by the experimenter in the 3.2 x 3.2 imaging field.

Each experimental session was comprised of an initial adapting period, where the stimulus was targeted to the same retinal location (which we refer to as the adapting

location), and was flickered in a 5 Hz envelope (three frames on, three frames off). The initial adapting period included 60 subject-paced repetitions of two-second trials. This was done to maintain image quality and eye tracking performance (allowing for blinks between trials) and alignment of the subject's pupil. By the end of the initial adapting trials, both subjects reported that the adapting stimulus had faded completely and was not visible.

Next, subjects completed two-second trials where the stimulus continued to appear at the adapting location for the first nine cycles, and, at the last cycle, the stimulus was targeted to the probe location. An auditory beep occurred simultaneously with the probe stimulus. For clarity, an example trial is illustrated in Figure 2.1. The probe stimulus was either (1) presented to the same location as the adapting stimulus, (2) presented to a location spatially offset from the adapting stimulus by 1.5, 3, 4.5 or 6 arcmin horizontally or vertically, or (3) did not appear at all (catch trials). Subjects were instructed to indicate whether the stimulus was present with a 0-to-3 confidence scale (0 = not seen; 1 = seen, low confidence; 2 = seen, medium confidence; 3 = seen, high confidence). No feedback was given.

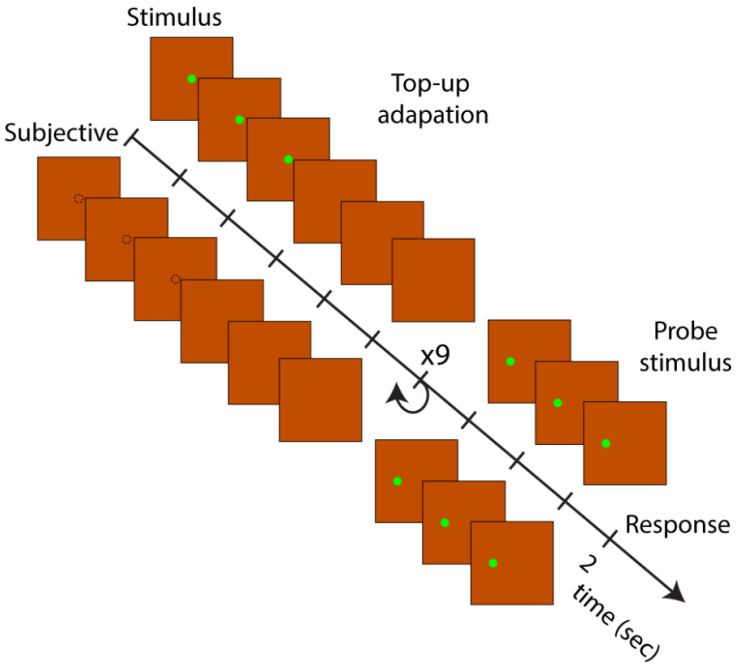

Figure 2.1. Time-course of a trial. The tick marks show intervals at the frame rate (each tick occurs at 1/30 seconds). This is a simplified schematic where frames are represented sequentially, but note that each frame is raster scanned such that an accurate depiction would place each pixel of the frame separately in the time domain. Trials each lasted two seconds, where the probe stimulus appeared in three-frame intervals (three on, three off). The first nine repetitions of the stimulus were for top-up adaptation, and the stimulus appeared at the adapting location as in the pre-adapting trials. The dashed circles denote the stimulus position in subject view and are meant to indicate that the stimulus was present but had faded. At the last onset, the probe stimulus was spatially offset horizontally or vertically. The subject indicated their response at the end of a trial. Note that stimuli are not drawn to scale here, the background was 3.2 deg and the stimulus was a small Gaussian windowed spot (σ = 0.56 arcmin).

Subjects each performed the task over four experimental sessions, where either horizontal or vertical offsets were presented during each session. Each session lasted approximately 2.5 hours with required breaks. The subject was allowed to request additional breaks if necessary, and in the event that the break lasted longer than a few seconds, 15 top-up adapting trials (identical to the initial adapting trials described in the previous paragraph) were performed to maintain the adapted state throughout the duration of the experiment.

Stimulus placement was recorded in the retinal videos by addition of a digital cross marker in each video frame at the location where the stimulus was delivered. Two adapting locations separated by approximately 0.5 deg were used in separate sessions for subject 20106. For subject 20109, adapting locations were targeted to the same retinal location in all experimental sessions. To return to the same retinal location whenever a new reference frame was needed for eye tracking, the reference frames were registered using the algorithm described by Guizar-Sicairos et al. (2008), and stimulus placement was updated accordingly.

Offline analysis was later performed to quantify stimulus location recovery (SLR, error in recovery of stimulus position after generation of a new reference frame) and placement accuracy (SPA, the error in stimulus delivery during the experiment), explained in further detail in the following sections.

2.3.3 Results

Full psychometric functions for both subjects are shown in Figure 2.2. Intensity is expressed in a.u. (see 2.3.2, Stimulus & Procedure), where 1 a.u. = 3.85 log Td, and 0 is the background (1.56 log Td). Data were fit with Weibull functions using the Palamedes toolbox in MATLAB (Prins & Kingdom, 2018). The intensity corresponding to 95% detectability was then interpolated from the fits, 0.80 a.u. for 20106 and 0.83 a.u. for 20109. A bootstrap resampling procedure (10,000 resamples) was used to estimate 95% confidence intervals for these values, which were 0.69 a.u.(lower bound) to 0.85 a.u. (upper bound) for 20106 and 0.72 a.u. (lower bound) to 0.91 a.u.(upper bound) for 20109.

Stimulus placement accuracy (SPA) for each experimental session was assessed using the following procedure: The stimulus position in each video frame (denoted by the digital cross marker) was determined by cross-correlation, and each video frame was then cropped so that the cross was centered in a 1.25 x 1.25 deg field. Each cropped frame was then cross-correlated to a single reference frame (typically the first acquired frame of the session) in order to quantify the motion of the retina relative to the stimulus. The result was a distribution of stimulus positions relative to the reference. The center of each distribution was then shifted to the median stimulus position to remove the effect of the initial reference selection. The distribution of stimulus placements was then used for modeling light delivery on the retina described in the following section.

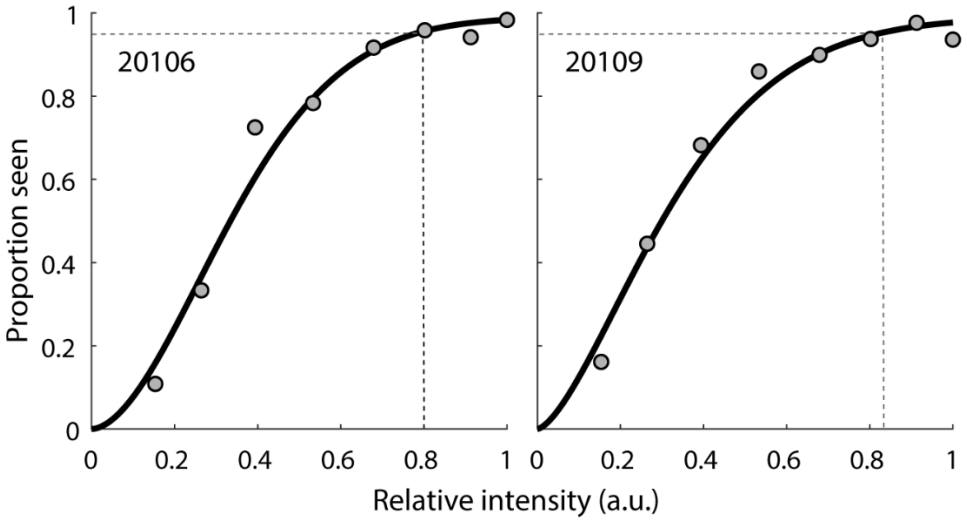

Figure 2.2. Psychometric functions (proportion seen as a function of intensity). Intensities are reported on an arbitrary unit scale, where 0 is the background (1.56 log Td) and 1 is the maximum intensity output of the system (3.85 log Td). Dashed lines show 95% frequency of seeing, 0.8 a.u. for subject 20106 (left) and 0.83 a.u. for subject 20109 (right). Solid lines are Weibull fits.

To register stimulus placement across experimental runs, a high SNR image consisting of 60 averaged frames was used as a master image. Another high SNR reference image was generated for each experimental run by averaging the frames of the first trial's video. Each reference image was then registered to the master image with a discrete fast Fourier transform (FFT) algorithm, as described in Guizar-Sicairos et al., 2008. The optimal angle of rotation was found by iteratively rotating the images and registering to the master reference. The optimal rotation was taken at the angle which produced the smallest normalized root-mean-square (RMS) error between the registered image and the master. Finally, the Δx and Δy translational offsets between images were applied to the digital cross locations in the reference to determine the master image coordinates.

For analysis of behavioral data, the locations of probe stimuli were recovered using the same procedure described above, and the data were binned with centers defined by the targeted probe offsets. D-prime (d') was then calculated for each probe location using the procedure described by Wickens (2002). D' is a sensitivity index corresponding to the separation of the signal and noise distributions estimated from performance in target and catch trials, respectively. A log-linear correction was applied to correct for extreme hit and false-alarm rates (Hautus, 1995).

Results are shown for each subject in Figure 2.3, where markers are overlaid on the master reference image to show probe locations relative to the adapting location, and colored corresponding to d' for each stimulus location. In general, sensitivity to the probe stimulus was diminished near the adapting point, but increased quickly as the probe was spatially offset.

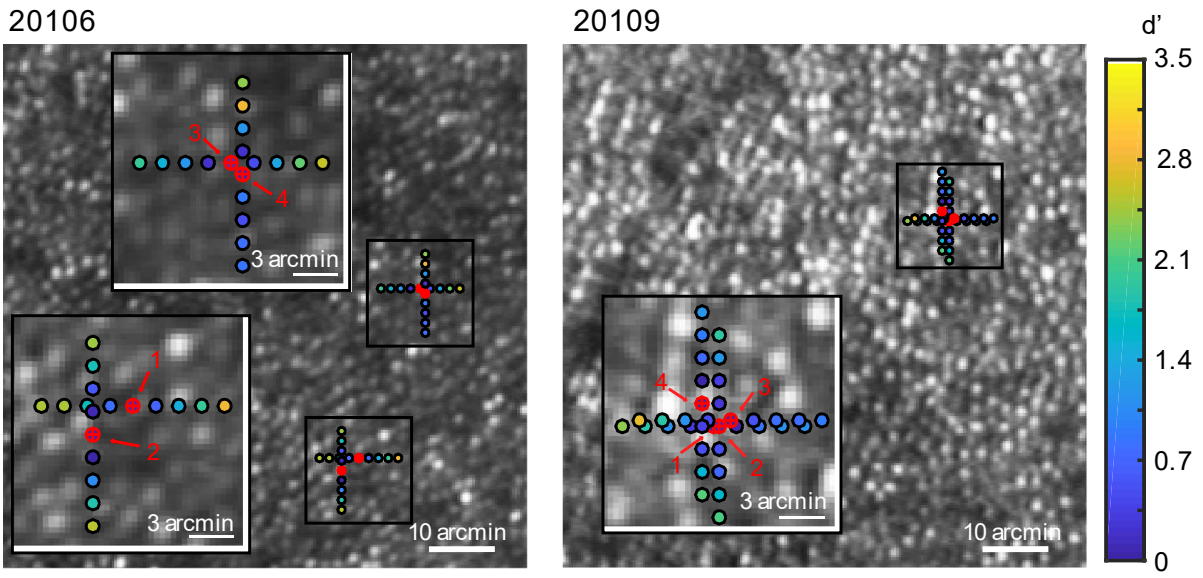

Figure 2.3. Sensitivity (d') of probe stimuli. The red crossed markers indicate the location of the adapting stimuli. Each marker represents a probe stimulus offset relative to the adapting stimulus, with colors corresponding to the sensitivity index d', as indicated by the color bar on the right.

2.3.4 Modeling

We next considered whether light adaptation at the receptor level could predict the spatial extent of desensitization. To address this, we modeled the light delivery distribution of the adapting stimulus on the retina by convolution of the estimated intensity distributions of each source of uncertainty (uncorrected optical blur, error due to changes in TCA with pupil displacements, and SPA).

We first considered blur due to uncorrected monochromatic aberrations. Since the true point spread function (PSF) is unknown, we modeled optical blur as a Gaussian with σ = 1 arcmin (corresponding to about twice the full width at half maximum (FWHM) of the diffraction limited Airy pattern over a 4 mm pupil, λ = 532).

Next, we considered additional error that is introduced by dynamic changes in transverse chromatic aberration (TCA) that occur with pupil displacements when stimuli are viewed through an external limiting aperture. We measured pupil displacements directly with real-time pupil tracking (Privitera et al., 2016) during the experiment, and then inferred the chromatic offsets due to changes in TCA at each pupil position using the slope (3.86 arcmin/mm) of published data relating the linear change in TCA as a function of pupil displacement (Boehm et al., 2019, see Chapter 4). From this we generated a matrix representation of TCA across the two spatial dimensions. The standard deviation of TCA offsets due to pupil displacements was, on average, 0.35 arcmin; although there were slight asymmetries between horizontal and vertical TCA offsets for 20106.

We then used the distribution from SPA analysis described in the preceding section to estimate the effects of stimulus placement error on the overall light delivery

profile on the retina. The center of each distribution was shifted to coincide with the recovered position in the master image. Note that this incorporates the additional errors in stimulus position that are introduced by SLR during the experiment, which were determined previously by registering each reference with the master image taking into account rotational distortions.

Finally, we estimated the light intensity distribution of the adapting stimulus on the retina as a convolution of the potential sources of uncertainty in stimulus position with the stimulus itself.

$$L = Stimulus(1, \sigma = 0.56') \otimes Optical(1, \sigma = 1') \otimes TCA \otimes SPA \qquad \text{(Equation 2.1)}$$

An example of the resulting model is shown in Figure 2.4. Note that a separate model was used to estimate the light distribution in each experimental session. For comparison with Figures 2.3 and 2.5, this example corresponds to subject 20109, location 2.

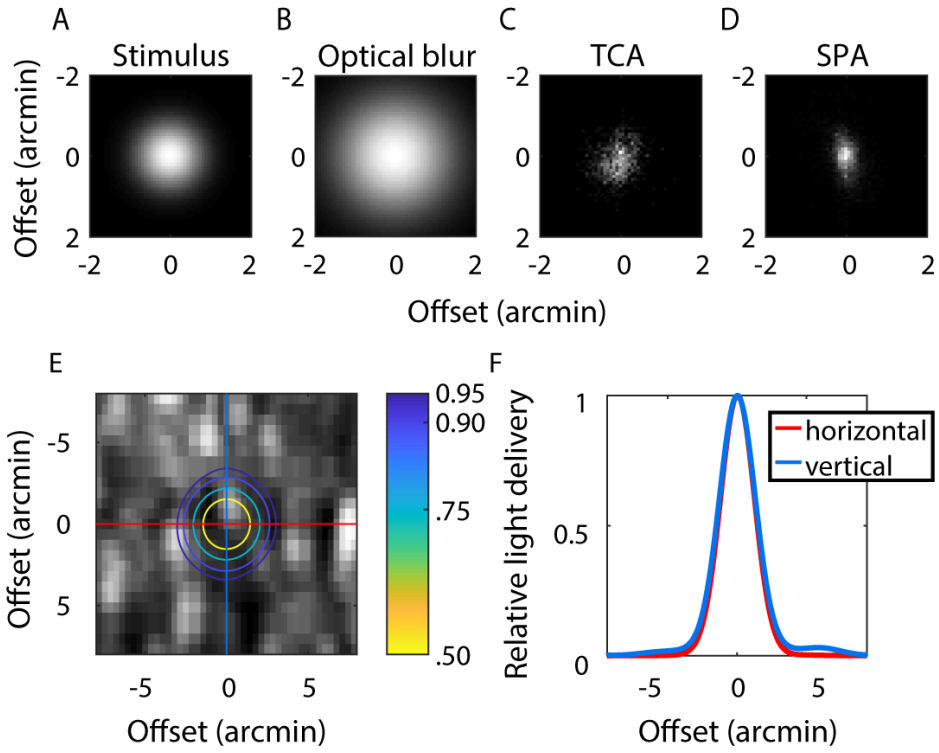

Figure 2.4. Light delivery model. The light distribution on the retina was considered for the stimulus (A), optical blur (B), TCA offsets due to pupil displacements (C), and SPA (D), with the output of the convolution shown overlaid on the retinal image (E). The colored contours represent the relative light delivery, as specified by the color bar. For comparison with the data, horizontal or vertical profiles were used (F), consistent with the direction of probe offsets.

To model sensitivity (d') versus probe offset, we assume that sensitivity is inversely proportional to the fraction of total light at any given retinal location, approximated by the following equation:

$$d'_p = (-L + \max(L)) \times d'_n \qquad \text{(Equation 2.2)}$$

Where d'_p is d' at a given probe offset, p, and d'_n is the observer's sensitivity without adaptation. The model of predicted sensitivity for probe offsets (d'_p) assumes that desensitization should be directly proportional to the amount of light in the adapting stimulus, consistent with adaptation mediated by cone photoreceptors.

Figure 2.5 shows the experimental data in addition to the model output from Equation 2. In the plots, either the horizontal or vertical cross section is shown, consistent with the orientation of probe offsets in the corresponding experimental condition and reflecting any directional (horizontal versus vertical) asymmetries in TCA or SPA.

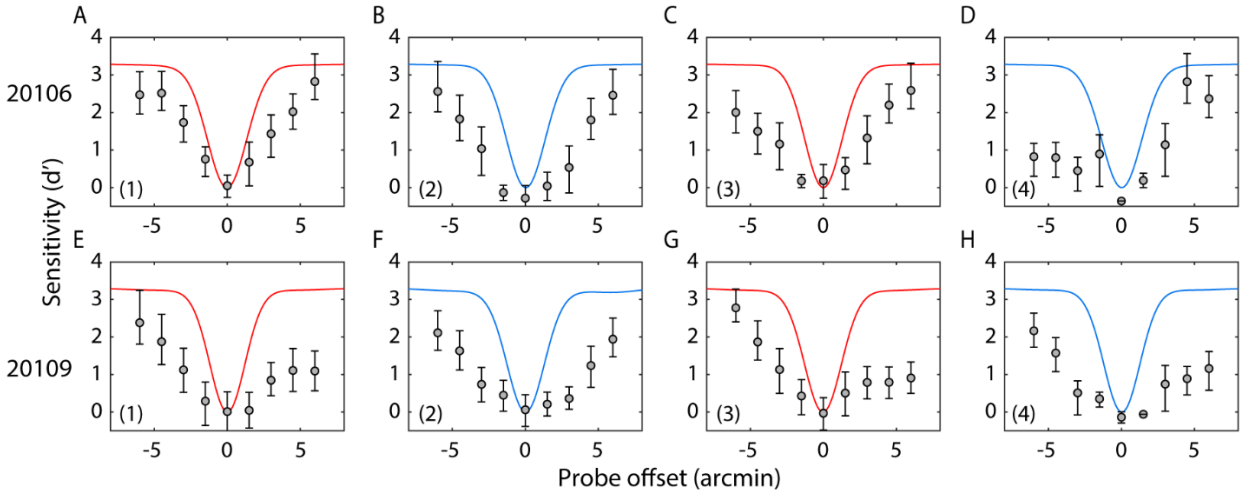

Figure 2.5. Sensitivity (d') as a function of probe offset relative to the adapting location. Error bars are 95% bootstrapped confidence intervals (10,000 resamples). Panels A-D show data for subject 20106 at the labeled adapting locations in Figure 2.3 (1-4), and similarly for 20109 (panels E-H). Model estimates (Eq. 2.2) for horizontal (red) and vertical (blue) probe offsets are shown by the solid lines. For the model, d'_n was assumed to be 3.29, corresponding to hit rate = 0.95 and false alarm rate = 0.05.

In general, the model underestimates the spatial extent of the observed desensitization, consistent with the interpretation that threshold elevation is not simply due to light adaptation in the photoreceptors. This leaves open the intriguing idea that the spatial areas of desensitization are psychophysical signatures of the receptive fields of the post-receptoral adapted neurons, a point we consider in more detail below.

2.3.5 Discussion

To investigate the spatial specificity of desensitization to repeated light stimulation on the retina, we measured sensitivity for probe stimuli which were spatially offset from an adapting stimulus in a TSLO. We found that sensitivity increased rapidly as a function of

distance from the adapting stimulus, with probe stimuli only a few arcminutes away retaining sensitivity.

We then considered how the light distribution of the adapting stimulus on the retina might affect sensitivity in nearby locations. To gauge whether light adaptation in the receptors could account for the observed threshold elevation, we modeled the total light distribution on the retina, and found that the areas of reduced sensitivity extended beyond the area of the retina that was exposed to light from the adapting stimulus. While the model is oversimplified in its presupposition that sensitivity is inversely proportional to the fraction of light delivered (it assumes no saturating effects of the adaptation), this is a reasonable assumption for cone-mediated light adaptation at the light levels used for the adapting stimulus (3.76 log Td), with the half-bleaching constant for cones reported to be 4.3 log Td (Rushton 1965; Rushton & Henry, 1968). Therefore, the model suggests that the desensitization observed after repeated stimulation to stabilized, flickered stimuli in the SLO is not simply due to light adaptation, consistent with previous work with more conventional stimuli (Frome et al., 1981).

This leaves open the possibility that the area of desensitization is mediated by downstream receptive field sampling of the photoreceptor mosaic. If adaptation to the stimulus (and the corresponding reduction in sensitivity) occurs in a post-receptoral neural unit with a receptive field covering more retinal space than is stimulated directly, a potential consequence is that the reduction in sensitivity extends to nearby retinal locations which were not directly exposed to the stimulus, like we observed in our data. This would imply that the desensitized areas are psychophysical signatures of the receptive field sampling of the adapted neurons. This concept has been previously referred to as a perceptive field (Jung & Spillmann, 1970; see also Spillmann et al., 1987, and Neri & Levi, 2006) to designate its status as the psychophysical analog to the receptive field.

What neural units might impose the spatial limits to the desensitized areas we observed? Our data suggest that the effect is remarkably spatially specific, with probe stimuli only a few arcminutes away retaining sensitivity. This may implicate midget retinal ganglion receptive fields and the corresponding parvocellular pathway, which is known to have the smallest receptive fields of the primate visual system (De Monasterio & Gouras, 1975; Dacey, 1993). Histological tracings of the connections between cones, bipolars, and ganglion cells suggests that the receptive fields of midget retinal ganglion cells sample from only a handful of cones at 10 deg eccentricity, with approximately 6 arcmin of coverage (Dacey & Peterson, 1992). Comparatively, the receptive fields of parasol cells (and the magnocellular neurons they project to) are orders of magnitude larger. Thus, the size of the desensitized areas we measured are most consistent with the smaller midget/parvo receptive fields.

It is worth stating explicitly that the consistency in size of the desensitized areas with midget retinal ganglion cells and parvocellular neurons does not presume that desensitization occurs at the same neural site where the spatial limits of the effect are imposed. For example, it might be the case that habituation occurs further upstream but is delimited spatially at the site of convergence.

For example, neurons in the superior colliculus habituate strongly to repeated stimulation, with strong transient responses to novel stimuli (Goldberg & Wurtz, 1972; Woods & Frost, 1977; Boehnke et al., 2011). The transient responses of visual SC neurons are thought to be important for orienting an observer to novel stimuli through convergence of bottom-up and top-down processes which determine stimulus salience (Boehnke & Munoz, 2008), and is now understood to have inputs from both the magnocellular (Schiller et al., 1979) and parvocellular (White et al., 2009) geniculate pathways.

Additionally, it is worth noting that the coincidence of the spatial extent of desensitization with the size of the smallest visual receptive fields does not preclude the possibility that desensitization occurs across multiple pathways. Since the adapting stimulus becomes completely invisible following adaptation, it is a reasonable assumption that whatever pathways would otherwise support detection of the stimulus are no longer sufficient to retain visibility. In this case, the logic follows that the neural unit with the most proximal unadapted receptive field would support detection of probe stimuli nearest to the adapter, favoring the pathway with the smallest receptive fields. Additionally, if detection is supported by separate mechanisms pre- and post-adaptation, this could explain why sensitivity did not reach that estimated by the model even at the largest probe offsets.

In general, our data are in support of a low-level origin for the spatial effects of desensitization. Retinal ganglion cell receptive fields of a given type tile the retina, with minimal overlap between adjacent receptive fields (Dacey, 1993; Field et al., 2010). At higher-level visual areas, receptive fields become more complex in structure (Hubel & Wiesel, 1962), sampling from larger, overlapping retinal areas (Smith et al., 2001). The rapid increase in sensitivity we observe is most consistent with a tiled mosaic, and thus a low-level origin for the spatial effects of desensitization. This may be reflected in the asymmetries we observe in the varying directions of spatial offset relative to the adapting point. Random selection of a point in a tiled mosaic would result in an asymmetric pattern of desensitization on the retina. However, we cannot rule out with the current experiment that these asymmetries may be due to other factors; for example, changes in sensitivity due to vasculature, variations in pigment spectral sensitivity, or an asymmetric PSF.

A welcome follow-up to this study would be to perform a similar experiment with even finer spatial control of the stimulus, i.e., with adaptive optics, in order to reveal any tiling or coinciding borders between desensitized areas. We describe preliminary data for such an experiment in the following sections.

2.4 Experiment 2: Transfer of Desensitization Between Individual Cones

One subject (20076) participated in the experiment. All procedures were approved by the University of California, Berkeley Committee for Protection of Human Subjects and adhered to the tenets of the Declaration of Helsinki. Informed consent documents were signed prior to participation.

2.4.1 Apparatus

The AOSLO used in Experiment 2 is the same as described previously (Roorda et al., 2002; Harmening et al., 2014), with details pertinent to the current experiment specified below.

The system was equipped with a Shack-Hartmann wavefront sensor which measures the distortions in the wavefront due to optical aberrations of the eye. A deformable mirror (DM; DM97, ALPAO, Montbonnot-Saint-Martin, France) was used to correct for the measured distortions in real time in a closed-loop system. Four wavelengths were selected from a supercontinuum light source (SuperK EXTREME, NKT Photonics, Birkerod, Denmark), 543 nm, 680 nm, 840 nm and 940 nm. The 940 nm wavelength was used for wavefront sensing, 840 nm for retinal imaging, and 543 nm for cone-targeted stimulation. 680 nm was not used in the current experiment. Each light source (excluding 940 nm) was fiber-coupled to an acousto-optic modulator (AOM; Brimrose Corp., Sparks Glencoe, MD), which was used to switch on and off the independent light sources at the appropriate points in the raster scan.

A projector (LightCrafter, Texas Instruments, Dallas, Texas) was coaligned with the AOSLO beam path in a Maxwellian setup to provide a fixation target and uniform background during the experiment. A pupil camera (CMOS color board, DFM 61BUC02-ML, Imaging Source Inc., Charlotte, NC) was placed at the back end of the Maxwellian assembly, conjugate to the pupil.

LCA was corrected by adjusting the relative source vergences (Grieve et al., 2006; Harmening et al., 2012), following published LCA models (Atchison & Smith, 2005).

2.4.2 Stimulus & Procedure

The subject (20076) sat in the system with a bite bar stationed on a mount to minimize head movements. Two drops of 1% tropicamide and 2.5% phenylephrine ophthalmic solutions were administered at least 30 minutes prior to the beginning of the experiment for pupil dilation and cycloplegia.

Residual uncorrected LCA was measured by assessment of the images taken with the 840 nm and 543 nm wavelengths at different levels of defocus induced with the DM. The optimal defocus of 543 nm was used during the experiment to ensure the sharpest PSF for the stimulus wavelength. The difference in defocus levels for best 543 and 840 nm image quality was typically less than 0.02 diopters; thus, 840 nm image quality was compromised by only a small amount.

TCA was measured following the methods detailed in Harmening et al., 2012. Briefly, three five-second videos were taken, where each frame consisted of interleaved lines of the different channels (543 nm, 680 nm and 840 nm). A cross-correlation procedure was used to calculate the offset between images obtained with the relevant wavelengths (840 and 543 nm for retinal imaging and stimulation, respectively). The tolerance was set to 0.15 mm for pupil tracking, corresponding to 0.58 arcmin (< 1 cone diameter at the eccentricities tested) of chromatic offset between 543 (stimulus) and

840 nm (imaging) wavelengths due to pupil displacements (Privitera et al., 2016; Boehm et al., 2019). Due to the high intensities of light needed to image in the visible range, at least ten minutes' time was taken between TCA measurements and the beginning of the experiment to allow for replenishment of photopigments.

The experimental paradigm was similar to that of Experiment 1, with key differences specified here. The experiment was performed at 6 and 9 deg eccentricities (relative to the preferred retinal locus or PRL, Putnam et al., 2005), determined by montaging of images from the fovea to the experiment locations. The fixation target was a small spot presented through a projector aligned in Maxwellian view to the AOSLO beam path (see 2.4.1 Apparatus). Additionally, the projector was used to form a dim white background (roughly 8 cd/m^2) which appeared in the same location as the raster. This was done to minimize any contribution from rod photoreceptors. (Note that in the previous experiment this was achieved by the high background intensity caused by leak through the 532 nm channel of the TSLO. Here the intensity due to leak is much less as a higher ND filter is placed at the source.)

The stimulus was a small square, with size scaled to roughly equate single-cone sensitivity across eccentricities. The stimulus was 0.77 arcmin in diameter when the experiment was performed at 6 deg eccentricity and 1.22 arcmin at 9 deg. In both cases, this is < 1 cone diameter. The stimulus intensity was fixed at 0.7 a.u. on a linearized intensity scale, where 0 is the background and 1 is the maximum output of the system setup, corresponding to a retinal illuminance of 5.59 log Td.

At the beginning of the experiment, the experimenter selected seven cones from a high SNR image obtained by frame averaging of a two-second stabilized video of the retina (Figure 2.6A). We attempted to select seven contiguous cones at each experimental session. The first cone selected was designated as the adapter cone, with the remaining six cones at variable distance from the adapter cone (typically one or two cone spacings away).

Each trial (pre-adapt and probe) lasted one second. First, 60 to 80 pre-adapt trials were performed. The subject responding with the number of flashes seen (0 to 5) using a keypress on each pre-adapting trial to roughly characterize the time-course of desensitization. The reason for the different durations of pre-adaptations was that we observed asymptotic behavior at the end of the 60-trial duration, and later added an additional 20 trials to verify that this behavior continued at longer durations. All data collected at 9 deg was with the 80-trial duration, and approximately half of the data collected at 6 deg was with the 60-trial duration. During pre-adapt trials, the stimulus was delivered in three frame pulses (three on, three off) to the adapter cone, with five repetitions per trial.

Next, the subject completed 80 probe trials, where the stimulus was presented to the adapter cone in four, three-frame pulses (three on, three off) to maintain adaptation throughout the course of the experiment. At the fifth pulse, the stimulus was delivered to one of the seven selected cones, with trials pseudo-randomly interleaved. An auditory beep accompanied the probe stimulus to indicate timing to the subject. Figure 2.6B shows the time-course of the probe trials. Note that the stimulus is only on for a fraction

of each frame duration, as the raster is scanned over the targeted cone location. The subject indicated their confidence that the probe stimulus was seen on a 0-3 scale, 0 being not seen, and 3 being confidently seen. No feedback was given.

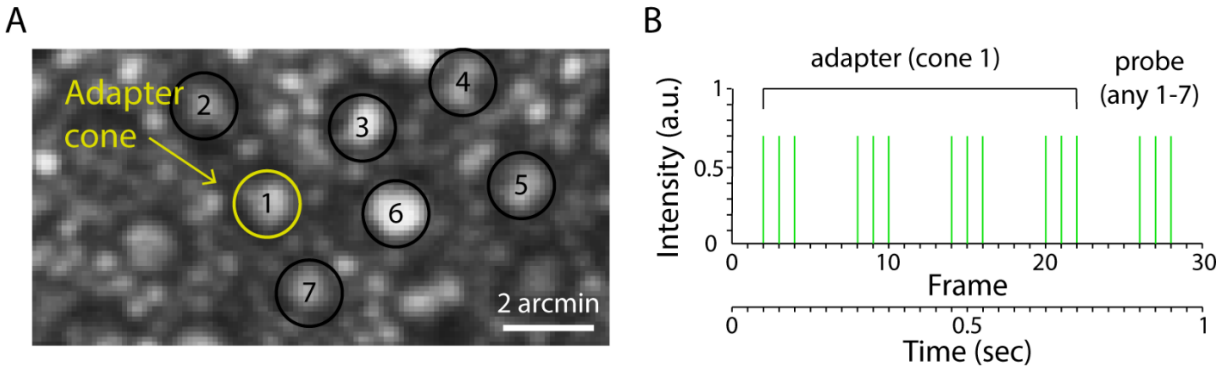

Figure 2.6. Cone selection and stimulus time-course. Seven cones were selected from a frame-averaged image (A). The first cone selected was the adapter cone. (B) shows the time-course of the stimulus for a single probe trial. 543 nm (green) light was delivered to the adapter cone for four repetitions of three frames on, three frames off. At the last three-frame presentation, the probe stimulus was delivered to any of cones 1-7 (including the adapter). Note that the time-course is specified in frames to highlight the fact that the stimulus was only on for a fraction of each frame duration (as the raster scanned over the targeted cone). The entire trial (30 frames) lasted one second. Intensity is specified in a.u.

2.4.3 Results

Prior to analysis of the data, tracking error was quantified by identifying the location of the targeted cross in each stimulus frame. Trials were excluded from analysis when the probe stimulus was not delivered within a specified distance of the targeted location, 1 arcmin at 6 deg and 1.34 arcmin at 9 deg, corresponding to roughly one-half cone spacing, which we determined by evaluating the distance between adapting cones and the probe cones that were nearest neighbors (i.e., the six neighboring cones surrounding the adapter in the hexagonal packing arrangement). Additionally, if the overall tracking error (mean distance of delivered location relative to the targeted position) exceeded this threshold, the entire session was excluded.

We recovered cone locations relative to a master image by cross-correlating cropped sections of the frame used for cone selection (see previous section, 2.4.2 Stimulus & Procedure) with a manually identified section of the master image. The resulting output gave reasonable alignment between the selected cones in the images, and cone centers were manually selected to correct for any errors due to rotational (torsion) offsets between frames or distortions due to reference frame artifacts.

We next looked at the subjects' responses to pre-adapting trials. Figure 2.7 shows the mean number of flashes reported as seen by the subject as a function of trial number. Note that only 60 trials are shown here, but in some cases 80 pre-adapting trials were used (see 2.4.2 Stimulus & Procedure). The data for 6 deg is shown in the left panel and 9 deg in the right panel. In general, the time-courses are similar between the two eccentricities; however, sensitivity appears to drop off more quickly at the

greater eccentricity. Fading typically occurs more rapidly as a function of eccentricity, but because we only roughly equated sensitivity across the two conditions, we cannot rule out that this is due to an overall reduction in sensitivity to the stimulus at 9 deg than at 6 deg. We discuss this possibility further below.

At 6 deg, one adapting cone was identified as a putative S-cone. S-cones have very low sensitivity at the stimulus wavelength (543 nm). For this cone, the subject responded 0 or 1 on every pre-adapting trial. Additionally, in another session where the same cone was selected but not as the adapter, the subject had very low sensitivity to the probe stimulus when it was targeted.

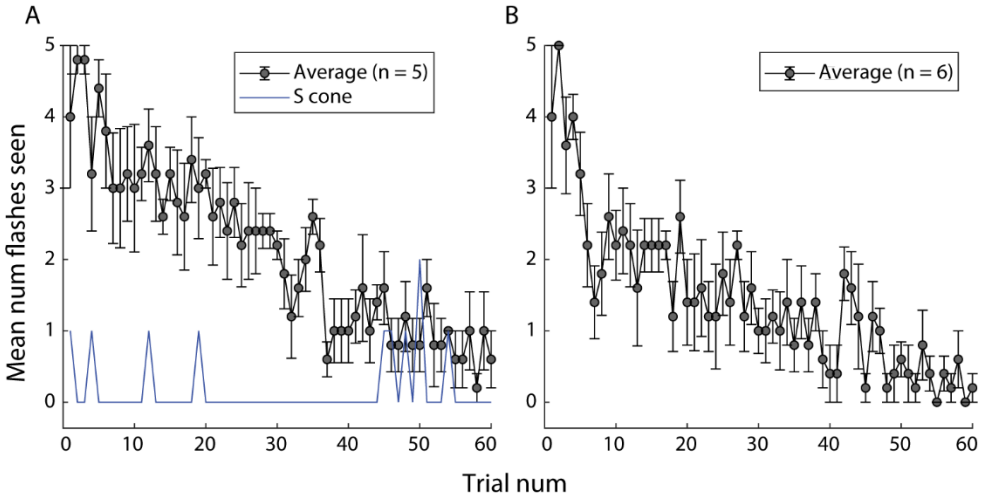

Figure 2.7. Rough time-course of adaptation to repeated stimulation of single cones. Data from 6 deg eccentricity is shown in the left panel and 9 deg in the right panel. The gray markers (and solid black line adjoining them) show the mean number of flashes seen on each trial (n = 5 sessions at 6 deg, and n = 6 at 9 deg). Note that in some cases 80 pre-adapting trials were completed. That data is omitted here, but it followed the same general pattern (i.e., less than one flash was seen on average). At 6 deg (left panel), one of the adapter cones was identified as a putative S-cone, shown here as the solid blue line.

For analysis of probe trials, data from different sessions that included the same adapter/probe pairs were combined, but typically only one session of data was collected for each pair. Overall, 42 adapter/cone pairs were tested at 6 deg, and 39 at 9 deg. This sample included 26 and 16 unique cones at 6 and 9 deg, respectively. Figure 2.8 shows sensitivity (d') as a function of distance from the adapter cone. To evaluate whether cones closer to the adapting stimulus, i.e., neighboring cones, had lower sensitivity than cones farther away, values of d' were separated into three groups based on their proximity to the adapter cone.

The first group consisted of adapter cones only. The second group was composed of the nearest neighbors to the adapter cone (the ring of six surrounding cones in a hexagonal packing arrangement), which we call "proximal cones." The third group was termed "distal cones," which included those farther away than the surrounding ring (typically by one cone-spacing, though a few were two to three spacings away). Cones were binned into groups based on their distance from the

adapter cone in the retinal image, with the cutoff between proximal and distal groups set to 2.7 arcminutes for data collected at 6 deg and 3.5 arcminutes for data collected at 9 deg. The average proximal and distal cone distances were 2.01 and 3.94 arcmins at 6 deg, and 2.69 and 5.71 arcmins at 9 deg. The average sensitivity index (mean d') for cones at 6 deg was -0.0028 for adapter cones, 1.098 for proximal cones, and 1.914 for distal cones. At 9 deg, this was -0.0692 for adapter cones, 0.6248 for proximal cones, and 1.4411 for distal cones.

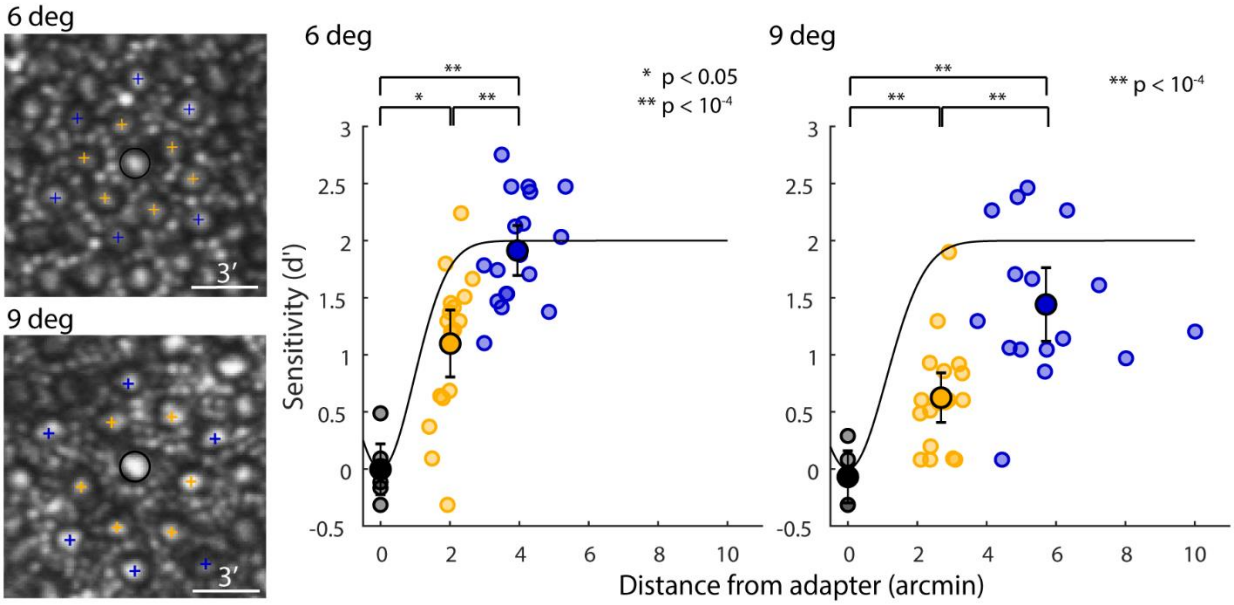

Figure 2.8. Sensitivity (d') as a function of distance from the adapter cone. The left panels show retinal images at 6 deg (top) and 9 deg (bottom). On the right, sensitivity (d') is shown for individual cones, in addition to group averages. In the images on the left, the larger cells are cone photoreceptors showing the hexagonal packing arrangement, and the smaller cells are rod photoreceptors which surround the cones. Cones were grouped according to whether they were nearest neighbor cones (proximal cones, yellow crosses) or cones one or more spacings away (distal cones, blue crosses) from the adapter cone (black circle). Note that this is just an example to visualize the different groupings. The cones shown here do not correspond in a meaningful way to the data shown. In the data in the right panels, data is shown for adapter cones in black, proximal cones in yellow, and distal cones in blue. Error bars on mean estimates (larger markers) are 95% confidence intervals. Statistical comparisons are shown for the group averages. Solid black lines show sensitivity predictions based on the light delivery model (Eqs. 2.1-2).

We performed a one-way analysis of variance (ANOVA), and found a main effect of group (adapter, proximal, distal) at both 6 deg [$F(2,39) = 31.28$, $p = 7.84 \times 10^{-9}$] and 9 deg [$F(2,36) = 18.38$, $p = 3.16 \times 10^{-6}$] eccentricities. A Tukey-Kramer test was then used to evaluate differences between individual groups. All groups were significantly different from one another, with $p < 10^{-4}$ or lower in all cases, except between adapter and proximal (neighboring) cones at 6 deg eccentricity, which was significant at the $\alpha = 0.05$ level. (Note that we did not consider correction for multiple comparisons in reporting these values.)

To consider how light delivery may have influenced our results, we constructed a model similar to that described for the previous experiment (see 2.3.4 Modeling). Separate models were generated for each eccentricity to reflect the different tolerances allowed for stabilization and tracking errors.

To account for blur from uncorrected monochromatic aberrations, we modeled the diffraction limited PSF over a 6.5 mm pupil for λ = 543, with the addition of 0.059 D residual defocus after AO correction (Harmening et al., 2014). To estimate the effect of transverse chromatic offsets due to changes in TCA with pupil shifts we generated a Gaussian function with σ = 0.29 arcmin, corresponding to the estimated chromatic offset at one half the tolerance setting of 0.15 mm for pupil tracking that was used during the experiment (3.86 arcmin/mm; Boehm et al., 2019). To account for errors in stimulus delivery a second Gaussian function was generated with σ = 0.88 arcmin for comparison of the model with 6 deg data and σ = 0.99 arcmin for 9 deg, reflecting the average standard deviation of the recovered stimulus positions across all experimental sessions. Finally, the estimated light delivery distribution, *L*, was generated by convolving the stimulus with each of the above described sources of blur and uncertainty in stimulus position (Equation 2.1).

To model sensitivity as a function of probe offset, we applied the estimated light delivery distribution, *L*, to Equation 2.2, with $d'_n = 2$ (a rough estimate of single cone sensitivity with no adaptation). The resulting functions are plotted with the data in Figure 2.8. For the 6 deg data, the model generally overestimates sensitivity for proximal cones and is close to the average sensitivity for distal cones. In contrast, the model generally overestimates sensitivity at all probe offsets, suggesting, similar to our findings in Experiment 1, that our results cannot be accounted for by light adaptation at the photoreceptor level.

2.4.4 Discussion

In Experiment 2, we delivered repeated pulses of light to individual cones at 6 and 9 deg eccentricities and measured the spatial effects of desensitization to repeated stimulation by assessing sensitivity in nearby cone photoreceptors. To summarize our findings, at both eccentricities, cones neighboring the adapter (proximal cones) had lower sensitivity than cones two or more spacings away (distal cones). Qualitatively, more cones were desensitized at 9 deg than at 6 deg, with many of the proximal cones at 9 deg having d' < 1.

It is unlikely that blur due to uncorrected aberrations or errors in stimulus placement due to TCA or tracking failures can account for our findings. These sources of error should similarly affect all cones of approximately the same distance from the adapter, while our preliminary data suggests that the effect is cone specific, with cones of nearly equal distance from the adapter showing variable sensitivity. While it is true that sensitivity varies between nearby cones even without adaptation (a point we return to below), the range of d' values for proximal cones at 6 deg is larger than at 9 deg, suggesting that normal variability in single cone sensitivity cannot account for our findings.

We selected 6 deg as one of the tested eccentricities because it is here that histological tracings of human retinal tissue first show deviance from the 1:1 wiring scheme typical of cones and midget retinal ganglion cells in the fovea and parafovea (Dacey & Peterson, 1992; Dacey, 1993). In Figure 2.8, sensitivity for individual cones is shown by the smaller markers, but note that these values are based on very few (typically ten) trials, precluding more sophisticated analyses on a cone-by-cone basis. Nonetheless, it is tempting to point out qualitatively that at 6 deg, proximal cones appear to segregate into two groups. Some cones neighboring the adapter (proximal cones) have sensitivity similar to the adapter cones, while others have sensitivity comparable to the more distal cones.

At 9 deg, there is generally lower sensitivity for both proximal and distal cones than at 6 deg, with most proximal cones at 9 deg having d' < 1, consistent with increasing convergence of cones to downstream neurons. However, as stated previously, we only roughly equated single-cone sensitivity (without adaptation) across eccentricities. It is encouraging that the cones with the highest sensitivity at both eccentricities are comparable, but the possibility that our results are influenced by an overall lower sensitivity to the adapting stimulus at 9 deg cannot be ruled out. Future experiments should fully characterize single-cone sensitivities at the eccentricities tested.

Additionally, it is still unknown to what extent single-cone increment thresholds vary in the periphery. It has been shown that at the fovea, thresholds are highly variable between cones (Harmening et al., 2014; Bruce et al., 2015). There are several potential reasons for this (discussed in Harmening et al., 2014), for example, variability in physiological weighting of cone inputs to downstream neurons (Sincich et al., 2009; Field et al., 2010; Li et al., 2014), which may play a larger role in the peripheral retina where convergence of cones to downstream neurons increases.

It is possible that some of the cones tested were S-cones, which are insensitive to the stimulus wavelength (543 nm). However, S-cones make up only 5% of the cones in the retina. In our sample of 26 and 16 unique cones at 6 and 9 deg eccentricities, respectively, we expect very few to be S-cones (one to three). We attempted to identify any putative S-cones in our data by looking for cones which were consistently insensitive across sessions, and identified only one at 6 deg eccentricity (see Results 2.4.3). The putative S-cone was selected randomly as an adapter cone, with the subject's response to pre-adapting trials shown in Figure 2.7A (blue line). The subject responded with 0 or 1 on every trial that this cone was targeted.

2.5 Conclusions & Future Directions

To summarize, the results presented in Experiment 1 demonstrate that the reduced sensitivity observed after repeated exposure to small spots of pulsed light in the periphery extends to nearby areas of the retina which were not directly exposed to the adapting stimulus. This is consistent with a post-receptoral origin for the effect, and inconsistent with simple light adaptation at the receptor level. The localization of the

effect to areas of the retina within only a few arcminutes of the adapting stimulus suggests that the spatial sampling resolution of such a mechanism must be high, like that afforded by the small receptive fields of the parvocellular neurons which draw their inputs from the smallest receptive fields at the output of the retina, the midget retinal ganglion cells. Indeed, our preliminary data from Experiment 2 shows that this effect persists and can be measured at the scale of individual cone photoreceptors.

Future experiments should be aimed toward looking more closely at the cone-specific effects of desensitization. For instance, it would be useful to know to what extent sensitivity is variable between individual cones in the periphery in order to measure directly their change in sensitivity following stimulation of nearby cones. This may reveal the specific wiring of individual cones to post-receptoral units, such that some cones are linked together and others are not, implying a sampling mechanism that is tiled with well-defined borders between receptive fields. Figure 2.9 shows an example of this in our preliminary data, where the contours encompass cones which were insensitive (d' < 1) after repeated stimulation of the adapted cones (cones 1-3 in the figure). Our results suggest that this paradigm, or a modification of it, could be used to measure the convergence and divergence of individual cone photoreceptors to post-receptoral units, and possibly reveal psychophysical signatures of receptive field tiling.

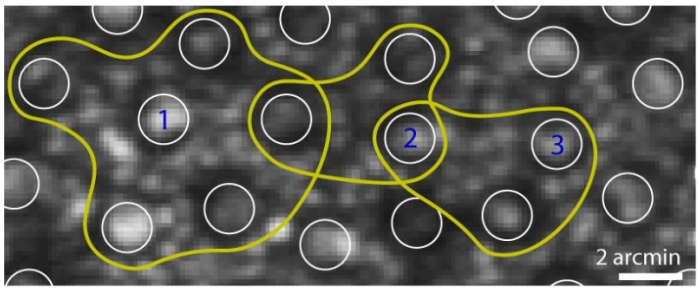

Figure 2.9. Mapping post-receptoral units from perceptual tiling. Cone photoreceptors are circled in white. The smaller cells surrounding the cones are rod photoreceptors. The yellow contours encompass the cones which had low sensitivity (d' < 1) after repeated stimulation of the adapter cones (1-3).

One weakness of the current single-cone study was the few trials delivered to each individual cone. An improvement on the current paradigm would be to minimize top-up adaptation to what is necessary; for example, including a top-up adaptation trial every few probe trials. This would relieve the subject of having to maintain strict fixation for the full duration of every trial, making the task easier, in addition to allowing for more probe trials to be collected in a more efficient manner. It would be useful to know whether desensitization of nearby retinal areas also persists, for example, by delaying the time between the offset of the adapting stimulus and onset of the probe.

Additionally, performing this experiment at a larger number of retinal eccentricities in several subjects would allow for assessment of the slope of the function relating the fraction of nearby cones with reduced sensitivity to retinal eccentricity. This should lend insight as to where in the post-receptoral visual system the spatial areas of

desensitization are imposed, since it is well known that cortical magnification steepens the slope of the function relating eccentricity and receptive field size in comparison to spatial sampling limitations inherited from pre-cortical sites (e.g., Levi et al., 1985; Duncan & Boynton, 2003; Levi, 2013), for example, in comparison to slopes relating grating acuity with eccentricity which follow closely with the midget retinal ganglion cell receptive field spacing (e.g., Thibos, et al., 1987a; Williams & Coletta, 1987; Wilkinson et al., 2016).

2.6 Acknowledgements

Thanks to my lab mates and collaborators for their helpful feedback on the work presented in this chapter. Particularly, Christy Sheehy assisted in collection of pilot data for Experiment 1 and provided valuable feedback. Brian Schmidt was a collaborator on Experiment 2 and provided feedback on experimental design and interpretation. Austin Roorda and Dennis Levi provided feedback on conception, analysis and interpretation. Additional thanks to Pavan Tiruveedhula for his technical assistance. We thank the participants of this study who were generous with their time and patience.

Chapter 3. Reconstructing Color Space from Targeted Cone Stimulation

3.1 Abstract

There are three types of cone photoreceptors, sensitive to short (S), medium (M) and long (L) wavelengths of light. The probability of light capture by a given cone type varies with wavelength, however, the same cone signal can be elicited by different combinations of wavelength and light intensity. This concept was formalized by William Rushton in 1972 as the principle of univariance. That cone signals are spectrally ambiguous implies that, in theory, it should be possible to create any chromatic or luminance percept with light of a single wavelength, provided that the intensity of the light is modulated in a way corresponding to the spectral topography of the cone mosaic.

Cone-targeted stimulus delivery in the AOSLO is typically done with 543 nm light. At this wavelength, L- and M-cone photoreceptors are nearly equally sensitive, and S-cones are insensitive. Spectral opponency along the red-versus-green dimension of theoretical color space (see Chapter 1) is achieved by comparisons of the activity in the L- and M-cone photoreceptors. L- and M-cone activity, when modulated together, correspond to a change in luminance relative to the background, while modulations biased toward L- or M-cones should result in changes in the red or green directions, respectively. In two previous publications, single L- and M-cone stimulation with 543 nm light was shown to be associated with reddish and greenish percepts when viewed against an achromatic background (Sabesan et al., 2016; Schmidt et al., 2018a), suggesting that color appearance can be reliably measured even at the level of single cones.

The work presented in this chapter seeks to extend on this work in two ways. First, we measured hue scaling responses to individual cones and pairs of adjacent cone photoreceptors, equated for detectability. We find that the color percept elicited by two cones is well predicted by a simple average of the two single cone color percepts, with cones of the same spectral type eliciting slightly more saturated percepts and cones of different type eliciting less saturated (whitish) percepts.

Second, we stimulated patches of cones of known spectral type with 543 nm light. When the light intensities delivered to each cone were biased toward either the L- or M-cone photoreceptors, chromatic percepts in the red-versus-green dimension were elicited. Color matching results reveal a linear relationship between L-versus-M biased stimuli and their position in MacLeod-Boynton chromaticity space, though the slope of this function was compressed. Additionally, discrimination thresholds of L- and M-cone-targeted stimuli show that only a small difference in L-versus-M activity is required to elicit distinct, discriminable, chromatic percepts.

Taken together, this work provides the framework for construction of the red-versus-green dimension of color space from cone-targeted stimuli with light of a single wavelength.

3.2 Introduction

The human retina contains three classes of cone photoreceptors, sensitive to long (L), medium (M) and short (S) wavelengths of the visible light. Though these cells are preferentially sensitive to different ranges of the visible spectrum, the same cone signal may arise through different combinations of wavelength and intensity in a stimulus. This is known as the principle of univariance, formalized by William Rushton in 1972.

This principle implies that the signal arising from stimulation of a single cone photoreceptor is spectrally ambiguous. Color information is computed by post-receptoral neurons which compare the relative activity across the three types of cones. It is generally thought that the parvocellular pathway, drawing its inputs from the midget retinal ganglion cells in the retina, is responsible for processing of chromatic signals which vary along the red-versus-green dimension of color space. This is achieved by neurons which draw excitatory inputs from either L- or M-cones and inhibitory input from their surrounds. The basic low-level circuitry supporting red-versus-green color vision is described in more detail in Chapter 1.1.

How might single cone photoreceptors contribute to conscious color perception? In several previous publications, authors employing AOSLO techniques for single-cone stimulation have demonstrated that single cone color percepts can be measured (Hofer et al., 2005b), are repeatable (Sabesan et al., 2016), and correspond to cone photoreceptor type when viewed against an achromatic background (Schmidt et al., 2018a). However, cone signals are rarely, if ever, elicited in isolation in more natural viewing conditions. Understanding the post-receptoral circuitry underlying red/green color vision requires information about how cone signals are combined by low-level neural processes to relay spectral information about the stimulus to later visual areas. Much work has been done in the fields of anatomy and physiology to characterize the neural connections between cells in the retina and LGN that supports color computations at later visual stages by the formation of three parallel processing streams, the magnocellular, parvocellular and koniocellular pathways. These pathways correspond to the cardinal mechanisms of color vision which compare activity in the cone photoreceptors along three dimensions, luminance, red/green, and blue/yellow, respectively.

These mechanisms have been shown to have behavioral relevance, particularly for chromatic discriminations (e.g., Boynton & Kambe, 1980; Krauskopf et al., 1982; Krauskopf & Gegenfurtner, 1992; Miyahara et al., 1993; Yeh et al., 1993; Smith & Pokorny, 1995), lending support to the idea that they provide the foundation for the perception of color.

To investigate these mechanisms behaviorally, physiologically relevant color spaces (e.g., MacLeod & Boynton, 1979) derived from cone excitation space are used to relate colored stimuli to post-receptoral processes. It has been shown that the cardinal axes of these spaces predict the tuning of post-receptoral neurons in the LGN (Derrington et al., 1984), lending support to their relevance in physiological mechanisms.

In the MacLeod-Boynton chromaticity diagram, a plane of equal luminance is extracted from cone excitation space. Since S-cones contribute little to luminance, a 2D plane in 3D cone excitation space, where the sum of L- and M-cone activity is equal, defines an equiluminant plane. The axes of the diagram are then L/(L+M) and S/(L+M), corresponding to red-versus-green and blue-versus-yellow. L/(L+M) represents the fraction of luminance (L+M) attributable to L-cones, and S/(L+M) compares S-cone activity to the total activity summed across L- and M- cones. A third dimension can be defined as (L+M), with cross-sections perpendicular to this plane containing chromaticities at equal luminance. It is believed that varying stimuli along one of these axes alone, while holding the others constant, isolates the corresponding post-receptoral mechanism in behavioral experiments (e.g., Krauskopf et al., 1982).

The above theory provides the framework for specifying cone-targeted stimuli in conventional chromaticity units. For the present work, we concern ourselves only with specifying stimuli along the L/(L+M) dimension since this does not require targeted modulation of S-cone activity, which is still not technically feasible in an AO system due to challenges imposed by transverse chromatic aberration (TCA) and light exposure safety limits (ANSI, 2014). L- and M-cone photoreceptors have approximately equal sensitivities to 543 nm light, while S-cones are effectively insensitive.

First, we extend previous work on single-cone color percepts to pairs of cone photoreceptors. Earlier work has demonstrated that single cone percepts are dependent on the background chromaticity (Schmidt et al., 2018b), and when viewed against an achromatic background L- and M-cone percepts reliably correspond to reddish and greenish hues, respectively (Sabesan et al., 2016; Schmidt et al., 2018a). These results are perhaps unsurprising in the context of modern color theory. A change in L- or M-cone activity relative to a white background should indeed elicit a +L/-M or -L/+M change in the relevant post-receptoral mechanisms, corresponding to the red and green directions in physiologically relevant perceptual color spaces. What is interesting, however, is that this relationship persists on such small spatial scales, implicating the single cone center receptive fields of midget retinal ganglion cells near the fovea, and suggesting that the spectral identity of foveal cones is preserved at later visual stages (Schmidt et al., 2018a).

It remains unclear, however, how the signals from a pair of cones might be combined to elicit a color percept representative of the cone-pair. For example, summation of intensity signals is thought to be summed across multiple photoreceptors by the larger, magnocellular projecting receptive fields in the retina and LGN, enhancing luminance sensitivity. The small receptive fields of midget retinal ganglion cells and parvocellular neurons do not preclude that these signals are summed at a later visual stage, for example, in area V1 of the cortex, or perhaps influenced by lateral connections between neurons in the retina and later visual system.

In Experiment 1, we performed hue scaling on single cones and pairs of cones, equating detectability across the two stimulus conditions. Our results demonstrate that the summation of L- and M-cone signals results in color percepts that are well-predicted by the average of the percepts mediated by each individual cone when stimulated

alone. However, L- and M-cones, when targeted together, tended to elicit desaturated (i.e., whitish) percepts. This is consistent with the visual system's interpretation of a uniform change in L- and M-cone signals against an achromatic background, representing a change in luminance more so than chromaticity. When two L- or two M-cones were stimulated together, percepts tended to be slightly more saturated than their average, possibly implicating nonlinear mechanisms which contribute to color appearance at later visual stages.

In Experiment 2, color matching and discrimination thresholds were measured for stimuli encompassing a patch of spectrally identified cones on the retina. When intensity was biased towards L-cone photoreceptors, the resulting percepts were reddish. Similarly, M-cone biased stimuli were perceived as greenish. When the computed L/(L+M) values representing the relative activity of L- and M-cones contributing to the percept were plotted against the MacLeod-Boynton chromaticity values of the matched colors, a linear, but compressed, relationship was revealed. Additionally, discrimination thresholds for these stimuli were measured in a 2-interval-forced-choice (2-IFC) experiment, demonstrating the observer's sensitivity for changes in chromatic contrast achieved by cone-targeted stimulation is similar to that of more conventional stimuli.

Together, these experiments represent the first steps toward the reconstruction of physiologically relevant color space with cone-targeted stimulation, which will provide a new platform to test the assertions of modern color theory in addition to novel questions about the post-receptoral circuitry subserving human trichromatic color vision.

3.3 Experiment 1: Summation of Color Signals Across Pairs of Cones

Three subjects (S10001, S20075 and S20076) participated in Experiment 1. Two of the three subjects (S10001, S20076) had spectrally classed regions of their cone mosaic from previous studies. The cone types for S20075 were unknown. The subjects' pupils were dilated and cyclopleged with 1% tropicamide and 2.5% phenylephrine ophthalmic solutions 15 minutes prior to the experiment.

All procedures were approved by the University of California, Berkeley Committee for Protection of Human Subjects and adhered to the tenets of the Declaration of Helsinki. All subjects signed informed consent documents before participating in the experiments.

3.3.1 Apparatus

The AOSLO used in these experiments is the same as described previously. For reference, see Roorda et al., 2002 and Harmening et al., 2014, or the preceding chapters of this document. Details of the apparatus specific to these experiments are described below.

The AOSLO used here is a multiwavelength system, where four wavelengths (λ = 543, 680, 840 and 940 nm) were selected from a supercontinuum light source (SuperK EXTREME, NKT Photonics, Birkerod, Denmark). The 940 nm wavelength was used for

wavefront sensing, 840 nm for retinal imaging, and 543 for cone-targeted stimulation. The 680 nm light was not used in the current experiment.

Wavefronts were measured with a custom Shack-Hartmann wavefront sensor and corrected with a deformable mirror (DM; DM97, ALPAO, Montbonnot-Saint-Martin, France). The intensities of the 840 nm and 543 nm wavelength used for retinal stimulation were modulated by fiber-coupled acousto-optic modulators (AOMs; Brimrose Corp., Sparks Glencoe, MD). A Maxwellian assembly was coaligned with the AOSLO beam path to relay light from a DLP projector (LightCrafter, Texas Instruments, Dallas, Texas) to the eye. The projector was used for presentation of a fixation target and stationary background. A camera (CMOS color board, DFM 61BUC02-ML, Imaging Source Inc., Charlotte, NC) was placed at the back end of the Maxwellian assembly and aligned to be conjugate with the pupil.

3.3.2 Stimulus & Procedure

Detection thresholds (85% frequency of seeing) were measured at 1-2 deg eccentricity for one- and two-cone conditions following established procedures (Harmening et al., 2014). First, a high SNR image from an average of 60-90 frames was used to identify the region of the retina where cones were previously identified as belonging to a particular spectral class. The experimenter then selected the center pixel of 8-12 contiguous cones from the reference image for testing. Thresholds were measured with a modified QUEST procedure (ZEST; Watson & Pelli, 1983; King-Smith et al., 1994). Each spot of light was monochromatic 543 nm, 0.35 x 0.35 arcmin (or 3 x 3 pixels) and was raster scanned against a low-photopic white background (40 cd/m^2). In the case of paired stimulation, two spots of light, each 0.35 x 0.35 arcmin, were delivered on each stimulus frame. Stimuli were presented over approximately 500 ms (15 frames). The subject initiated each trial with a button press. An auditory beep indicated the start of the trial and then a stimulus was delivered to the center of either one or two of the selected cones. The subject reported whether she saw the flash with a single yes/no button press. No feedback was given.

Each session consisted of four interleaved staircases. Two staircases measured single cone thresholds and two measured paired stimulation thresholds. Each staircase terminated after 35 trials. Stimulus order was randomized. On each trial, one cone or one pair from the preselected group was targeted. Therefore, these measurements reflected an average threshold over the 8-12 cones. Thresholds for specific cones or pairs could not be estimated from this data, since each location was only targeted on a handful of trials. This approach was an efficient way to approximate thresholds over a larger group of cones and allowed us to equate detectability between the one- and two-cone conditions.

A fraction of the 8-12 cones selected at the start of the experimental session were separated by multiple cones. Variable distances between cones in the selected region was a potentially confounding factor. To minimize its effect, threshold measurements were only made between pairs of cones separated by no more than one cone or roughly two arcmin between the center of each cone. Cones at this eccentricity

are about 1 arcmin in diameter. At the end of each session, threshold was estimated from each staircase using the QUEST mean procedure (King-Smith et al., 1994). This generated four threshold estimates: two for single cones and two for pairs. We then averaged thresholds within each condition and compared the threshold energy between two- and one-cone conditions.

Stimulus conditions in the appearance task were identical to the detection task. Experimental sessions again began by capturing a high SNR image of the subject's cone mosaic. From that image, three contiguous cones were selected for study. By selecting contiguous cones, we assured that cones were never separated by more than one cone (a center-to-center distance of approximately 2 arcmin), which was the limit we set in the detection task. The subject initiated each trial with a button press, which was accompanied by an audible beep. On each trial, one or two of the selected cones were stimulated. The light energies used for one- and two-cone stimuli were set to each subject's previously determined detection thresholds. The recorded frequency of seeing in this task was 85%, as expected. Each cone and pair was tested 12 times for a total of 72 trials per session ([3 cones + 3 pairs] x 12 trials). Trials were randomly interleaved.

After each trial, subjects judged the hue and saturation with a scaling procedure (Gordon et al., 1994; Schmidt et al., 2018a). The subject indicated the percent of red, green, blue, yellow and white contained in each stimulus using five button presses such that each press represented 20% (5x20%=100%). This response scheme is called five category scaling. One subject, S20075, used an alternative response scheme called 4+1 category scaling (Gordon et al., 1994). In this procedure, the subject first rated saturation on a 7-point scale. Then, hue was rated with five button presses using only red, green, blue and white. It has been shown previously that these two procedures produce very similar results, but some subjects prefer the 4+1 category approach (Gordon et al., 1994). Both results were converted into a common metric space as described below.

In both the threshold and hue scaling portions of the experiment, pupil tracking was performed in real time to monitor pupil position and minimize any changes in TCA due to pupil displacements (Boehm et al., 2019). The tolerance for pupil tracking was set to 0.15 mm, corresponding to approximately half an arcmin of angular offset due to changes in TCA, less than the size of a cone photoreceptor at this eccentricity.

3.3.3 Results

We first measured detection thresholds in the one- and two-cone conditions in order to control for differences in sensitivity in the hue scaling portion of the experiment. Threshold energy (threshold intensity multiplied by stimulus area) for achieving 85% frequency of seeing (FoS) was determined with an adaptive staircase procedure. Each subject completed at least four sessions of the detection task, and each session contained two staircases per condition (one- and two-cone stimuli). At the end of the session, we averaged the threshold estimates for each condition and compared them. The values reported in Table 3.1 are the ratio of two:one cone threshold energies. This ratio equals one when the same energy (i.e., number of photons) was required to

achieve threshold in both conditions. Values below 1 indicate less energy was necessary in the two-cone case to achieve 85% FoS. The results from our three subjects were all close to 1, which means, at threshold, each cone in a pair received approximately half the photons of the one-cone case. Thus, the total energy was roughly equal across conditions and was consistent with linear summation. In subsequent experiments, individual and pairs of cones were stimulated at these threshold energies. Therefore, color judgments were made under conditions in which detection mechanisms were equally sensitive to all stimuli.

Table 3.1. Two:one cone threshold energy ratios

Subject	*N*	*mean*	*standard dev.*
S10010	4	0.98	0.09
S20075	4	1.05	0.12
S20076	11	0.92	0.1

The raw color appearance dataset contained a total of 4,968 trials completed by three subjects. Before analyzing the data, unusable trials due to stimulus placement errors were removed. The location of the stimulus on each frame was recorded in real time with a digital cross written into the video frames. To identify unusable trials, a delivery error was computed as the standard deviation of the stimulus location over the 15 frames (500 ms). Trials with delivery error greater than 0.35 or less than 0.01 arcmin (values below 0.01 do not occur naturally) were considered unusable. In those trials, we could not be confident that the correct cone was targeted. After removing bad trials (3.6%), 4,788 trials remained for further analysis.

The remaining trials had a mean delivery error of 0.19 arcmin (standard deviation = 0.036 arcmin), which was about 1/5 of the diameter of cones at the eccentricities tested. Trials that either targeted an S-cone or were not detected were also removed. The remaining dataset contained trials in which individual or pairs of L- and M-cones were stimulated (N=4,057). Finally, cones and pairs which had fewer than four good trials were not analyzed due to low statistical power. Most cone pairs (71%) had at least ten good trials.

Raw scaling data was transformed into a uniform appearance diagram (Gordon et al., 1994). For each trial, the number of red, green, blue, yellow and white button presses were converted to a percentage of the total button presses (five). A green-red dimension was computed as *gr* = (*green*% - *red*%) / 100% and a yellow-blue dimension as *yb* = (*yellow*% - *blue*%) / 100%. Saturation was computed from a sum of the absolute values of the green-red (gr) and yellow-blue (yb) dimensions (| yb | + | gr |). In 4+1 category scaling, each color category was scaled by the saturation judgment, which was normalized to range from 0-1. For example, consider a spot that was rated 60% red and 40% yellow at 40% saturation. Red and yellow, in this case, would be scaled down to 24% and 16%, respectively.

We next quantified color appearance of one- and two-cone spots presented at the measured threshold. A total of 198 pairs were tested across three subjects. Hue and saturation scaling data were transformed into a color opponent representation described

in the previous paragraph. In this representation, saturation is expressed as the distance from the origin (in city block metric). A maximally saturated report falls along the outer diamond, and a pure white response falls at the origin.

The results of one session are plotted in Figure 3.1. In this example, Cone 1 was an M-cone and had a bias towards green (positive *gr* value). Cone 2 was an L-cone and elicited predominantly white reports. Cone 3, also an L-cone, was rated reddish-yellow (orange) with medium saturation (negative *gr* value, positive *yb* value). The percepts elicited when these cones were stimulated in tandem may provide insights into how the visual system combines color information across photoreceptors. In the example, when Cone 1 was targeted together with either Cone 2 or Cone 3, the average report had no clear color bias. In comparison, when Cone 2 and 3 were targeted, they elicited a medium-saturated orange report. Below, we analyze the results from all sessions and subjects.

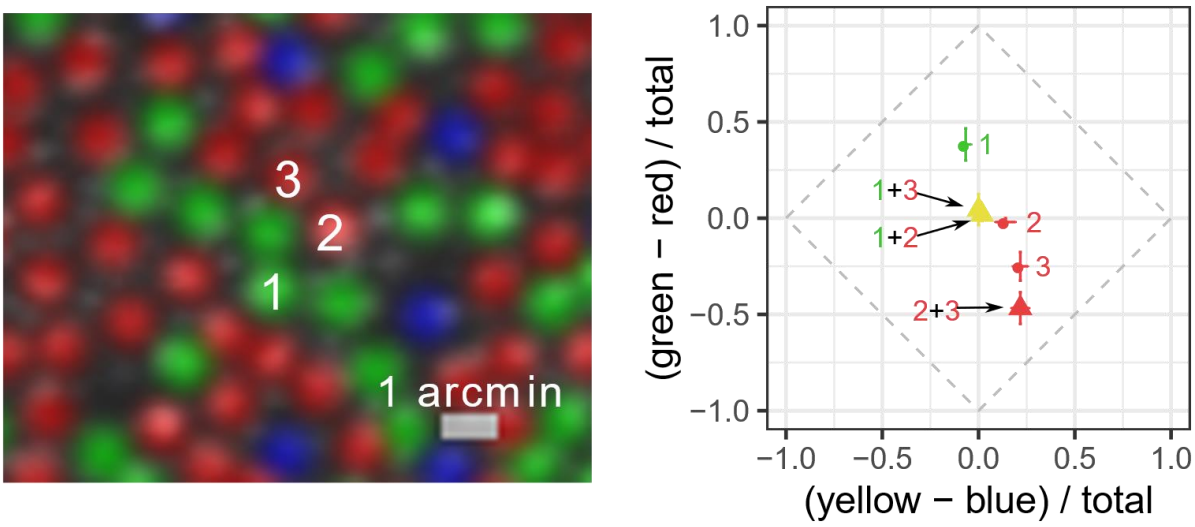

Figure 3.1. Measuring color appearance in one- and two-cone conditions. (A) Example AOSLO cone selection image (S20076; 1.5 deg eccentricity). Groups of three cones were targeted during each experimental session (543 nm; 500 ms). Cones have been pseudo-colored to reflect their spectral type (red = L-cones, green = M-cones, blue = S-cones). The smaller, gray-scale blobs in between cones are rod photoreceptors. (B) Mean hue and saturation reports for one- (circles) and two-cone (triangles) conditions. Numbers correspond to labels in (A). Results are plotted in a uniform appearance diagram (UAD), which represents bias towards the primary hues. An unbiased, or pure white, response falls at the origin. Green = M-cone(s), red = L-cone(s), yellow = L+M-cone pair. Error bars indicate +/- SEM.

We first grouped each trial based on which cone or pair was probed. The results are reported in Figure 3.2A separately for each subject. Each point in these plots represents the mean response measured from a single cone or pair. This plot illustrates the variability in responses across cones/pairs and between subjects. There are a few features to note. Firstly, there were individual differences in color responses: S20075 used blue more frequently than the two other subjects, and S10001 did not report yellow on any trials. However, the general patterns are similar. Most of the variance was found

along the green-red dimension, and there were few points that fell in the bluish-red or greenish-yellow quadrants.

Secondly, in two subjects with classified mosaics, we found L-cone-targeted trials were red biased, while M-cones were green biased. These patterns were similar to previous reports from single-cone (Sabesan et al., 2016; Schmidt et al., 2018a and 2018b) and large-field studies (De Valois et al., 1997).

Thirdly, within a single subject, there was considerable variability between cones and pairs with the same spectral sensitivity. Similar variability in single-cone-mediated percepts has been reported previously (Hofer et al., 2005b; Sabesan et al., 2016; Schmidt et al., 2018a and 2018b). This is the first report of variability in percepts elicited from pairs of cones.

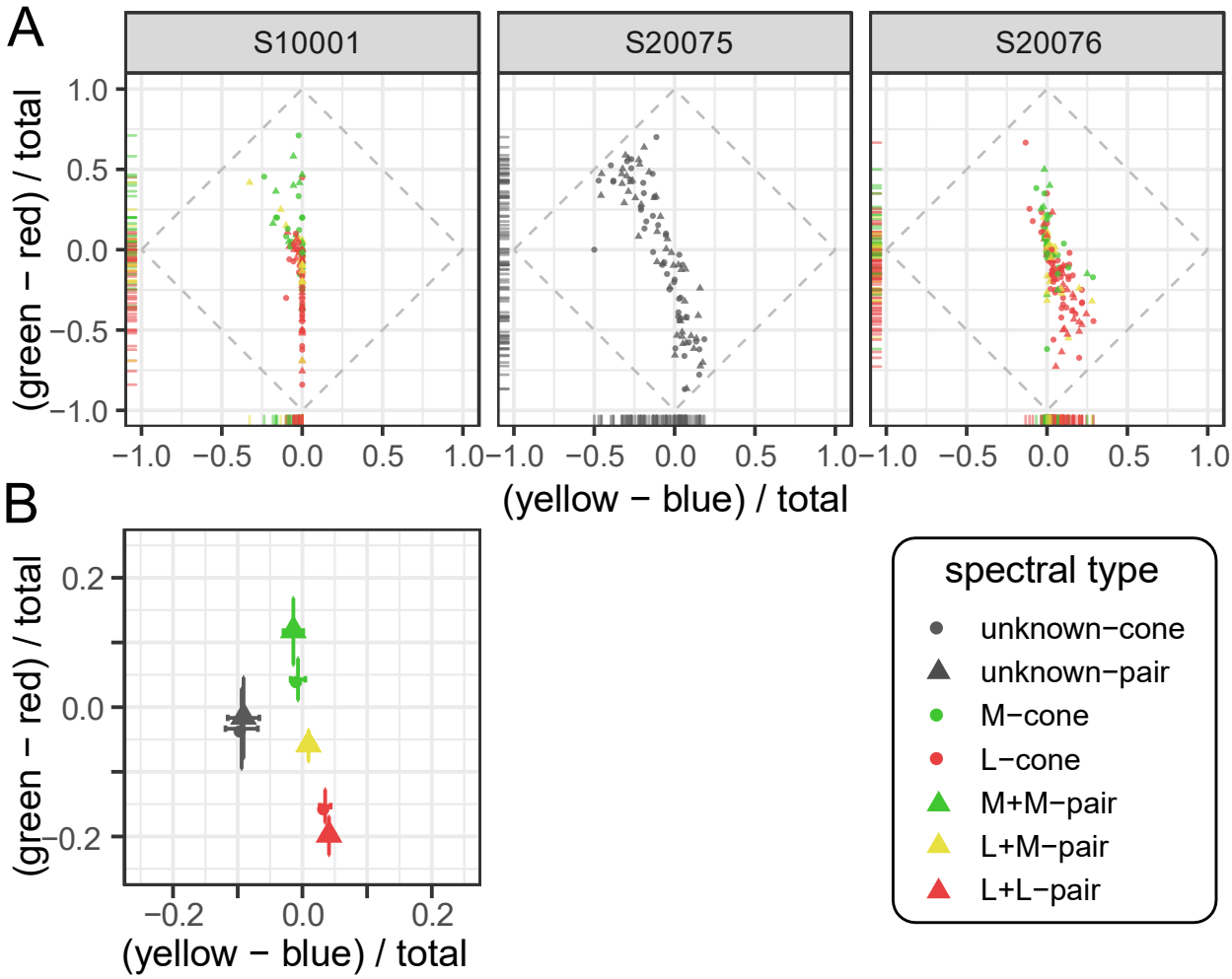

Figure 3.2. Number and type of cones probed influence color reports. (A) Average response from each cone and pair targeted in three subjects. Data was transformed into an opponent representation: yellow-blue and green-red. Marginal distributions are represented along each axis with rug plots. (B) The data from each subject was further grouped according to the cone type tested. The mean and standard error of each group are represented.

To better appreciate the influence of cone type and number of cones targeted on color reports, data was pooled across subjects and grouped according to the type of cone or pair probed. The mean and standard error for each group is shown in Figure 3.2B. When an individual or pair of M-cones was targeted, the average *gr* response was greater than zero, indicating a bias towards green. In comparison, the average L-cone(s) elicited biases towards red and yellow. Together, these cone type specific differences in color reports were consistent with a predictive relationship between cone type and color report, as previously reported (Sabesan et al., 2016; Schmidt et al., 2018a). Two cones with the same photopigment tended to elicit slightly more saturated reports than single-cone trials. On the other hand, one L- and one M-cone-targeted together tended to produce desaturated reports.

Figure 3.2A illustrates that color reports varied even between cones with the same photopigment. Some L-cones, for instance, elicited saturated red reports, while a majority produced white or desaturated red. We next asked whether this variability could be explained by features of the mosaic. Specifically, can we predict whether an L-cone will produce a saturated or a desaturated red based on the surrounding cone types? And in the case of paired stimulation, did the distance between the two cones influence color appearance? The existence of such relationships could implicate low-level neural mechanisms, such as chromatically-opponent ganglion cells, in this behavior.

The local neighborhood surrounding a cone is thought to be an important factor influencing color percepts associated with small spots (Brainard, 2015). To test this prediction, we found the number of L-cones in the immediate neighborhood of each cone/pair. In keeping with prior work (Sabesan et al., 2016; Schmidt et al., 2018a and 2018b; Tuten et al., 2017) the local neighborhood was defined as the six nearest cones. In the case of a pair, the immediate neighborhood for each cone was found separately, and duplicates were removed. We did not find a significant correlation between the number of neighboring L-cones and the mean response in any dimension (*gr*, *yb* or saturation; $p > 0.05$).

The distance separating two cones in a pair may also be an important factor influencing appearance. However, this measure was not correlated with hue or saturation reports ($p > 0.05$). Cone pairs were never separated by more than one cone, which may explain why we did not detect a relationship. Moreover, subjects verbally reported that the flashes always appeared as a single uniformly colored dot. In the future, systematically varying the distance between stimulated pairs will be an informative exercise. At a certain critical distance, the spots of light will be seen as two spatially distinct dots. It is less clear at what distance the spots will be perceived as two distinct colors.

While features of the mosaic and the physical stimulus did not predict color reports, we hypothesized that the responses recorded following individual cone trials would be predictive of paired stimulation. To assess this prediction, we matched the mean response from each cone pair with the mean report from each cone tested individually. We then fit an averaging model to the data. Behavioral reports, *r*, from two-cone stimulation were predicted by an average of the individual responses: $r_{1,2} = (r_1 +$

r_2)/2. Predictions were computed for *gr* and *yb* dimensions separately. Figure 3.3 shows the measured responses plotted against these predictions. An average of the single-cone responses was a good fit to the data in both the *gr* (R^2 = 0.73; $p < 0.01$) and *yb* (R^2 = 0.75; $p < 0.01$) dimensions. The best-fit lines had slopes close to unity, which further supported the conclusion that an average of individual responses was a good model.

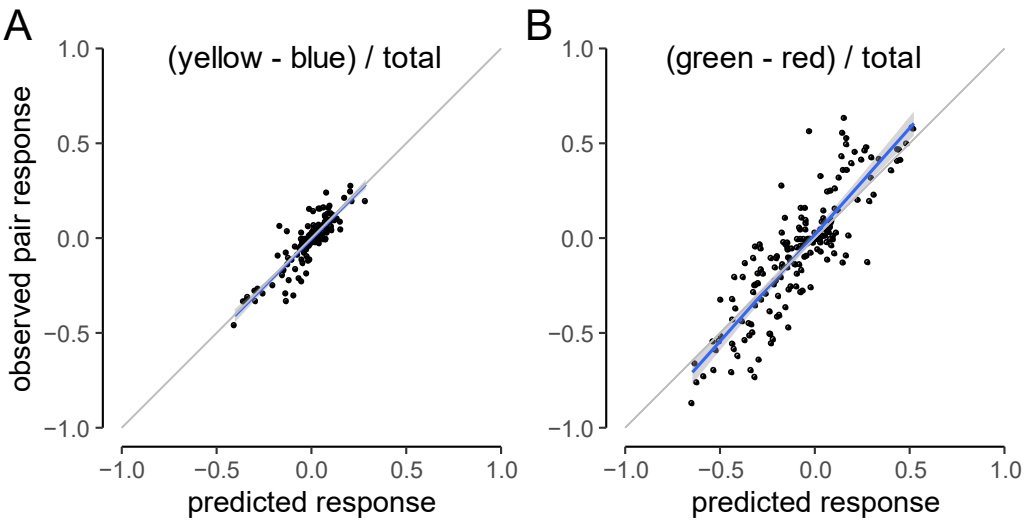

Figure 3.3. An average of individual responses predicts paired stimulation. The response measured for each pair was predicted from the average response of the two cones tested individually. Blue line represents the best-fit line, with 95% confidence intervals indicated by gray shading. (A) Blue-yellow (*by*) dimension. Best-fit line: $yb_{observed} = 0.004 + 1.002yb_{predicted}$. (B) Green-red (*gr*) dimension. Best-fit line: $gr_{observed} = 0.02 + 1.12gr_{predicted}$. Gray lines indicate unity slope. Analyses include data from all three subjects.

While an averaging model captured a large fraction of the variance in two-cone color judgments, there were some pairs that deviated substantially from the best-fit line. We wondered whether these deviations from an average might be predicted by the sub-class of the two cones. For instance, were L+M-pairs more likely to deviate from the model? To answer this question, we found the saturation for each pair and compared it to the saturation predicted by the average of the two cones probed alone (Figure 3.4A). A unity line represents the condition where the observed saturation judgment was predicted exactly by an average of individual responses. Notice that the L+L and M+M pairs tended to lie above the unity line, particularly at higher saturation values. In contrast, the L+M pairs often fell below the line. These observations indicate that cones of the same spectral type produced slightly more saturated reports than predicted by the average of their individual responses, while pairs of opposite type elicited desaturated (more whitish) reports.

We quantified this trend directly by taking the difference between the observed and predicted saturation judgments. The results are illustrated in a histogram (Figure 3.4B). Student's t-tests confirm that the L+L and M+M pairs were significantly more saturated than an average of their individual responses (mean = 0.072, $t_{78} = 4.2$, $p <$

0.01). In comparison, the mean difference for L+M pairs approached significance in the opposite direction (mean = -0.034, t_{56} = -1.9, p = 0.06). These pairs were slightly more likely to be less saturated than predicted by an average of the individual responses. Across all of the unclassified cones tested in S20075, the average pair was more saturated than an averaging model predicted (mean = 0.123, t_{46} = 4.0, p < 0.01). It is worth noting that this dataset contains all combinations of L- and M-cones. Had L+M pairs been removed from the S20075 dataset, the difference between observed and predicted saturation judgments may have been even more pronounced.

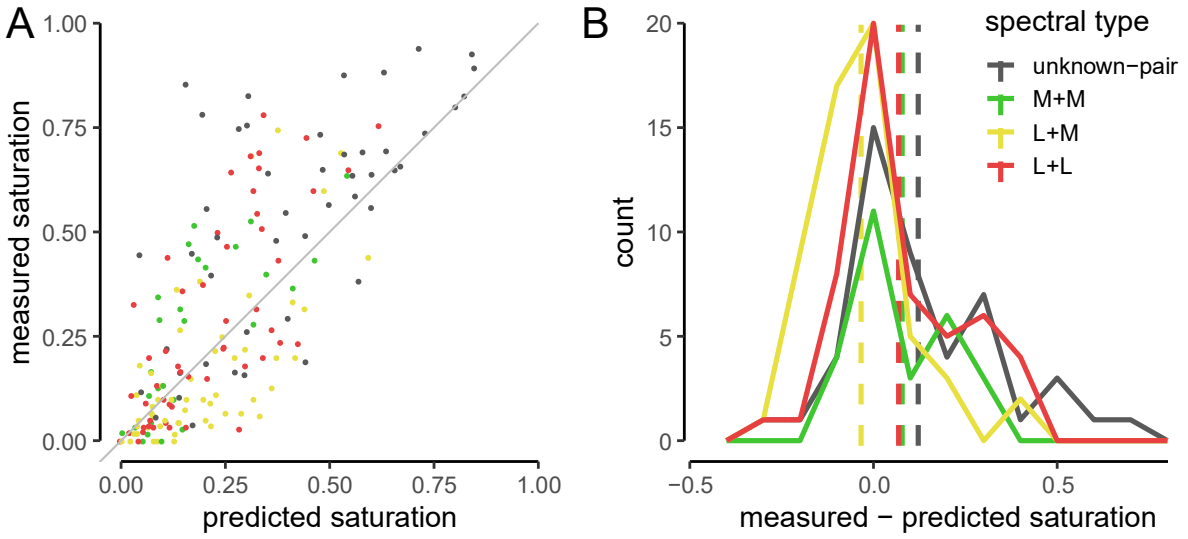

Figure 3.4. Cone pairs with the same spectral sensitivity produce higher saturation ratings than predicted. Saturation judgments were predicted for each measured cone pair with a linear average model. (A) Model predictions were plotted against the mean saturation ratings measured for each pair. The gray line indicates a prediction that matches the measured judgment exactly. (B) Distribution of measured saturation judgments minus predicted responses. Dotted lines indicate the mean of each distribution. Colors indicate cone type of pair: red = L+L, green = M+M, yellow = L+M, gray=unknown.

3.3.4 Discussion

In Experiment 1, small spots of light were targeted to individual or pairs of cones and color appearance was quantified by hue scaling. We report here that both the number and spectral type of targeted cones influenced color percepts (Figure 3.2). Pairs of cones elicited percepts that were predicted by an average of individual responses (Figure 3.3). When cones of different sensitivity (L+M) were targeted, their responses tended to cancel, or create a desaturated percept. When two cones from the same subclass were probed, their responses were generally consistent with their spectral sensitivity: on average, two L-cones appeared red and two M-cones appeared green. These findings were consistent with the involvement of a spectrally-opponent mechanism(s) (Finkelstein & Hood, 1982; Finkelstein & Hood, 1984; Finkelstein 1988).

The most surprising finding of the present work was that when two cones of the same type were probed, subjects reported seeing a hue that was more saturated than

an average of the two probed alone (Figure 3.4). This was unexpected because the stimuli were adjusted to be equally detectable (Table 3.1). Thus, while a detection mechanism was equated across conditions, a second, color sensitive mechanism, was influenced by activity in a second cone and saturation was systematically elevated.

Why would two cones produce a more saturated percept when targeted together? The visual system generates color by comparing relative activity in the three cone classes. For example, a green surface excites M-cones more than L- or S-cones. Activation of a single M-cone also elevates the activity in M-cones relative to L+S and thus may appear green. However, activity in a single M-cone could equally be caused by a broadband (white) spot of light, because individual cones are sensitive to changes in wavelength and intensity (Rushton, 1972). Thus, small spots, like the ones presented here, force the visual system to select, from multiple possible interpretations, the physical stimulus that most likely generated the incoming pattern of activity. This uncertainty was likely one reason why single M-cones were sometimes associated with whitish percepts and sometimes greenish percepts (Figure 3.2).

The finding that even cones with the same photopigment elicited different percepts suggests that the visual system uses prior experience when making this guess (Brainard et al., 2008; Schmidt et al., 2018a). Stimuli not confined to one or two cones, for example, larger stimuli or small spots which are allowed to move across the retina in a manner consistent with fixational eye motion, should provide the visual system with more information about the stimulus. Thus, the number of possible interpretations by the higher-level visual system decreases. We hypothesize that when two M-cones were activated with an equally intense light the balance was tipped towards the interpretation that the physical stimulus was a uniform, medium-wavelength surface. In other words, activity in a second M-cone slightly decreased the likelihood that the physical stimulus was a broadband (achromatic) spot. Together, these observations suggest that the visual system uses a combination of spectral opponency and prior experience to assign color to small spots.

One possible mechanistic explanation for the increased saturation we observed in two-cone stimulation (Figure 3.4) is the presence of a saturating nonlinearity before cone signals are summed. Horwitz and Hass (2012) described color cells in primary visual cortex that compressed cone inputs before summation in a manner consistent with our observations. In comparison, our threshold measurements followed a linear summation model, which was consistent with the area of complete summation (Ricco's area) at this eccentricity (Volbrecht et al., 2000). Together, our observations support the idea that separate neural mechanisms mediated these two tasks (King-Smith & Carden, 1976), potentially implicating the parvo- and magnocellular pathways, which are thought to provide the basis for detection of chromatic and luminance differences, respectively (Lee et al., 1990; Lennie et al., 1993).

There were a few factors potentially confounding the present work. Firstly, different stimulus intensities were used in one- and two-cone conditions. In order to equalize detection, each cone in a pair was stimulated with about half the intensity of single-cone trials. An implicit assumption in the averaging model (Figure 3.3) was that

hue and saturation judgments were not influenced by intensity. Our findings would require a more complicated model if this assumption was invalid. We have previously found that color judgments in single-cone conditions are approximately constant over the range of intensities used in this study (Schmidt et al., 2018a). Therefore, we do not believe that stimulus intensity influenced our results since it was equated across cones in the two-cone condition.

Secondly, we cannot rule out the possibility that two-cone appearance judgments were influenced by a weighting mechanism at the site of spatial pooling (Li et al., 2014). However, in our study, two-cone appearance judgments were well predicted by a simple average of their individual activations (Figure 3.3). Consequently, if the chromatic mechanism weighted cones prior to summation, those weights were small and had only a minimal effect on the measured responses.

A final possible complication was that detection judgments were not made in a cone- or pair-specific manner. We measured average cone/pair thresholds drawn from groups of 8-12 cones. Bruce (2016) measured detection summation between cone pairs at a similar eccentricity and found that a subset of pairs followed a sublinear summation rule. We cannot rule out the possibility that some of the pairs in our dataset also followed this strategy. However, Bruce's (2016) findings were in the opposite direction of our appearance results. A fraction of their cone pairs were less sensitive than either tested alone. Thus, these small deviations cannot explain the increased saturation we found during paired stimulation trials.

The approach used here of targeting small groups of cones provides a means of testing more sophisticated hypotheses about early-stage neural mechanisms and their role in shaping visual experience. Our evidence supports the idea that the appearance of small spots is dependent upon both the number and type of cones targeted. These observations are consistent with different strategies for combining information within versus across neuronal subclasses. In the future, scaling these experiments to larger groups of cones will provide important clues about how the visual system extracts color and spatial signals in more naturalistic settings. In Experiment 2, described in the following sections, we present preliminary color matching and chromatic discrimination data for cone-targeted stimuli over patches of approximately 200-250 cone photoreceptors in an effort to reconstruct the red/green dimension of physiologically relevant color space with a single wavelength.

3.4 Experiment 2: Color Matching and Discrimination with Cone-Targeted Stimulation

One subject (S20075) with a classed region of the cone mosaic participated in Experiment 2. The subject’s pupil was dilated and cyclopleged with 1% tropicamide and 2.5% phenylephrine ophthalmic solutions 15 minutes prior to the experiment.

All procedures were approved by the University of California, Berkeley Committee for Protection of Human Subjects and adhered to the tenets of the Declaration of Helsinki. All subjects signed informed consent documents before participating in the experiments.

3.4.1 Apparatus

Details of the apparatus used for retinal imaging and cone-targeted stimulus delivery are the same as described for the previous experiment.

For color matching, the projector was calibrated with a PR650 spectroradiometer. Color calibration was performed using the Stockman and Sharpe (2000) cone fundamentals scaled so that L+M = luminance and S peaks at unity.

3.4.2 Stimulus & Procedure

Cone types were identified by creating a normalized frame from the average of 60 video frames and registering this to an image with previously identified cone types from densitometry (Sabesan et al., 2015). A search box surrounding the targeted position in the normalized image was used to identify cone types within a 14 x 27 arcmin patch of retina containing roughly 250 cones. The stimulus patterns for L- and M-cones were generated separately by placing small (0.33 x 0.33 arcmin) squares at the centers of each identified L- or M-cone. An example is shown in Figure 3.5. In this example, 266 cones are identified in the patch, with 165 L-cones and 88 M-cones.

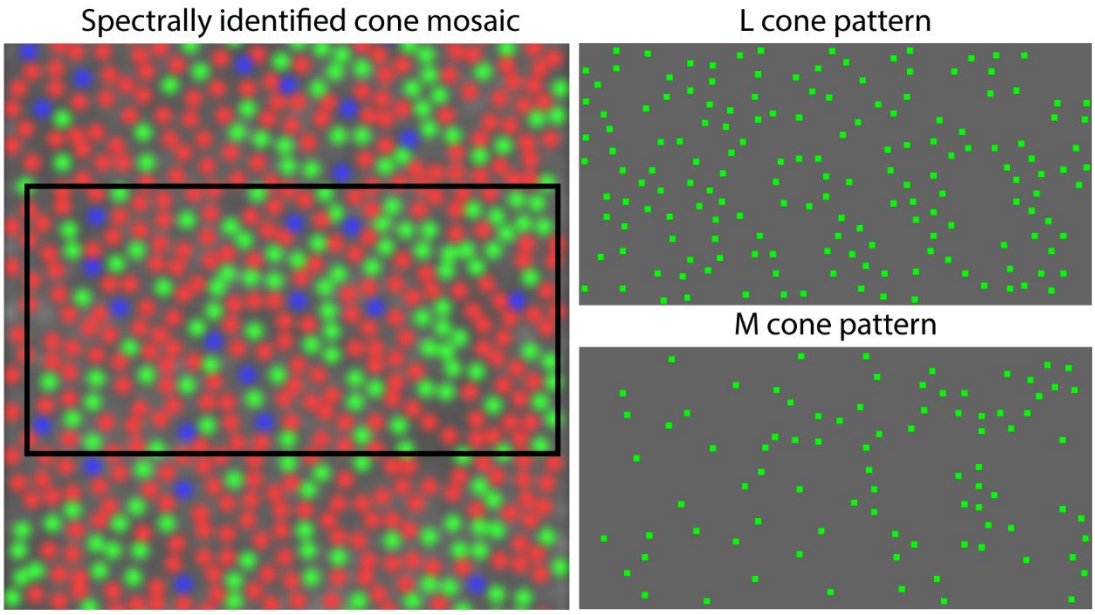

Figure 3.5. Example of multi-cone-targeted chromatic stimuli. L-cone and M-cone patterns (right panels) were generated by identifying L- and M-cones in a targeted patch of retina (left panel), and scaling the intensities of each pattern separately. The sum of the two patterns was used as the stimulus. Stimuli are drawn to scale.

In the right column of Figure 3.5, L- and M-cone patterns are shown with arbitrary intensities. For color matching and discrimination, the intensities of each pattern were scaled depending on the experimental condition (explained in further detail below), and the two patterns were then summed to create the full stimulus pattern.

Different L- and M-pattern intensities (L_I and M_I) were presented to the subject in order to vary the chromatic signal (L-versus-M), but so that average intensity across both L- and M-cones (L+M) was kept constant. This was achieved by designating the average cone-targeted luminance (*lum*, in arbitrary units, or a.u.) as 0.1 a.u. on a normalized unit scale, where 0 a.u. is the background and 1 a.u. = 5.2 logTd, the maximum output of the current AOSLO setup. Chromatic (L-versus-M) stimuli were then defined as the fraction of luminance (L+M) attributable to each cone type, *L/(L+M)* or *M/(L+M)*, consistent with the convention of MacLeod and Boynton (1979), though it should be noted that at this point, the contribution of the background to L- and M-cone activity is not considered and we therefore refer to these as simply $L_{fraction}$ and $M_{fraction}$ for clarity. (We consider the background and a representation of conventional MacLeod-Boynton units in more detail in Results 3.4.3.) The intensities delivered to each cone are then:

$$L_I = (L_{fraction} \times lum \times (n_L + n_M)) / n_L ,$$
$$M_I = (M_{fraction} \times lum \times (n_L + n_M)) / n_M , \qquad \text{(Equations 3.1-2)}$$

where n_L and n_M are the numbers of L- and M-cones identified in the patch of retina, and $1\text{-}L_{fraction} = M_{fraction}$.

The cone-targeted stimuli described above were presented against a background field from a projector coaligned with the AOSLO beam path in Maxwellian view (see Apparatus 3.4.1). The background chromaticity coordinates were found to be L/(L+M) = 0.68 and S/(L+M) = 0.02.

The observer completed two tasks, color matching and chromatic discrimination, with cone-targeted stimuli viewed against this background, described in the following paragraphs.

In the color matching task, a field matched in size and eccentricity was presented using light from a projector (Figure 3.6A). The subject viewed the projector stimulus continuously, and the cone-targeted stimulus was presented to the subject for four frames (30 Hz frame rate) whenever the subject initiated its appearance with a keypress. The subject made a color match by adjusting the chromaticity and luminance of the matching field until it appeared indistinguishable from the cone-targeted stimulus. The subject made 200 color matches over the course of four experimental sessions (50 trials each session). Matches were made to ten $L_{fractions}$ in each experimental session. Some $L_{fractions}$ were repeated across experimental sessions, with matches made for a total of 37 unique $L_{fractions}$ across the four sessions.

For matches outside of the projector gamut, light from the red primary of the projector (peak λ = 625 nm) was added to the cone-targeted stimulus (synchronized in both time and space). The amount of red light needed to bring the stimulus back into gamut was then used to estimate the out-of-gamut L/(L+M) values. Only one experimental session included this protocol for out-of-gamut matches. In the other three sessions near-gamut-limit matches were excluded from analysis.

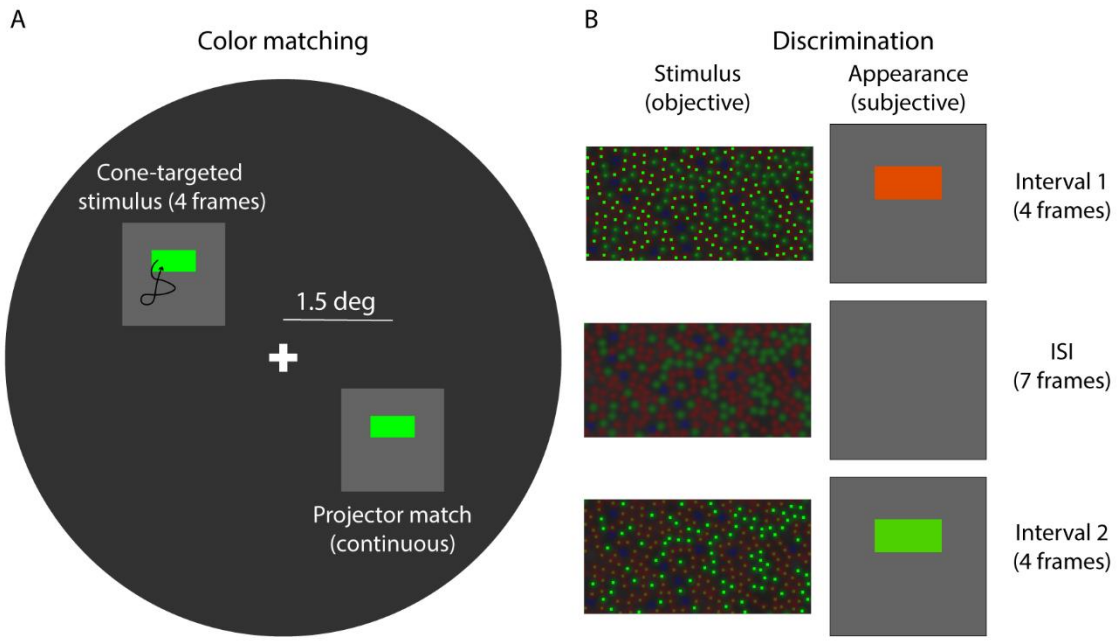

Figure 3.6. Color matching (A) and discrimination (B) of cone-targeted stimuli. Panel A is a schematic of the stimulus used in the color matching task. The cone-targeted stimulus was stabilized on the retina (shown by the arrow indicating that the stimulus moved with the eye) and appeared for four frames (30 Hz frame rate) whenever the subject initiated its appearance with a button press. The projector matching field was viewed continuously at an equal and opposite eccentricity. Panel B shows example stimuli from the discrimination experiment. Stimuli appeared in two four-frame intervals (ISI seven frames). Stimuli in this experiment were the same size as the cone-targeted stimulus in (A). The left column shows the objective stimulus, where cone-targeted intensities were biased to L-cones (top) or M-cones (bottom), resulting in reddish and greenish percepts (right column, subject view), respectively. This highlights the large difference in chromatic percepts that can theoretically be achieved, however, note that the differences in chromaticity between the two intervals was generally not as large as in this illustration.

In the discrimination task, the subject made discriminations between pedestal stimuli, with $L_{fractions}$ of 0.2022, 0.3667, 0.4778, 0.5588 or 0.6800, and a test stimulus, which contained a small change in $L_{fraction}$ relative to the pedestal. The five pedestal values were tested in separate experimental sessions. Figure 3.6B shows example stimuli and time-course of a trial in the discrimination task. In a 2-interval-forced-choice (2-IFC) paradigm, the subject viewed the pedestal and test stimuli for four frames each, with seven frames between stimuli (the inter-stimulus-interval, or ISI). The pedestal stimulus appeared randomly in either the first or second interval, and the test stimulus (pedestal +/- $\Delta L_{fraction}$) appeared in the other interval. The subject used the arrow keys on a keyboard to indicate whether the first or second interval contained the stimulus which appeared “greener (or less red).” A modified QUEST adaptive staircase procedure (ZEST; Watson & Pelli, 1983; King-Smith et al., 1994) was used to find the threshold difference required to detect the interval with lower $L_{fraction}$ correctly 75% of the time. Four pseudo-randomly interleaved staircases (each with 35 trials) were used, two for $+\Delta L_{fraction}$ (an increment in L/(L+M)) and two for $-\Delta L_{fraction}$ (a decrement in L/(L+M)).

Additionally, in two of the pedestal conditions ($L_{fraction}$ = 0.2022, 0.3667), we measured discrimination thresholds for scrambled cone arrays. Stimuli in this case were the same as for chromatic stimuli, except that the two stimulus arrays were randomly assigned to the mosaic, preserving the L:M ratio of cones in the patch. The subject in this case did not report seeing a uniform chromatic percept, but, rather, a "muddled achromatic intensity pattern." The subject indicated their response as to which interval appeared to have the highest intensity variation (i.e., least uniform) in the muddled pattern in order to identify the intervals with the larger intensity difference assigned to the random cone arrays. This was introduced as a control condition to see if the subject could make similar discriminations between stimuli without chromatic contrast.

Each pedestal was tested in one session (including four staircases), except in the case of chromatic stimuli with $L_{fraction}$ = 0.4778, which was tested twice (eight staircases). For the most extreme pedestal, $L_{fraction}$ = 0.2022, decrement staircases could not be reliably measured (due to gamut constraints). Only the increment staircases were considered for analysis in this case.

3.4.3 Results

In our analysis, we first considered how cone-targeted stimuli of this kind might be represented in MacLeod-Boynton (1979) chromaticity space. Following standard color mixing principles, the relative luminances of the background and cone-targeted stimuli sets the reference point from which the stimuli will deviate along the L/(L+M) axis (Figure 3.7). The background is composed of the IR imaging light (840 nm), leak from the visible stimulus channel (543 nm), and the addition of projector light to form an achromatic background (Figure 3.7A). The background was estimated to be L/(L+M) = 0.68 and S/(L+M) = 0.02. This is shown as the black square plotted in Figure 3.7B.

A standard mixing line (dashed line in Figure 3.7B) can be specified between the background chromaticity and the 543 nm stimulus wavelength, represented by the green cross. The point at which the matches intersect with this line should represent the case where the L-, M-, and S-cone excitations produced by a 543 nm monochromatic light source are reproduced with cone-targeted delivery. This is the point from which AOSLO cone-targeted stimuli will deviate along the L/(L+M) axis of MacLeod-Boynton (1979) chromaticity space, with its position reflecting the relative contributions of the background and cone-targeted stimulus to the apparent chromaticity of the stimulus. We refer to the relative contribution of the cone-targeted stimulus as *alpha* (where the relative contribution of the background is 1-*alpha*).

With knowledge of *alpha*, stimuli can be represented in more conventional units, i.e., the L/(L+M) and S/(L+M) units of MacLeod-Boynton (1979),

$$L/(L+M)_{total} = alpha \times L_{fraction} + (1-alpha) \times L/(L+M)_{background},$$
$$S/(L+M)_{total} = alpha \times S_{fraction} + (1-alpha) \times S/(L+M)_{background},$$

(Equations 3.3-4)

where the $S_{fraction}$ for 543 nm cone-targeted stimuli is zero.

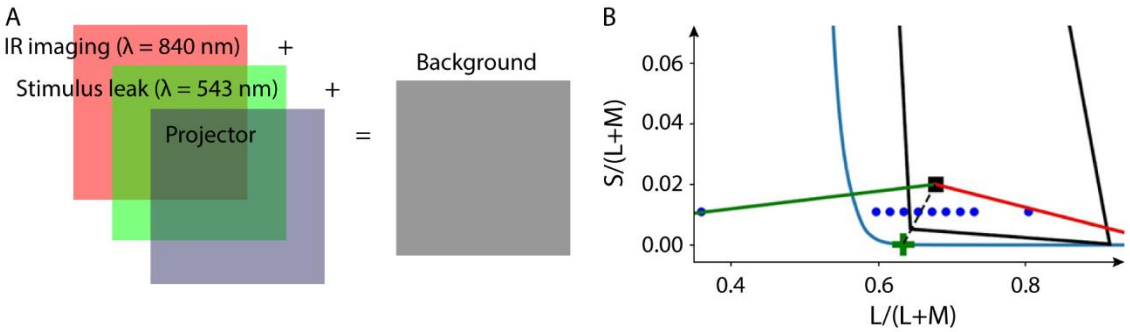

Figure 3.7. Specification of cone-targeted chromatic stimuli in MacLeod-Boynton units. (A) The background used for color matching and discrimination was composed of the IR imaging light (λ = 840 nm), leak from the stimulus channel (λ = 543 nm), and light from the projector. (B) To specify cone-targeted chromatic stimuli in MacLeod-Boynton units, the relative contribution of the background must be considered. The chromaticities that can be achieved by mixing of the background and the 543 nm light is shown by the dashed line adjoining the estimated background chromaticity (black square) and 543 nm position (green cross) on the spectrum locus (teal line). The relative contribution of the AOSLO cone-targeted light (*alpha*) to the stimulus is determined by where the matched chromaticities fall in relation to this line. The blue markers show the estimated positions of cone-targeted stimuli used in the color matching task (*alpha* = 0.45). Solid red and green lines correspond to directions of L- and M-cone isolating stimuli from the background point. Solid black lines represent the gamut of chromaticities achievable by the projector.

Figure 3.8 shows results for the color matching task. In the left panel (A), the individual match points from an example session are shown (black crosses). The blue circles show the estimated positions of the stimuli ($L/(L+M)_{total}$ and $S/(L+M)_{total}$ from Equations 3.3-4). The red circles indicate the average color matches, with error bars in both dimensions.

In general, the color matches made by the observer deviated along the L/(L+M) axis, as expected. Additionally, some points reflecting color matches made by the subject fall out of the projector gamut. The positions of these points were calculated by the subtracting the amount of the red primary from the projector that had been added to the cone-targeted stimulus to achieve a match (see 3.4.2 Stimulus & Procedure).

There was a large compression between the matched values and the estimated $L/(L+M)_{total}$ values from Equations 3.3-4. This can be seen more clearly in Figure 3.8B, where the values calculated from Equations 3.3-4 (*alpha* = 0.45, determined from the color matching results) are plotted against the matched L/(L+M) (top panel) and S/(L+M) (bottom panel) values for all sessions (excluding the out-of gamut-values). For S/(L+M), there is some variability in matched points, but the center of the distribution is near the S/(L+M) value expected with *alpha* = 0.45. For L/(L+M), the relationship appears linear (slope = 0.3311, p = 0.0001), however, the fitted line from a simple regression deviates substantially from unity (blue line), indicating that the calculated values are compressed relative to values attained by color matching in a calibrated projector space. Note that for the most extreme $L/(L+M)_{total}$ calculated (0.3637), the out-of-gamut match estimate

deviated substantially from linearity (L/(L+M) = 0.6235, S/(L+M) = 0.0114), and thus was excluded from the regression.

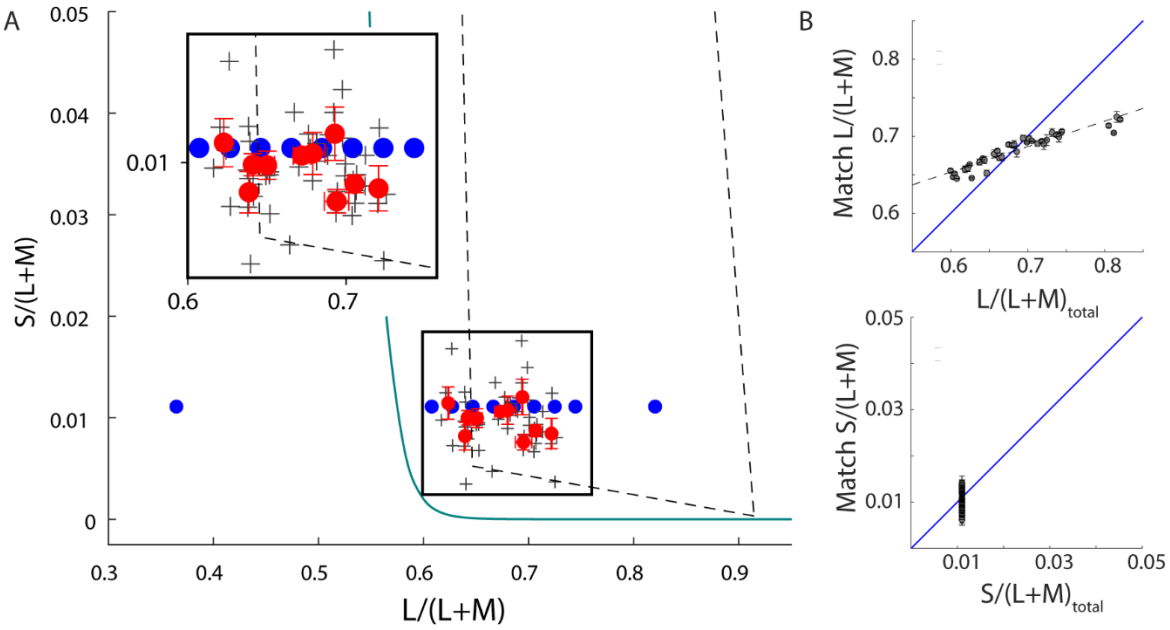

Figure 3.8. Color matching results. (A) Results from an example session. Each individual match is shown (gray crosses), with the red circles showing the average match point for each targeted chromaticity (error bars are SEM). The blue circles show the estimated positions of the stimuli based on Equations 3.3-4. The black dashed lines represent the gamut limits of the projector, and the teal line is the spectrum locus. Points outside of the projector gamut were calculated by subtracting the amount of red light added to the cone-targeted stimulus to bring it back within gamut. Although some matches are outside of the projector gamut, there is a compression of the matched points relative to the calculated chromaticities along the L/(L+M) axis. This can be seen more clearly in panel B, where the estimated $L/(L+M)_{total}$ and $S/(L+M)_{total}$ values from Equations 3.3-4 are plotted against the matched values. These data include all four experimental sessions, with the average match point for each tested chromaticity shown (error bars are SEM).

Results for the discrimination task can be seen in Figure 3.9A. The average thresholds for both increment and decrement staircases are shown. These were not found to differ significantly, so data from the two conditions were combined. Along the x-axis, L/(L+M) indicates the $L/(L+M)_{total}$ values scaled by the observed compression from the color matching results. For reference, the corresponding $L_{fraction}$ is noted below. Thresholds (ΔL/(L+M)) are scaled similarly. Example staircases are shown in Figure 3.9B. For the lowest $L_{fraction}$, decrement (-L/(L+M)) staircases could not be reliably measured (due to gamut constraints), thus this point represents the average of the two increment staircases. Overall, the results for the chromatic stimuli reveal a familiar V-shaped function characteristic of pedestal-versus-threshold functions with more conventional stimuli (e.g., Krauskopf & Gegenfurtner, 1992), with the minimum of the V here falling near L/(L+M) = 0.65. We return to this point in the discussion.

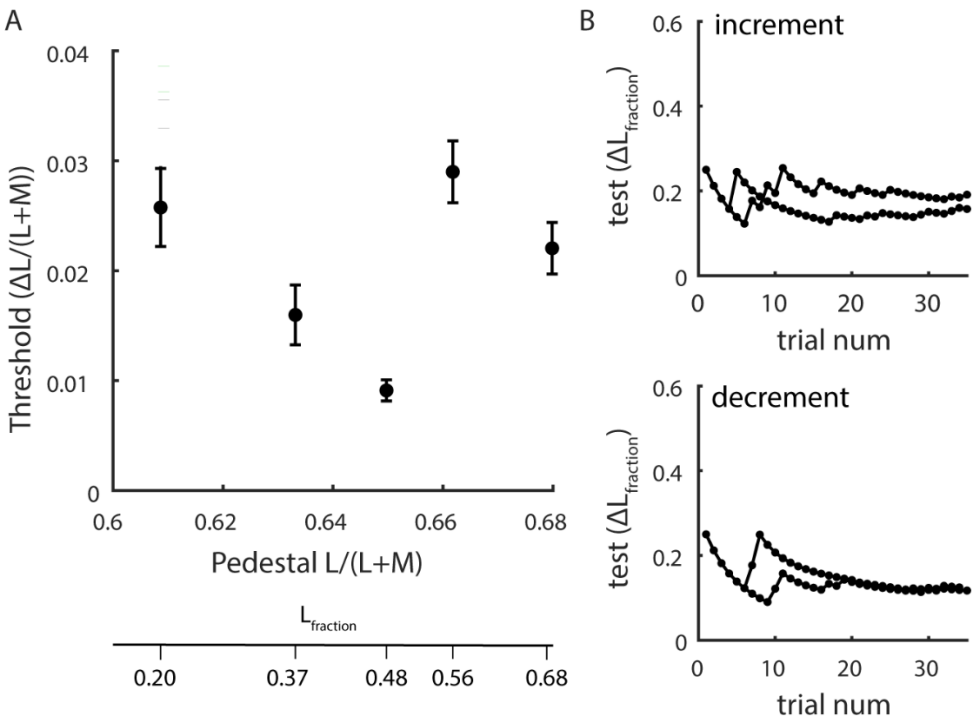

Figure 3.9. Discrimination results. (A) Thresholds for the different pedestal stimuli, converted to MacLeod-Boynton (1979) units by applying Equations 3.3-4 and applying the compression observed from the color matching results (Figure 3.8). The $L_{fractions}$ corresponding to the pedestal stimuli are noted below the graph for convenience. (B) Example staircases from the $L_{fraction}$ = 0.68 condition (L/(L+M) = 0.68 after compression, due to the point of intersection between the fit and unity line in Figure 3.8B, top panel).

We performed a paired t-test to evaluate whether the differences between the discrimination thresholds for scrambled stimuli (where the stimulus array was mismatched with the spectral identity of the cones) were significantly higher than their chromatic counterparts for the two pedestals where both conditions were tested ($L_{fraction}$ = 0.2022, 0.3667). Though the average scrambled thresholds were higher than the chromatic thresholds, this difference was not found to be significant (p = 0.0742), likely due to our small sample size (n = 6). It should be noted that in both cases, thresholds for scrambled stimuli were measured after chromatic thresholds, therefore we cannot rule out that subject fatigue may have influenced our results.

3.4.4 Discussion

In the current experiment, we targeted L- and M-cone photoreceptors of known spectral sensitivity (Sabesan et al., 2015) with cone-sized stimuli that were scaled in intensity depending on the targeted cone type (Figure 3.5). The subject performed color matching and discrimination tasks with these types of chromatic stimuli (Figure 3.6), which appeared as a uniform chromatic patch that varied in chromaticity along the L/(L+M) axis of MacLeod-Boynton (1979) chromaticity diagram (Figure 3.7). When cone-targeted intensities were scrambled in a manner inconsistent with the underlying

cone mosaic, as was done in the discrimination task, the percept was no longer of uniform chromaticity, but was described by the subject to be a muddled pattern of intensity variations, without a clear chromatic component.

The representation of chromaticity with AOSLO cone-targeted stimuli is of practical importance. Several authors have recently used this as a tool to investigate the mechanisms underlying color vision (e.g., Hofer et al., 2005b; Sabesan et al., 2016; Schmidt et al., 2018a and 2018b). Currently, the AOSLO system is limited to only two visible wavelengths for stimulation. Even if this range were expanded by addition of a third primary, technical difficulties arising from chromatic aberration would abound. The specification of chromatic stimuli with light of a single wavelength in conventional units is paramount to generation of chromatic stimuli when more than a few cones are in play, and will allow for the mechanisms underlying color perception to be isolated in behavioral experiments.

The discrimination task here was a replication of classical chromatic discrimination experiments performed with more conventional stimuli (e.g., Krauskopf & Gegenfurtner, 1992). Our results revealed the V-shaped function familiar of previous work. However, the minimum was displaced from the background chromaticity originally specified. The total background chromaticity depends not only on the light from the projector, but the IR imaging light (840 nm) and leak through the 543 nm stimulus channel due to first-order scatter from the AOM (Domdei et al., 2018). After color matching of the total background, the chromaticity was determined to be L/(L+M) = 0.6511 and S/(L+M) = 0.0165. This falls closely in line with the pedestal L/(L+M) value calculated after compression at the minimum of the V-function, 0.6497, reflecting the highest sensitivity for discriminations near the adapting chromaticity.

Additionally, we found that thresholds for scrambled stimuli (inconsistent with the spectral typing of cones in the identified patch) were higher at the two pedestals tested. As noted in the results, these measurements were made after the chromatic discrimination thresholds at the same pedestals. While we do not believe that subject fatigue influenced these results substantially, it remains to be seen whether chromatic discrimination thresholds are consistently lower across the range of achievable pedestals. In the present experiment, this was introduced mainly as a control to demonstrate that discriminations were made by a chromatic mechanism specifically, even though a single wavelength was used to generate the stimuli. In future experiments, when stimuli nearer to the human gamut limits are employed, it will be important to demonstrate whether discrimination is made solely on the basis of chromatic contrast to judge whether these percepts are reflective of near-gamut-limit experiences.

In general, our results are consistent with the idea that chromaticities varying along the red/green axis of color space can be reproduced with cone-targeted stimuli using light of only a single wavelength. In our study, 543 nm was selected due to the near-identical sensitivities of the L- and M-cone photoreceptors at this wavelength. We estimated the L/(L+M) and S/(L+M) values of the cone-targeted stimuli following Equations 3.3-4, and found that there was a linear relationship between the estimated

values and the matched chromaticities. However, there was a significant compression in the matched chromaticities relative to the calculated values. We consider potential reasons for this below.

One potential cause of this compression could be due to blur in the cone-targeted stimuli. We modeled the effect that typical blur might have based on previous AOSLO light delivery models (Harmening et al., 2014), but we found that even at unreasonably large levels of defocus the model did not account for as much compression as we observed in the color matching results. The stimuli used here are unlike the AOSLO cone-targeted stimuli of past experiments in that hundreds of cones are targeted simultaneously. Errors in registration between the experiment selection image and the master image containing cone identities may have introduced additional error if some cones were misaligned.

Additionally, the larger size of the patch stimulus may have caused larger errors in stimulus delivery that would not be typical of single-cone or cone-pair stimulation. For stabilized stimuli in the AOSLO, the prediction made for the timing of stimulus delivery in the raster scan is made when the scan reaches the strip preceding the stimulus location; thus, any eye motion that occurs during the time of prediction and delivery results in stabilization error. For the larger stimuli used here, this would likely result in additional errors in stimulus delivery that cannot be quantified by simply tracking a single point near the stimulus center.

It is also possible that this compression may be due to neural factors, for example, lateral mechanisms in the retina (e.g., gap junctions) which may introduce crosstalk between adjacent receptors, thereby reducing the opponent signal (Tsukamoto et al., 1992; Hornstein et al., 2004). Hornstein et al. (2004) modeled the effect of electrical coupling between L- and M-cones and determined that sensitivity for wavelength discrimination may be reduced by as much as 20% for wavelengths greater than 530 nm. While this may contribute some to the observed compression, it is unlikely to account for all of it.

Finally, it is possible that the differences between the L/(L+M) values of the matches and those calculated from Equations 3.3-4 may be due to differences in the stimuli themselves. The cone-targeted stimulus was stabilized to the retina and appeared for four frames at each presentation, while the matching field moved freely on the retina in a manner consistent with the eye's natural motion and was on continuously during the matching procedure. Although not ideal, these differences were necessary due to the constraints imposed by the current system setup. Light and contrast adaptation are both likely to affect the appearance of the matched stimulus when viewed continuously so as to reduce its apparent saturation relative to the 120 ms cone-targeted stimulus (Webster & Mollon, 1994; Webster & Mollon; 1995; Webster & Wilson, 2000). However, this would alter the subject's match points in the direction opposite of the observed compression.

The potential role that eye-motion (or lack thereof) might play in color appearance is less well-defined. While it is well known that prolonged viewing of a chromatic target will result in Troxler fading, how fixational eye motion might play a

supportive role in color vision has not been previously explored. The movement of a stimulus across many photoreceptors and receptive fields of downstream neurons may aid the visual system in distinguishing between chromatic and achromatic contrast by removing potential ambiguity in the retinal representation of the stimulus, perhaps even rectifying the effect of neural crosstalk between cones at their junctions to restore spectral opponency at a later neural site.

In any case, our results are an encouraging first step toward the representation of cone-targeted stimuli in physiologically relevant color space, widening the potential for future experiments investigating the neural mechanisms underpinning color vision. Our discrimination results represent a replication of the classical chromatic discrimination experiments with cone-targeted stimuli. If a full human-gamut range of chromaticities can be attained with cone-targeted stimuli, it may be possible to investigate the chromatic mechanisms at saturating values not normally experienced in natural viewing conditions. While unrepresentative of normal color vision, this may lend insight into how the visual system renormalizes color signals to suit the range of chromaticities encountered in the environment (von der Twer & MacLeod, 2001; MacLeod, 2003; Webster, 2011), for example, to maintain stability of chromatic percepts across the lifespan (Werner & Schefrin, 1993; Delahunt et al., 2004) or to enhance color appearance in anomalous observers (Regan & Mollon, 1997; Boehm et al., 2014).

3.5 Conclusions & Future Directions

The experiments presented in this chapter represent the first steps towards reconstruction of color space using cone-targeted stimuli in an AOSLO. For 543 nm light, where L- and M-cone photoreceptors are nearly equally sensitive, the appearance of small spot-stimuli (single cones or cone pairs, i.e., Experiment 1) is consistent with cone type such that stimulation of two L-cones together appears reddish against an achromatic background, and two M-cones appears greenish. When L- and M-cones are targeted together with the same intensity, the percept is desaturated, corresponding to a larger change in luminance than chromaticity relative to the background. This is consistent with the interpretation that post-receptoral mechanisms compare activity in L- and M-cones in representations of luminance (L+M) and chromaticity (L-M) at a low level of the visual system.

Further, by targeting large patches of cones with intensities biased towards either L- or M-cones, while keeping the total L+M content of the stimulus constant, we were able to construct spatial metamers for stimuli varying along the L/(L+M) axis of the MacLeod-Boynton (1979) chromaticity diagram.

Future work will be aimed at a better understanding of the compression observed in the color matching work. Expanding the gamut to include all potential chromaticities achievable with cone-targeted stimuli will enable novel questions about the mechanisms underlying color vision to be answered. For example, what functional limitations to spectral opponency might be imposed by the low-level mechanisms (e.g., gap junctions)? What role might fixational eye-motion play in generation of color

appearance? And, finally, can colors be seen and discriminated at the limits of the human gamut?

3.6 Acknowledgments

This chapter includes the collaborative effort of several individuals. The work presented in Experiment 1 is currently under review for publication, with approval of its inclusion here given from co-authors Brian P. Schmidt (corresponding author), William S. Tuten, and Austin Roorda. Experiment 2 was a collaborative effort between the aforementioned authors, in addition to Dr. Ren Ng, Utkarsh Singhal and Peter Manohar. Dr. Brian P. Schmidt is credited with much of the theory and calculation behind the colormetric representation of AOSLO cone-targeted stimuli. Appreciation is given to these collaborators for their contributions and permission to include the work here.

Chapter 4: Transverse Chromatic Offsets with Pupil Displacements in the Human Eye: Sources of Variability and Methods for Real-Time Correction

4.1 Abstract

Tracking SLO systems equipped to perform retinally targeted stimulus delivery typically use near-IR wavelengths for retinal imaging and eye tracking and visible wavelengths for stimulation. The lateral offsets between wavelengths caused by transverse chromatic aberration (TCA) must be carefully corrected in order to deliver targeted stimuli to the correct location on the retina. However, both the magnitude and direction of the TCA offset is dependent on the position of the eye's pupil relative to the incoming beam, and thus can change dynamically within an experimental session without proper control of the pupil position. The goals of this study were twofold: 1) To assess sources of variability in TCA alignments as a function of pupil displacements in an SLO and 2) To demonstrate a novel method for real-time correction of chromatic offsets. To summarize, we found substantial between- and within-subject variability in TCA in the presence of monochromatic aberrations. When adaptive optics was used to fully correct for monochromatic aberrations, variability both within and between observers was minimized. In a second experiment, we demonstrate that pupil tracking can be used to update stimulus delivery in the SLO in real time to correct for variability in chromatic offsets with pupil displacements.

4.2 Introduction

In the last decade, scanning laser ophthalmoscopes (Webb et al., 1980), or SLOs, both with (Roorda et al., 2002) and without (Sheehy et al., 2012) adaptive optics (Liang et al., 1997) have been used to simultaneously image the retina, track eye motion (Vogel et al., 2006), and deliver targeted, stabilized stimuli to the retina (Arathorn et al., 2007; Yang et al., 2010). These systems have several advantages for both clinical research and psychophysics. For example, adaptive optics scanning laser ophthalmoscope (AOSLO) based microperimetry (Tuten et al., 2012) has been used to assess visual function in local areas of interest in diseased retinas (Wang et al., 2015). Additionally, the capability for cone-targeted stimulus delivery with adaptive optics (AO) has made it possible to perform psychophysical experiments at the level of single cone photoreceptors (Harmening et al., 2014; see also: Sabesan et al., 2016; Schmidt et al., 2018a and 2018b).

In multi-wavelength tracking SLOs, near-infrared wavelengths are typically used for retinal imaging and eye tracking, and visible wavelengths in the 500-700 nm range are used for retinal stimulation. Because the infrared images are used to identify the targeted retinal locations for functional testing, chromatic aberration between the imaging and stimulus wavelengths must be carefully measured and corrected to

achieve cellular resolution. Chromatic aberration has two components, longitudinal chromatic aberration (LCA) and transverse chromatic aberration (TCA).

LCA is the difference in axial focus between wavelengths. The magnitude of LCA in human eyes has been carefully quantified (Wald & Griffin, 1947; Bedford & Wyszecki, 1957; Charman & Jennings, 1976; Marcos et al., 1999; Fernández et al. 2006; Vinas et al., 2015) with estimates of approximately 2 diopters (D) across the visible spectrum, with little variability between individuals.

TCA is the angular offset between the chief rays of two or more wavelengths which causes a lateral offset in the retinal image plane. TCA is typically measured subjectively with a two-wavelength Vernier alignment task (Ogboso & Bedell, 1987; Simonet & Campbell, 1990; Thibos et al., 1990 and 1992) or objectively with image-based methods in an adaptive optics SLO (Harmening et al., 2012; Privitera et al., 2016; Winter et al., 2016). TCA is highly variable between individuals (Simonet & Campbell, 1990; Rynders et al., 1995; Marcos et al., 1999 and 2001), owing to differences in the position of the achromatic axis in the eye, pupil centration, and alignments of the various optical components of the eye.

Because LCA varies little between individuals (Atchison & Smith, 2005), a fixed correction between the relative source vergences is sufficient for multi-wavelength imaging and stimulation (Grieve et al., 2006; Harmening et al., 2012). TCA, however, is a much more challenging problem to account for. While TCA can be measured quickly and reliably with image-based methods in an AOSLO (Harmening et al., 2012), it depends on the exact position of the pupil relative to the incoming beam (Thibos et al., 1990) and thus changes dynamically with small shifts in pupil position.

Previous experiments with retinally stabilized stimuli in the AOSLO have accounted for changes in TCA by measuring TCA image offsets at the beginning and end of an experimental session and discarding data from sessions where TCA changed more than a predetermined threshold. However, this ignores any dynamic changes in TCA that occur during an experimental session that could, in some cases, displace a stimulus from its targeted retinal location by as much as 1 arcmin (Privitera et al., 2016). Maintaining pupil alignment is especially difficult with unpracticed subjects or when a bite bar is not used, as is often the case with clinical populations and naïve participants. Therefore, a new strategy is needed for measuring and correcting for TCA offsets in real time in order to increase the efficiency of behavioral data collection in an SLO and reduce inter-trial variability in stimulus delivery.

For a perfectly centered optical system, TCA is zero along the optical axis. But in the human eye, TCA will often be present along the line of sight because there is no true optical axis of the human eye and, even if there were, the fovea is displaced relative to it. Consequently, when the subject views a stimulus composed of two wavelengths foveally through a centered pupil, there will be an offset between the two images formed on the retina that is caused by TCA. Displacements from a centered pupil cause the magnitude of the chromatic offset to change, following a linear relationship at small pupil offsets (< 2mm) (Simonet & Campbell, 1990; Thibos et al., 1990 and 1992; Privitera et al., 2016):

$$TCA_{(x,\,y)} = m_{(x,\,y)} \times (R_{(x,\,y)} - P_{(x,\,y)}) + TCA_{(0,\,0)}, \qquad \text{(Equation 4.1)}$$

where $TCA_{(x,\,y)}$ is the horizontal (x) and vertical (y) TCA offset in retinal image space in arcminutes, $R_{(x,\,y)}$ is the (arbitrary) reference pupil position, and $P_{(x,\,y)}$ is the real-time pupil position. The pupil offset, $R_{(x,\,y)} - P_{(x,\,y)}$, is specified in millimeters. $TCA_{(0,\,0)}$ is the TCA offset at the reference pupil position, and is the y-intercept of the linear function relating TCA to pupil offset. Finally, $m_{(x,\,y)}$ is the slope, or the change in TCA offset per unit pupil displacement.

Moving $TCA_{(0,\,0)}$ to the left-hand side of Equation 4.1 yields Equation 4.2, where ΔTCA is the change in TCA offset relative to its value at the reference position.

$$\Delta TCA_{(x,\,y)} = m_{(x,\,y)} \times (R_{(x,\,y)} - P_{(x,\,y)}), \qquad \text{(Equation 4.2)}$$

The linear relationship described above implies that changes in TCA with pupil displacement can be easily predicted, and thus compensated for, with only knowledge of the current pupil position relative to some reference and the ΔTCA/mm ratio, or $m_{(x,\,y)}$ in Equations 4.1 and 4.2.

Previous examinations of the relationship between TCA offsets and pupil displacements have measured TCA subjectively through a displaced pinhole aperture (Simonet & Campbell, 1990; Thibos et al., 1990 and 1992), what previous authors have referred to as optical TCA. For example, Thibos et al. (1990) measured TCA as a function of pupil offset for Vernier targets composed of 433 and 622 nm wavelengths and found a mean slope of 4.38 arcmin/mm. In general, their results were well predicted by a chromatic eye model in which the TCA offset is directly related to the location of the chief ray with respect to the pupil center.

More recently, in two previous publications from our lab (Harmening et al., 2012; Privitera et al., 2016) data were presented demonstrating the linear relationship between TCA offset and pupil position in an AOSLO with image-based methods after correcting for higher- and lower-order aberrations. Across these studies, data for two individuals were reported. The primary goal of the current study was to demonstrate a novel method for real-time correction of TCA offsets with pupil displacements. However, for TCA compensation in a tracking SLO, it is important to know to what extent variability in $m_{(x,\,y)}$ should be expected. If there is little variability between individuals, the need to calculate slopes for individual subjects will be removed. This would be especially valuable in situations where time with subjects is limited, particularly in studies utilizing clinical populations. Additionally, it is often impractical to measure TCA with image-based cross-correlation methods, due to the uncomfortable brightness of the imaging light that is experienced with visible wavelengths and the overall reduction in image quality that is often seen in patient populations.

Previous studies investigating the relationship between pupil displacements and changes in TCA did not directly assess variability between individuals, or within an

individual along different pupil meridians. One study (Marcos et al., 2001) reported a correlation between foveal TCA and the magnitude of monochromatic aberrations, though they did not measure TCA with pupil displacements. It remains unknown how monochromatic aberrations might affect TCA, but this is of practical importance in tracking SLO systems without adaptive optics, where estimates of TCA are limited to subjective alignment procedures in the presence of monochromatic aberrations.

The current study comprised two experiments. Two systems were used, an adaptive optics scanning laser ophthalmoscope (AOSLO) and a tracking scanning laser ophthalmoscope (TSLO), both systems are described in more detail in Chapter 1.2. Because the methods for the two experiments are different, each experiment will be described and discussed separately.

In Experiment 1, we measured TCA as a function of vertical and horizontal pupil position in normal eyes in an AOSLO both objectively with image-based methods and subjectively with a Vernier-like alignment technique. Subjective TCA was measured with and without correction for monochromatic aberrations to investigate the sources of variability affecting TCA across the pupil.

In Experiment 2, we implemented and tested a strategy to compensate for dynamic changes in TCA in real time during a psychophysics experiment in a TSLO without correction for monochromatic aberrations.

To summarize, we found that, in the presence of aberration, there are significant differences in the slope of TCA with pupil offsets between meridians in the eye and between individuals. After correcting aberrations, the measurements are much less variable. Finally, by performing a calibration of the slope of TCA with pupil offsets, we can use pupil tracking to guide compensation of TCA offsets in real time.

4.3 Experiment 1: Sources of Variability in TCA with Pupil Displacements

4.3.1 Apparatus

A multi-wavelength adaptive optics scanning laser ophthalmoscope (AOSLO) was used for imaging and stimulus delivery. This system is described in detail elsewhere (Roorda et al., 2002; Harmening et al., 2014), with relevant details specified below.

Three wavelengths (λ = 940, 840, 543 nm) were selected from a supercontinuum light source (SuperK EXTREME, NKT Photonics, Birkerod, Denmark) and the vergence of each wavelength channel was adjusted to compensate for LCA of the human eye using the following procedure: Using 680 nm as a reference wavelength, we computed the expected difference in the eye's refractive state for the specified wavelength using published LCA models (Atchison & Smith, 2005). Then we placed a model eye in the system and positioned the retina to simulate an equal and opposite refractive state. Next, we adjusted the vergence of the source at its point of entry in the light delivery arm of the system to focus the scanning beam on the retina of the model eye. Finally, we adjusted the position of the confocal pinhole to optimize the image. 940 nm light was used for wavefront sensing. 840 nm (near-IR) and 543 nm (green) light were used for

both imaging and stimulation. Beam size at the pupil was approximately 3 mm in the subjective alignment task, and 6.5 mm for retinal imaging.

All three channels were raster scanned onto the retina and subtended a square field 0.95 x 0.95 deg in size (corresponding to a sampling resolution of 0.11 arcmin per pixel). Light backscattered from the 840 and 543 nm channels was collected into a photomultiplier tube (Photosensor module H7422, Hamamatsu Photonics, Hamamatsu, Japan) via a confocal pinhole and digitized. The intensity of the 840 and 543 nm channels were modulated with fiber-coupled acousto-optic modulators (AOMs; Brimrose Corp, Sparks Glencoe, MD). The subject's head was positioned with a bite bar mounted on an X, Y, Z translation stage.

The AOSLO employed a closed-loop AO system comprised of a custom-built Shack-Hartmann wavefront sensor and a deformable mirror (DM97, ALPAO, Montbonnot-Saint-Martin, France). The system operated in one of three modes, described in further detail in *2.4 Procedure*.

Pupil videos were recorded using a ½ inch USB CMOS color board camera (DFM 61BUC02-ML, ImagingSource Inc., Charlotte, NC) at 1024 x 768 pixel resolution corresponding to approximately 60 pixels per mm. The sensor was controlled by a MATLAB plugin which allows full control and optimization of the camera's settings (e.g., exposure, gain, gamma) from the MATLAB working space. Images of the pupil were formed via retro-illumination from the 840 nm imaging beam (i.e., red-eye reflex). Videos were acquired directly in MATLAB at approximately 10 fps and then converted into gray scale. The shape of the pupil was first roughly separated by applying a simple gray scale threshold, and then its contour was finely defined by a gradient (edge detection) operator. Next, an ellipse was fitted using a least-squares criterion. Pupil tracking was represented by the x and y coordinates of the center of the fitted ellipse.

The pupil camera was coaligned with the AOSLO beam path by means of a beamsplitter placed before the eye with a 45° angle of incidence and broad-spectrum anti-reflective coating on one side to minimize reflections (Ross Optical Industries, El Paso, Texas). The pupil camera was placed at the back end of a Maxwellian assembly which is typically used to form background images and fixation targets, though the projector was not used in the current study. A 50 mm square hot mirror (#43-452, Edmund Optics, Barrington, NJ) was placed before the projector to reflect light to the pupil camera while allowing transmittance of visible wavelengths from the projector. The optical axes of the pupil camera and SLO beam path were carefully aligned to ensure that axial misalignments of the subject's pupil were not misconstrued as lateral displacements.

4.3.2 Stimulus

The stimulus was similar to that previously used by our group for subjective measurements of TCA (Harmening et al., 2012). The background was a square raster pattern subtending 0.954 deg and was composed of the 840 nm light source that is typically used for imaging, in addition to leak from the 543 nm light source due to first-

order light scatter through the AOM (Domdei et al., 2018). The total retinal illuminance of the background was 1.71 log Trolands (logTd). The stimulus consisted of four decrement squares (-0.56 logTd), 4.42 arcminutes in length, arranged in a square pattern, and a green target square (λ = 543 nm, 2.04 logTd) of the same size that was spatially offset by a random amount between 0 and 2.21 arcminutes (vertically and horizontally) of the objective center of the stimulus configuration at the beginning of each trial (Figure 4.1A). The decrements were achieved by switching off the 840 nm wavelength at the appropriate points in the raster scan.

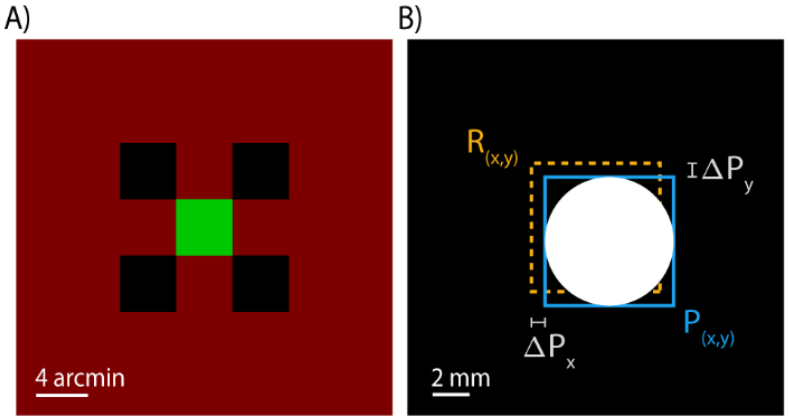

Figure 4.1. TCA induced by pupil displacements. (A) The stimulus used for the alignment task. Subjects aligned a green (λ = 543 nm) target square to be centered with respect to the surrounding decrement (λ = 840 nm) squares. (B) Pupil tracking was performed in real time throughout the experiment. The experimenter induced pupil offsets relative to the reference pupil position, $R_{(x,y)}$.

4.3.3 Procedure

Two subjects (20075 and 20076, ages 29 and 30) participated in all parts of Experiment 1. Both were authors of the study. Three additional subjects (20036, 20109 and 20112) participated in the imaging portion of the experiment. All procedures were approved by the University of California, Berkeley Committee for Protection of Human Subjects and adhered to the tenets of the Declaration of Helsinki. All subjects signed informed consent documents before participating in the experiments.

Subjects' pupils were dilated and cyclopleged with 1% tropicamide and 2.5% phenylephrine ophthalmic solutions 15 minutes prior to the experiment. The experimenter aligned the subject's pupil to be centered with respect to the imaging beam and this was set as the reference pupil position.

At the beginning of each trial, the experimenter moved the subject's pupil within +/- 0.5 mm of the reference pupil position in one of nine positions, upward-left, left, downward-left, downward, downward-right, right, upward right, upward, and centered (Figure 4.1B). The induced pupil offsets followed either a clockwise or counter-clockwise pattern which was alternated after the centered pupil position was reached at the end of each set of trials.

The subject adjusted the position of the green target square using a keyboard until it appeared to be centered with respect to the four decrement squares. Subjects indicated the alignment by pressing the enter key, and pupil positions were recorded at the time of the keypress. Subjects completed 45 alignments in each block of trials, where in each block one of the three modes of optical correction was applied ('defocus only,' 'defocus + astigmatism,' or 'all aberrations').

In the first mode ('defocus only'), defocus was manually added to the mirror, which was otherwise static for the duration of the session. The point of subjective best-focus was found by scanning the stimulus onto the retina and adjusting defocus until the subject reported seeing the sharpest image.

In the second mode ('defocus + astigmatism'), defocus and astigmatism were manually added to the mirror and the point of subjective best-focus was again found. Subjective corrections were -1.4 diopter sphere (DS), -1 diopter cylinder (DC), axis 179 deg for subject 20075 and 2.8 DS, -0.75 DC, axis 155 deg for subject 20076.

Objective wavefront measurements were not performed for these conditions, though the subjective correction of 20075 was close to that found on an independent Shack-Hartmann wavefront sensor (λ = 830 nm, -0.48 DS, -1.16 DC, axis 8.04 deg) in a previous experiment, after taking into account the chromatic difference of focus due to LCA (Atchison & Smith, 2005). We did not record objective wavefront data for subject 20076.

In the third mode ('all aberrations corrected'), real-time wavefront measurements were used to control the deformable mirror and correct both lower- and higher-order monochromatic aberrations. In this mode, correction continued in real time throughout the duration of the session.

Additionally, we measured TCA at similar pupil offsets with image-based methods following the methodology described in detail in Harmening et al. (2012). Briefly, AOSLO images were recorded with λ = 543 nm (4.5 μW) and λ = 843 nm (52 μW) light simultaneously by interleaving lines composed of light from the different channels. A cross-correlation procedure was used to calculate the image offset between the two wavelengths. The median image offset across 150 video frames (30 Hz frame rate) was used to estimate TCA. Note that the image-based methods were only possible following correction for all aberrations – the low signal and poor resolution precluded image-based alignments for the other modes.

4.3.4 Results

Results for the two subjects' alignments under the three optical correction conditions and objective measurements of foveal TCA are shown in Figure 4.2. In panels A-C and E-G of the figure, each point represents the subjective vertical or horizontal offset the subject required to align the 543 nm increment square to the 840 nm decrement squares, plotted as a function of pupil offset in the respective direction. In panels D and H, each point corresponds to the median TCA offset measured objectively by analysis of 5 second videos (30 Hz frame rate), and thus reflects the estimated TCA averaged

across 150 video frames. The data were fit to Equation 4.2, where the slopes ($m_{(x, y)}$) represent the change in TCA per unit pupil displacement.

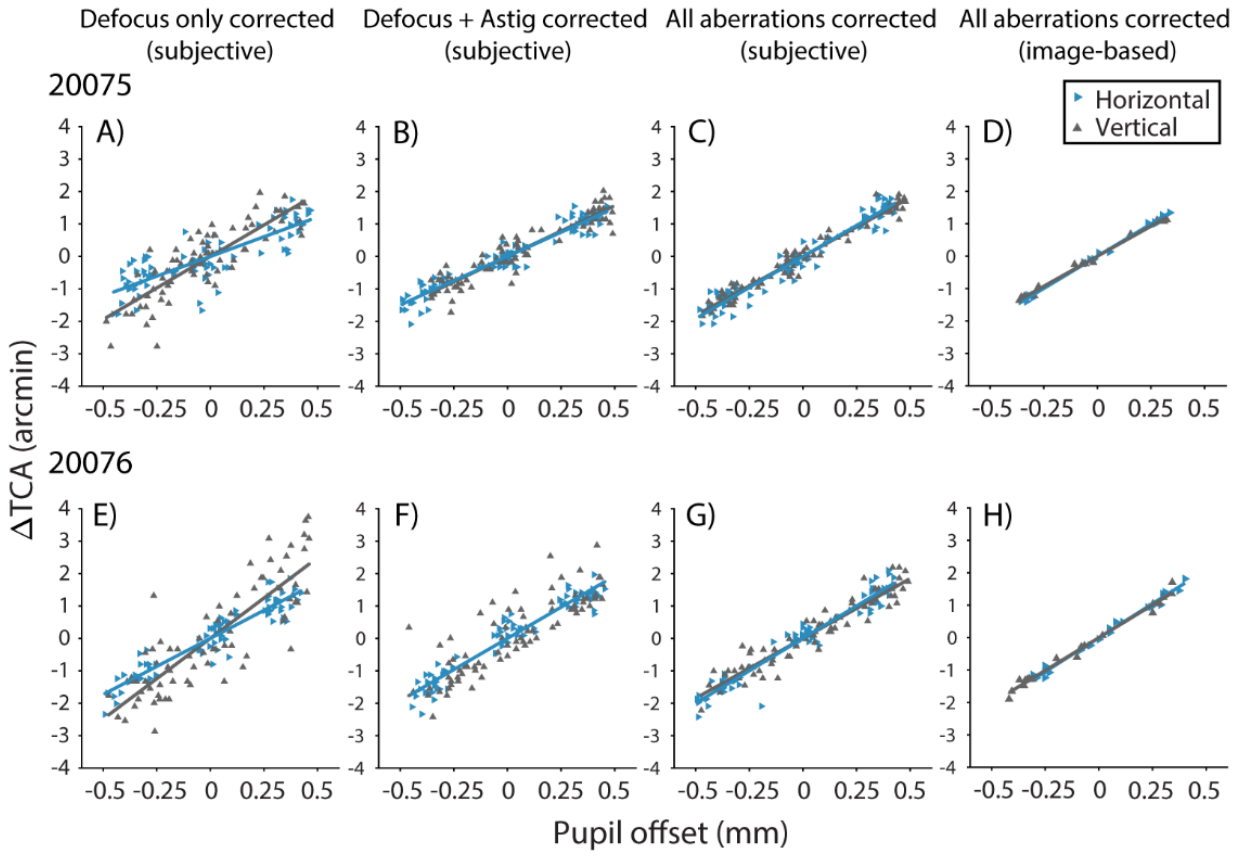

Figure 4.2. Changes in TCA (λ = 543 and 840 nm) with pupil displacement in the AOSLO for subjects 20075 (A-D) and 20076 (E-H). TCA was measured subjectively under different optical corrections: Defocus only (panels A and E), defocus and astigmatism (B and F), and all aberrations (C and G). Panels D and H show image-based TCA measurements following correction for all aberrations. The horizontal (blue rightward triangles) and vertical (gray upward triangles) components of the chromatic offset follow a linear relationship with the magnitude of the horizontal and vertical pupil offsets, respectively. Solid lines show fits to Eq. 4.2.

Bar charts showing the slope estimates and statistical comparisons are shown in Figure 4.3. Slopes of the regression lines were compared using the z-test method explained by Kleinbaum et al. (2013), with z-scores evaluated as the difference between regression slopes divided by the standard error of the differences between slopes.

In the defocus correction condition (Figure 4.2A and E), slopes relating the horizontal component of TCA to horizontal pupil offsets were significantly different from vertical changes in TCA with vertical pupil offsets ($p < 10^{-4}$; Figure 4.3). However, when we applied a correction for astigmatism (Figure 4.2B and F), the differences between horizontal and vertical slopes were no longer significant. This was also the case when all aberrations were corrected (Figure 4.2C and G); vertical and horizontal slopes were not significantly different for either subject (Figure 4.3).

Next, the amount of variability in TCA captured by the linear model was quantified with a correlation analysis (R^2). A perfectly linear system with zero noise would have $R^2 = 1$. In both subjects, R^2 increased as monochromatic aberrations were reduced. For 20075, R^2 increased from 0.7993 (average of horizontal and vertical R^2) when only defocus was corrected to 0.8195 when astigmatism was corrected as well. R^2 increased further to 0.9270 when AO correction was applied. For 20076, R^2 was 0.7020 for defocus only, 0.9069 for defocus + astigmatism, and 0.9524 with AO correction. Thus, as monochromatic blur was removed, variability in subjective TCA decreased.

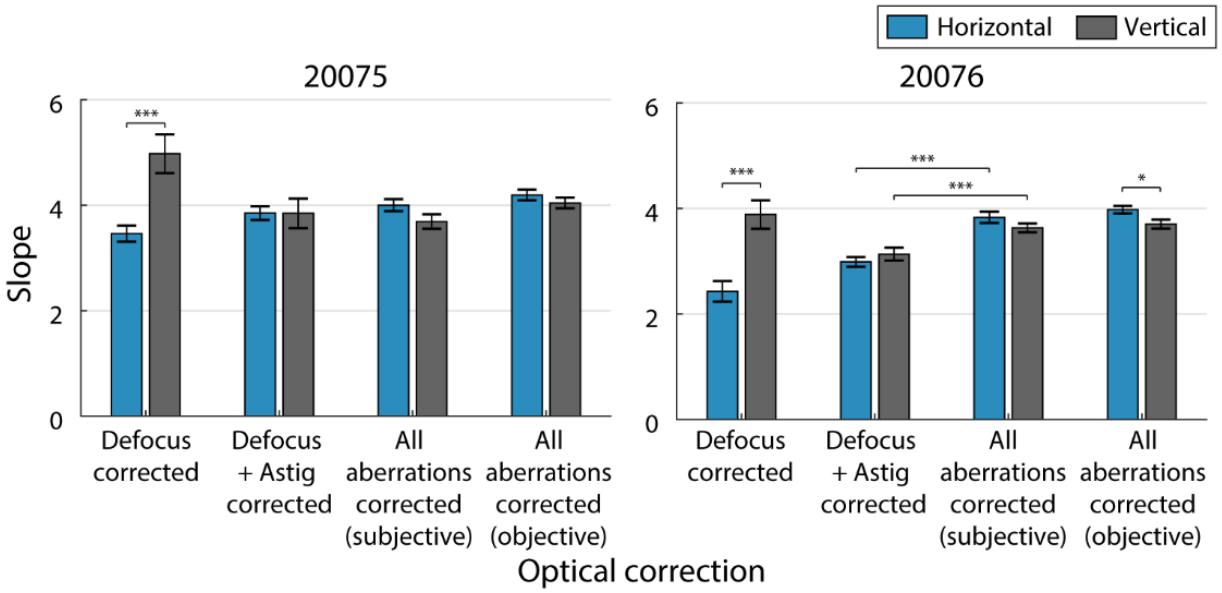

Figure 4.3. Comparison of slopes for changes in TCA with pupil displacements under different optical corrections. Slopes for horizontal (blue) and vertical (gray) changes in TCA are shown for subjects 20075 (left) and 20076 (right) under different optical corrections: defocus, defocus + astigmatism, and all aberrations. Slope estimates for changes in TCA with all aberrations corrected are reported for two measurement methods, subjective alignments and objective image-based. Error bars are standard errors of the slope estimates. Brackets show statistically significant comparisons (* $p < 0.05$, ** $p < 0.01$, *** $p < 0.001$).

Additionally, we compared the slopes between the 'defocus + astigmatism' and 'all aberrations' corrected conditions to see if there was any further change in slope after correction for higher-order aberrations. For 20075, slopes were not significantly different between the two conditions. However, both m_x and m_y were slightly steeper in the AO correction condition for 20076 ($p < 10^{-4}$). Comparing the horizontal and vertical slopes across the two subjects, we found that they were not significantly different after correction for all aberrations, with a mean m ratio of 3.845 for 20075 and 3.731 for 20076.

We also measured foveal TCA with pupil displacements using an image-based cross-correlation procedure (Figure 4.2D and H). To further investigate between-subject variability in slopes derived with the image-based protocol, three additional subjects

were included in this portion of the study. The slopes, $m_{(x, y)}$, and y-intercepts, $TCA_{(0, 0)}$, are reported below in Table 4.1. The sign convention is arbitrary and defined to yield positive slopes across both eyes. For pupil displacements, negative values for the horizontal component reflect displacements rightward in the pupil image relative to the reference (i.e., a temporal displacement for the subjects' left eyes, nasal for right eyes). For the vertical component, pupil displacements are positive in the superior direction and negative in the inferior direction.

Following this convention, TCA offsets tend toward positive values as the pupil is displaced in the positive direction, and vice versa. That is, for left eyes with positive pupil displacements, the green (λ = 543 nm) image becomes more displaced in the nasal/superior direction relative to the IR (λ = 840 nm) image on the retina. TCA offsets at the reference position ($TCA_{(0, 0)}$) were calculated to provide rough estimates of TCA at zero pupil offset, though it should be noted that this does not necessarily represent TCA for a centered pupil because the reference was defined as the location of best image quality rather than a direct estimate of the exact pupil center. Nonetheless, these values are consistent with previous measurements of TCA using the same wavelengths with a centered pupil in an AOSLO (Winter et al., 2016).

Table 4.1. Parameter estimates for fits to Eq. 4.1 for image-based TCA measurements (all aberrations corrected)

	$m_{(x, y)}$ *(arcmin/mm)*	$TCA_{(0, 0)}$ *(arcmin)*
20036	3.92, 3.74	1.89, 0.01
20075	4.19, 4.04	0.62, -0.36
20076	3.97, 3.71	-1.08, 0.61
20109	3.82, 3.83	1.32, -1.20
20112	3.65, 3.77	0.26, -0.87
mean	3.91, 3.82	0.60, -0.36

The small differences in slopes measured with image-based methods after AO correction could be due to differences in corneal curvature between subjects and/or between pupil meridians. We discuss this point further below. Figure 4.4 shows the data for all subjects with the combined data fit to Eq. 4.2. This was achieved by first fitting each subject's data to Eq. 4.1 to determine $TCA_{(0, 0)}$, the TCA at the pupil reference. TCA values were represented as a change from TCA at the reference position (ΔTCA). The slope of this function was 3.86 arcmin/mm and had $R^2 = 0.9768$.

Finally, we compared the slopes of the TCA versus pupil offset functions between the subjective alignment task to those acquired with the image-based method in the two subjects who participated in both portions of the study. For 20076, there was no significant difference between the slopes calculated with the two different methodologies. For 20075, there was a small difference in the vertical TCA with vertical pupil displacements, but this difference was not statistically significant at the α = 0.05 level after correction for multiple comparisons (Benjamini-Hochberg, 1995).

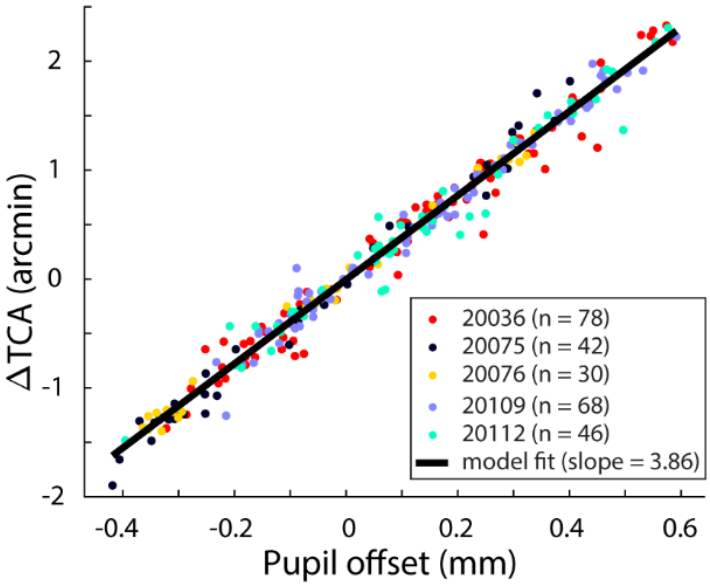

Figure 4.4. Image-based estimates of TCA at offsets relative to the pupil reference. Each data point represents the average TCA offset across 30 video frames plotted against the pupil offset relative to the reference position. Each subject's data (represented here by different colored circles) were individually fit to Eq. 4.1 and scaled so that ΔTCA, the change in TCA relative to its value at the reference, was zero at the reference pupil position (pupil offset = 0 mm). The combined data were then fit to Eq. 4.2 (black line).

4.3.5 Discussion

In Experiment 1, we compared slopes of two subjects' TCA versus pupil offset functions using a subjective alignment procedure to estimate TCA in an AOSLO under different optical corrections: defocus only, defocus + astigmatism, and all aberrations. In addition to measuring TCA with subjective alignment methods, we employed the image-based methods of Harmening et al. (2012) in the condition where all aberrations were corrected and high-resolution retinal images in the two wavelength channels could be obtained. The data of Harmening et al. (one subject) shows a horizontal slope of approximately 3.2 arcmin/mm, slightly lower than the mean slope of our sample, 3.86 arcmin/mm.

Our study used real-time pupil tracking, analogous to the measurements performed by Privitera et al. (2016), who used pupil tracking and image-based TCA to estimate the slope of the TCA versus pupil offset function to be 3.5 arcmin/mm in one subject. This is within the range of slopes recorded for our sample of five subjects using the image-based protocol (Table 4.1). In general, these results are consistent and support our conclusion that real-time correction for changes in TCA with a uniform slope estimate across subjects is a plausible and functional approach in an AOSLO where higher-order aberrations are corrected and inter-subjective variability is much reduced. Of course, a larger sample size and more information about the optical quality of subjects would be needed to develop a model which takes into account all interactions between monochromatic and chromatic aberrations.

With ‘defocus only’ correction, we observed significant within-subject variability in slope estimates with respect to pupil meridian derived from the subjective alignment task. In both subjects, differences between slopes with respect to pupil meridian were removed when subjects made alignments with defocus + astigmatism correction and all aberrations corrected.

We first explored whether the difference in slope could be caused by meridional differences in corneal curvature. But when we varied the radius of curvature in a simple chromatic eye model (Thibos et al., 1992), it did not produce differences between m_x and m_y as large as we observed in our data, suggesting that meridional differences in corneal curvature cannot fully account for this. Varying the radius of curvature to simulate asymmetries in normal eyes (Kiely et al., 1982), however, did produce differences in TCA consistent with the small differences observed when all aberrations were corrected, suggesting that small differences in slope (< 0.5 arcmin) present even after aberration correction may be due to differences in corneal curvature. Similarly, the between subject variability in slopes we observed with the image-based protocol and all aberrations corrected (Table 4.1) may be due to small between-subject differences in corneal curvature, though we did not measure this directly in our subjects.

We then considered how uncorrected monochromatic aberrations might affect TCA. One possibility is that changes in monochromatic aberrations with wavelength could add additional perceived offsets between polychromatic targets, since even monochromatic targets appear misaligned by an amount proportional to the aberration when viewed through split-field systems where one target is presented in normal view and the other through an isolated portion of the pupil (Campbell et al., 1990). However, Marcos et al. (1999) found variations in monochromatic aberrations with wavelength to be very small, and therefore they are unlikely to result in the relatively large differences in slope that we observed in our subjects.

Marcos et al. (2001) investigated variability in foveal TCA, and concluded that the individual differences in foveal TCA could not be fully explained by the displacement of the achromatic axis from the optical axis of the eye, pupil centration, corneal curvature or asphericity, or alignment of the various optical components of the eye. Instead, they noted a correlation between the magnitude of monochromatic aberrations (root mean square, or RMS) and foveal TCA which they attributed to irregularities in the shape of the cornea and lens. However, given that changes in corneal curvature have small effects on the magnitude of TCA, it is not clear how monochromatic aberrations could generate the differences they observed.

Another possibility is that the differences in actual TCA are very small in the eyes we tested, and the observed differences reflect an observer bias in perceived offsets between the targets that is due to overall blur of the stimulus (Mather & Morgan, 1986; Morgan et al., 1990; Whitaker et al., 1996; Akutsu et al., 1999). Moreover, as blur is expected to change with increasing offset from a central pupil position, these biases will not only give rise to variability in alignments but differences in slope as well. Figure 4.5 offers a visual to help explain this effect. An aligned stimulus was convolved with the computed point spread, shown in panel B, of a typical eye over a 3 mm pupil that was

displaced laterally in the horizontal and vertical directions (Figure 4.5A). As can be seen, the blur from the PSF makes the correct alignment ambiguous and can change the subjective alignment depending on the offset position, thereby affecting the slope. We also suspect that the variability in perceived alignment will be further exacerbated by the reverse polarity of the features that are being aligned (Mather & Morgan, 1986; Levi & Westheimer, 1987; O'Shea & Mitchell, 1990; Murphy et al., 1988; Levi et al., 1990; Levi & Waugh, 1996).

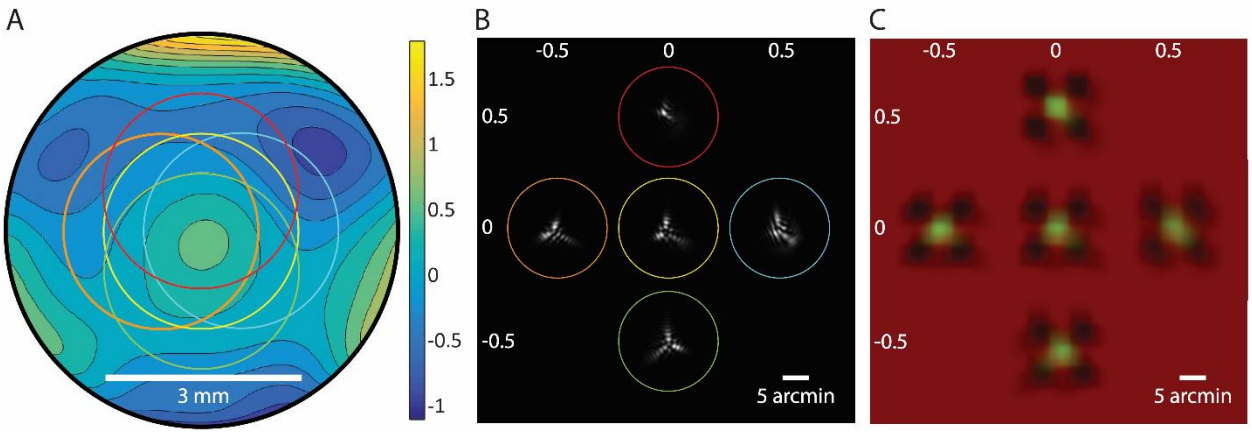

Figure 4.5. Simulations of the appearance of the TCA stimulus as a function of pupil position. A) Model wavefront of a typical eye used for simulations. Units for the color bar are micrometers. Colored circles overlaid on the wavefront image demarcate the area of the pupil which was sampled to generate the PSFs shown in B). Defocus was set to zero for the centered position only (yellow circle). The pupil offsets for each sample relative to the centered position are given in millimeters (mm) along the margins of panels B) and C). C) Simulations of the appearance of the stimulus, generated by convolving the PSFs shown in B) with the aligned stimulus (Figure 1A). Each image represents the stimulus appearance at a different vertical or horizontal pupil offset (units are mm). Note that this does not include the offset between stimuli incurred by chromatic aberration, and thus is representative only of the appearance with monochromatic blur.

To our knowledge, we are the first to report significant differences in TCA with pupil position in different meridians. Previous studies using Vernier stimuli viewed through a pinhole aperture only measured the horizontal component of the TCA offset as a function of pupil displacement (Simonet & Campbell, 1990; Thibos et al., 1990 and 1992). These authors did not directly assess variability between subjects, however their data demonstrate individual differences in slopes for horizontal TCA comparable to those observed here. Privitera et al. (2016) measured TCA offsets for both horizontal and vertical pupil displacements with AOSLO image-based methods, and the small difference between the horizontal and vertical slopes in their subject is consistent with the small variability observed here with the image-based protocol (Table 4.1).

We found an average *m* ratio of 3.86 with image-based methods. This means that a pupil misalignment of only 0.13 mm from the reference position (where TCA is measured at the beginning of an experiment with image-based methods) will displace a stimulus from its targeted retinal location by half an arcmin. This has implications for

single-cone-targeted stimulus delivery where authors are interested in relating behavioral phenomena to single-cone stimulation. Cone photoreceptor spacing at 1-2 deg eccentricity, where these experiments are typically performed, is approximately 1 arcmin, leaving little room for error induced by pupil displacements. To combat this, we have introduced real-time visual and auditory feedback from the pupil tracking plugin to assist the subject in keeping their pupil aligned. We find that in many cases this is sufficient and there is no need for active compensation. However, work done closer to the fovea will demand a higher level of stimulus placement accuracy and a better strategy for TCA compensation, like we demonstrate in Experiment 2. Additionally, TCA compensation would be useful for naïve subjects and particularly clinical populations who may have difficulty maintaining alignment.

In Experiment 2, we used *m* ratios measured for individual subjects in order to compensate for individual differences in TCA offset with pupil displacements. We used a tracking scanning laser ophthalmoscope (TSLO) to demonstrate TCA compensation without correction for monochromatic aberrations, other than defocus. Implementation in an AOSLO would be the same.

4.4 Experiment 2: Real-time Correction for Changes in TCA

4.4.1 Apparatus

The tracking scanning laser ophthalmoscope (TSLO) used in these experiments is described elsewhere (Sheehy et al., 2012), with details specific to these experiments described briefly here. The infrared light source was an 840 nm superluminescent diode (Superlum, Moscow, Russia). A second light source, a diode-pumped solid-state laser (CrystaLaser, Reno, NV) with λ = 532 nm, was aligned so that its beam path was coaligned with the infrared wavelength at a dichroic beam splitter placed before the entrance pupil. Two fiber-coupled acousto-optic modulators (AOMs; Brimrose Corp., Sparks Glencoe, MD) were used to independently modulate the intensities of the light sources. A chinrest and temple pads were mounted on an X, Y, Z stage that the experimenter used to align the subject's pupil to the pupil plane of the system.

Pupil tracking in the TSLO system was the same as described in Experiment 1.

4.4.2 Stimulus

The stimulus configuration was the same as in Experiment 1 (Figure 4.1A), except for the following. The background composed of the 840 nm raster was 3.2 deg (1.56 logTd), reflecting the larger field of view in the TSLO system, and each square was 11.25 arcminutes in length. The target square was composed of 532 nm light (3.06 logTd). Decrement squares were 0.76 logTd.

4.4.3 Procedure

Eight subjects (4 males, 4 females, ages 23-50), none of whom participated in the previous experiment, participated in Experiment 2. Subjects 10003 and 20036 were

authors of this study, the remaining six subjects were naïve to the purposes of the experiment.

Subjects' pupils were dilated and cyclopleged with 1-2 drops of 1% tropicamide ophthalmic solution 15 minutes prior to the experiment. A trial lens was placed at the entrance pupil of the TSLO to correct for defocus when necessary. The experimenter aligned the subject's pupil to be centered with respect to the imaging beam and this was set as the reference pupil position.

Subjects completed 180 trials in each experimental session. Each trial was the same as described in Experiment 1 (4.3.3, Procedure), except that the pupil offsets extended to +/- 0.75 mm of the reference pupil position. Three subjects (20093, 20106, 10003) completed one session and then went on to participate in the compensation task, described in the following paragraph, while the other five subjects completed two sessions without compensation to further assess individual differences in slopes.

To compensate for changes in TCA with pupil displacements, the position of the green (λ = 532 nm) increment square generated by the stimulus channel was updated on each frame by an amount equal and opposite to the predicted TCA offset, inferred from the subject's current pupil position and their previously determined *m* ratio. This was achieved by real-time feedback from the pupil tracker which was used to estimate the current TCA offset by applying the *m* ratio to Equation 4.2. Next, the timing of the green stimulus delivery in the raster scan was updated accordingly by an AOM synchronized with the beam scan, using the same methodology described in detail in (Arathorn et al., 2007; Yang et al., 2010).

On each trial, subjects used a keyboard to align the increment square to be centered relative to the decrement squares. Spatial offsets indicated by the subject were summed with any additional offsets intended to compensate for changes in TCA. Subjects completed 90 trials where compensation was or was not applied. In the no-compensation condition, the position of the increment pattern was updated by the subject's key presses only, and thus was no different from the calibration procedure. Trials were pseudo-randomly interleaved, with 45 in each condition.

4.4.4 Results

Figure 4.6 shows data and fits to Equation 4.2 for three representative subjects. Each data point represents the vertical or horizontal offset the subject required to align the 532 nm target square to the 840 nm decrement pattern, plotted as a function of pupil offset in the respective direction. Each subject's data were fit to Eq. 4.2, where the slopes ($m_{(x, y)}$) represent the change in TCA per unit pupil displacement.

In all eight subjects, the difference in slopes was significantly different between the two pupil meridians ($p < 0.01$). Figure 4.7 shows the log ratios, $\log_{10}(m_x/m_y)$, for all subjects. When $m_x = m_y$, the log ratio is zero (solid line). Additionally, there was between-subject variability in both the magnitude and direction of the anisotropy. In half of our subjects $m_x > m_y$ and the other half had $m_x < m_y$.

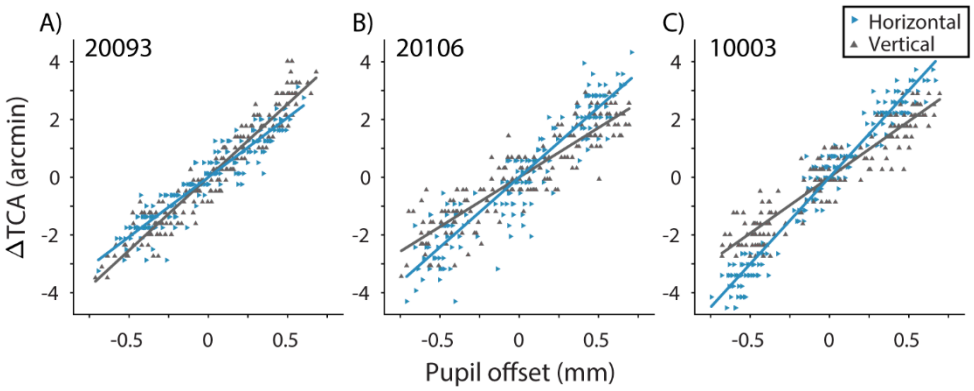

Figure 4.6. Subjective alignments of the stimulus at different pupil positions for three subjects: A) 20093, B) 20106, and C) 10003. Pupil offsets are relative to the reference pupil position at zero. Subjects' alignments are expressed as ΔTCA, the change in TCA offset (λ = 532 and 840 nm) relative to its magnitude at the reference pupil position. Data were fit with ordinary least squares (OLS) regression separately for horizontal (blue rightward triangles) and vertical (gray upward triangles) changes in TCA for horizontal and vertical pupil offsets, respectively.

Data and fits for the compensation condition are shown in Figure 4.8. Following compensation for changes in TCA with pupil displacements, m_x and m_y were not significantly different from zero (20093: $p = 0.55$ for m_x, $p = 0.65$ for m_y; 20106: $p = 0.0055$ for m_x, $p = 1.0$ for m_y; 10003: $p = 0.09$ for m_x, $p = 0.35$ for m_y), except for m_x (the horizontal component of TCA with horizontal pupil displacements) for subject 20106 (Figure 4.8B), which was due to a noisy calibration measurement. Additionally, the within-subject anisotropies in ΔTCA with respect to pupil meridian (Figure 4.7) were no longer observed.

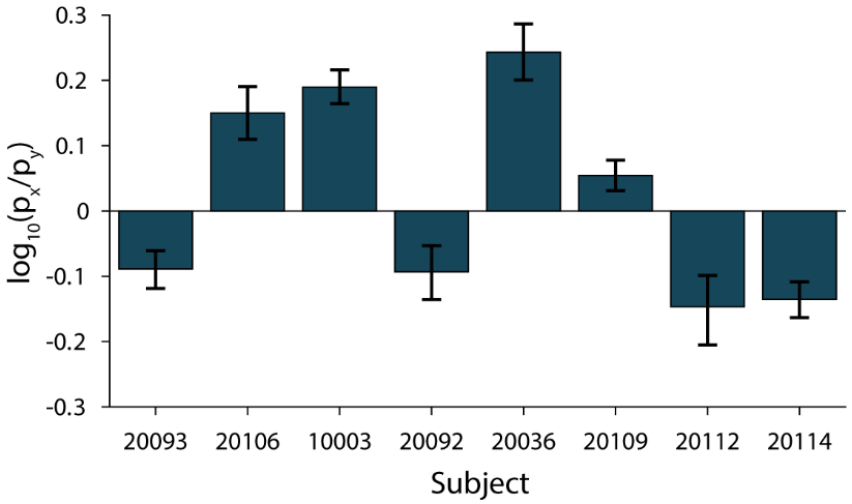

Figure 4.7. Individual differences in anisotropy of m_x and m_y. The log ratio $\log_{10}(m_x/m_y)$, is shown for each subject. When $m_x = m_y$, the log ratio is 0. Points above the line indicate $m_x > m_y$, and below the line $m_x < m_y$. Error bars are 95% bootstrapped confidence intervals.

We also compared the slopes across the no-compensation condition and the initial estimate determined in the calibration procedure. We found that slopes between the two sessions were not statistically different (20093: $p = 0.97$ for m_x, $p = 0.31$ for m_y; 20106: $p = 0.013$ for m_x, $p = 0.81$ for m_y; 10003: $p = 0.46$ for m_x, $p = 0.66$ for m_y), except in the case of m_x in 20106. This suggests that our failure to fully compensate for changes in TCA in this case was likely due to an overestimation of m_x in the calibration procedure.

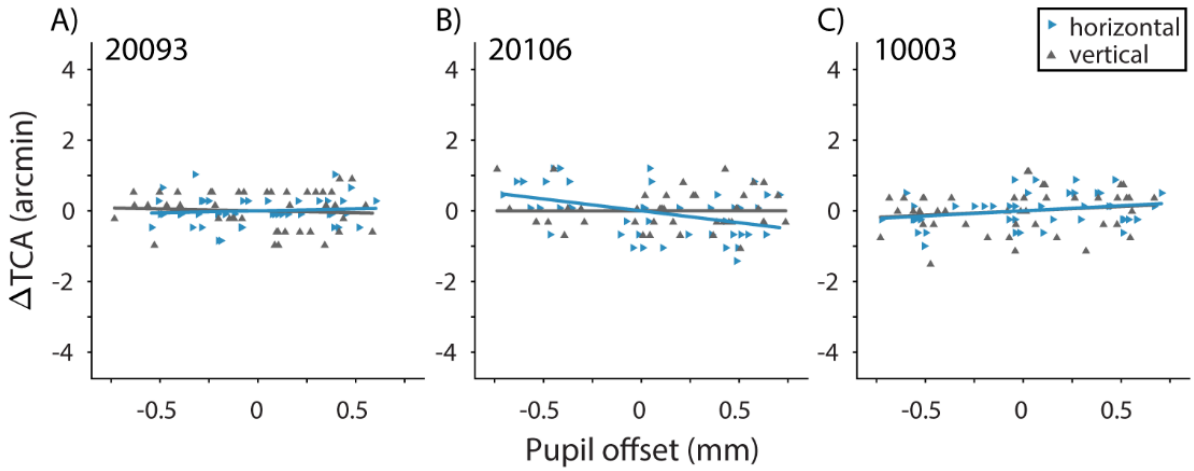

Figure 4.8. Compensation for ΔTCA with pupil displacements. Results are shown for the same subjects as in Figure 4.6. Slopes ($m_{(x, y)}$) for horizontal (blue rightward triangles) and vertical (gray upward triangles) pupil offsets were not significantly different from zero, except for m_x in 20106.

4.4.5 Discussion

In Experiment 2, we used *m* ratios measured for individual subjects in the TSLO in order to compensate for individual differences in TCA offset with pupil displacements without correction for monochromatic aberrations other than defocus. Similar to our results from Experiment 1, we found significant within- and between-subject variability in the slopes of the TCA versus pupil offset functions in all eight subjects.

We used *m* ratios calibrated for individual subjects and both pupil meridians in order to compensate for changes in perceived chromatic offsets with pupil displacements in the TSLO. Perceived changes in TCA with pupil displacements were compensated by a combination of real-time pupil tracking and updating of stimulus delivery. With real-time compensation, slopes of the ΔTCA versus pupil offset function were flattened and there was no longer a systematic relationship between pupil offset and subjects' alignments, except in the case of the horizontal component of TCA for 20106 which was likely due to an overestimation of m_x in the calibration procedure (see 4.4.4 Results). Even in this case, most of the variability in psychophysical alignment due to pupil displacements was removed.

Though we used a TSLO system to demonstrate TCA compensation, implementation in the AOSLO would be effectively the same because both systems are equipped with the same hardware and software components utilized in this technique. However, in AO systems, which correct for monochromatic aberrations across the fully

dilated pupil, our results from Experiment 1 suggest it may be possible to use a single *m* ratio. The small differences between slopes we observed following correction for all aberrations are negligible in the context of TCA compensation, given that foveal cone spacing is approximately 0.5 arcmin (Curcio et al., 1990) and the pupil is unlikely to become displaced by more than a fraction of a millimeter. Overall, these data suggest that a uniform *m* ratio can be used in systems which utilize AO to correct for higher-order aberrations, though a complete characterization of between subject variability will require a larger study.

4.5 Conclusions

In this study we demonstrated that pupil tracking can be used to predict dynamic changes in TCA that occur with small shifts in pupil position. By updating stimulus delivery in accordance with the subjects' pupil position, we successfully compensated for changes in TCA that occurred with pupil offsets (Experiment 2). We found that changes in TCA followed a linear relationship with pupil offset, consistent with previous estimates based on psychophysics (Simonet & Campbell, 1990; Thibos et al., 1990 and 1992) and AOSLO multi-wavelength image analyses (Harmening et al., 2012; Privitera et al., 2016). However, in both experiments we found that there was substantial variability in the slopes of the ΔTCA versus pupil offset functions, both between and within individuals, when monochromatic aberrations were uncorrected, and we propose that much of this variability is due to biases in alignments in the presence of optical blur. In our sample of five subjects, these differences were minimized when all aberrations were corrected, suggesting that in many cases a uniform slope can be used to correct for TCA across subjects in an AOSLO.

4.6 Acknowledgements

The work presented in this chapter was published as a peer-reviewed article in *Biomedical Optics Express* in March 2019. It is reprinted here with permission from the co-authors, Dr. Claudio Privitera, Dr. Brian Schmidt, and Dr. Austin Roorda, who each provided contributions to the conception, design, and implementation of the experiments discussed in this chapter. Additionally, Pavan Tiruveedhula provided much appreciated technical support on this project.

References

Ahmad, K. M., Klug, K., Herr, S., Sterling, P., & Schein, S. (2003). Cell density ratios in a foveal patch in macaque retina. *Visual neuroscience*, *20*(2), 189-209.

Akutsu, H., McGraw, P. V., & Levi, D. M. (1999). Alignment of separated patches: multiple location tags. *Vision Research*, *39*(4), 789-801.

ANSI. (2014). American National Standard for Safe Use of Lasers. ANSI Z136. 1–2014.

Anstis, S. (1989). Kinetic edges become displaced, segregated, and invisible. *Neural mechanisms of visual perception*, *2*, 247-260.

Arathorn, D. W., Yang, Q., Vogel, C. R., Zhang, Y., Tiruveedhula, P., & Roorda, A. (2007). Retinally stabilized cone-targeted stimulus delivery. *Optics express*, *15*(21), 13731-13744.

Atchison, D. A., & Smith, G. (2005). Chromatic dispersions of the ocular media of human eyes. *JOSA A*, *22*(1), 29-37.

Bedford, R. E., & Wyszecki, G. (1957). Axial chromatic aberration of the human eye. *JOSA*, *47*(6), 564-565.

Benjamini, Y., & Hochberg, Y. (1995). Controlling the false discovery rate: a practical and powerful approach to multiple testing. *Journal of the Royal statistical society: series B (Methodological)*, *57*(1), 289-300.

Boehm, A. E., MacLeod, D. I. A., & Bosten, J. M. (2014). Compensation for red-green contrast loss in anomalous trichromats. *Journal of vision*, *14*(13), 19-19.

Boehm, A. E., Privitera, C. M., Schmidt, B. P., & Roorda, A. (2019). Transverse chromatic offsets with pupil displacements in the human eye: Sources of variability and methods for real-time correction. *Biomedical Optics Express*, *10*(4), 1691-1706.

Boehnke, S. E., & Munoz, D. P. (2008). On the importance of the transient visual response in the superior colliculus. *Current opinion in neurobiology*, *18*(6), 544-551.

Boehnke, S. E., Berg, D. J., Marino, R. A., Baldi, P. F., Itti, L., & Munoz, D. P. (2011). Visual adaptation and novelty responses in the superior colliculus. *European Journal of Neuroscience*, *34*(5), 766-779.

Boycott, B. B., & Wässle, H. (1991). Morphological Classification of Bipolar Cells of the Primate Retina. *The European journal of neuroscience*, *3*(11), 1069-1088.

Boynton, R. M., & Kambe, N. (1980). Chromatic difference steps of moderate size measured along theoretically critical axes. *Color Research & Application*, *5*(1), 13-23.

Brainard, D. H., Williams, D. R., & Hofer, H. (2008). Trichromatic reconstruction from the interleaved cone mosaic: Bayesian model and the color appearance of small spots. *Journal of Vision*, *8*(5), 15-15.

Brainard, D. H. (2015). Color and the cone mosaic. *Annual Review of Vision Science*, *1*, 519-546.

Breitmeyer, B., & Julesz, B. (1975). The role of on and off transients in determining the psychophysical spatial frequency response. *Vision Research*, *15*(3), 411-415.

Bruce, K. S., Harmening, W. M., Langston, B. R., Tuten, W. S., Roorda, A., & Sincich, L. C. (2015). Normal perceptual sensitivity arising from weakly reflective cone photoreceptors. *Investigative ophthalmology & visual science*, *56*(8), 4431-4438.

Bruce, K. S. (2016). *Elementary photoreceptor signaling in human vision* (Doctoral dissertation, The University of Alabama at Birmingham).

Calkins, D. J., & Sterling, P. (1996). Absence of spectrally specific lateral inputs to midget ganglion cells in primate retina. *Nature*, *381*(6583), 613.

Calkins, D. J., Tsukamoto, Y., & Sterling, P. (1998). Microcircuitry and mosaic of a blue–yellow ganglion cell in the primate retina. *Journal of Neuroscience*, *18*(9), 3373-3385.

Campbell, M. C., Harrison, E. M., & Simonet, P. (1990). Psychophysical measurement of the blur on the retina due to optical aberrations of the eye. *Vision research*, *30*(11), 1587-1602.

Charman, W. N., & Jennings, J. A. M. (1976). Objective measurements of the longitudinal chromatic aberration of the human eye. *Vision Research*, *16*(9), 999-1005.

Chatterjee, S., & Callaway, E. M. (2003). Parallel colour-opponent pathways to primary visual cortex. *Nature*, *426*(6967), 668.

Clarke, F. J. J. (1961). Visual recovery following local adaptation of the peripheral retina (Troxler's effect). *Optica Acta: International Journal of Optics*, *8*(2), 121-135.

Clarke, F. J. J., & Belcher, S. J. (1962). On the localization of Troxler's effect in the visual pathway. *Vision Research*, *2*(1-4), 53-68.

Clarke, E., & O'Malley, C. D. (1996). *The human brain and spinal cord: A historical study illustrated by writings from antiquity to the twentieth century* (No. 2). Norman Publishing.

Crook, J. D., Manookin, M. B., Packer, O. S., & Dacey, D. M. (2011). Horizontal Cell Feedback without Cone Type-Selective Inhibition Mediates “Red–Green” Color

Opponency in Midget Ganglion Cells of the Primate Retina. *The Journal of Neuroscience*, *31*(5), 1762-1772.

Curcio, C. A., Sloan, K. R., Kalina, R. E., & Hendrickson, A. E. (1990). Human photoreceptor topography. *Journal of comparative neurology*, *292*(4), 497-523.

Curcio, C. A., Allen, K. A., Sloan, K. R., Lerea, C. L., Hurley, J. B., Klock, I. B., & Milam, A. H. (1991). Distribution and morphology of human cone photoreceptors stained with anti-blue opsin. *Journal of Comparative Neurology*, *312*(4), 610-624.

Dacey, D. M., & Petersen, M. R. (1992). Dendritic field size and morphology of midget and parasol ganglion cells of the human retina. *Proceedings of the National Academy of sciences*, *89*(20), 9666-9670.

Dacey, D. M. (1993). The mosaic of midget ganglion cells in the human retina. *Journal of Neuroscience*, *13*(12), 5334-5355.

Dacey, D. M., & Lee, B. B. (1994). The 'blue-on' opponent pathway in primate retina originates from a distinct bistratified ganglion cell type. *Nature*, *367*(6465), 731-735.

Dacey, D. M., Lee, B. B., Stafford, D. K., Pokorny, J., & Smith, V. C. (1996). Horizontal cells of the primate retina: cone specificity without spectral opponency. *Science*, *271*(5249), 656-659.

Dacey, D. M., Wool, L., Packer, O., & Wong, R. (2017). Confirmation of an S-OFF midget ganglion cell pathway using serial block-face scanning electron microscopy. *Journal of Vision*, *17*(7), 58-58.

Dacey, D. M. (2000). Parallel pathways for spectral coding in primate retina. *Annual review of neuroscience*, *23*(1), 743-775.

Dacey, D., Packer, O. S., Diller, L., Brainard, D., Peterson, B., & Lee, B. (2000). Center surround receptive field structure of cone bipolar cells in primate retina. *Vision research*, *40*(14), 1801-1811.

Dacey, D. M. (2018). Discovering visual pathway origins in the center of the human foveola with connectomics. *Investigative Ophthalmology & Visual Science*, *59*(9), 14-14.

Dartnall, H. J., Bowmaker, J. K., & Mollon, J. D. (1983). Human visual pigments: microspectrophotometric results from the eyes of seven persons. *Proceedings of the Royal society of London. Series B. Biological sciences*, *220*(1218), 115-130.

De Monasterio, F. M., & Gouras, P. (1975). Functional properties of ganglion cells of the rhesus monkey retina. *The Journal of physiology*, *251*(1), 167-195.

Delahunt, P. B., Webster, M. A., Ma, L., & Werner, J. S. (2004). Long-term renormalization of chromatic mechanisms following cataract surgery. *Visual neuroscience*, *21*(3), 301-307.

Derrington, A. M., Krauskopf, J., & Lennie, P. (1984). Chromatic mechanisms in lateral geniculate nucleus of macaque. *The Journal of physiology*, *357*(1), 241-265.

De Monasterio, F. M., & Gouras, P. (1975). Functional properties of ganglion cells of the rhesus monkey retina. *The Journal of physiology*, *251*(1), 167-195.

De Valois, R. L., Abramov, I., & Jacobs, G. H. (1966). Analysis of response patterns of LGN cells. *JOSA*, *56*(7), 966-977.

De Valois, R. L., De Valois, K. K., Switkes, E., & Mahon, L. (1997). Hue scaling of isoluminant and cone-specific lights. *Vision research*, *37*(7), 885-897.

De Valois, R. L., De Valois, K. K., & Mahon, L. E. (2000). Contribution of S opponent cells to color appearance. *Proceedings of the National Academy of Sciences*, *97*(1), 512-517.

De Weerd, P., Gattass, R., Desimone, R., & Ungerleider, L. G. (1995). Responses of cells in monkey visual cortex during perceptual filling-in of an artificial scotoma. *Nature*, *377*(6551), 731-734.

Ditchburn, R. W., & Ginsborg, B. L. (1952). Vision with a stabilized retinal image. *Nature*, *170*(4314), 36-37.

Domdei, N., Domdei, L., Reiniger, J. L., Linden, M., Holz, F. G., Roorda, A., & Harmening, W. M. (2018). Ultra-high contrast retinal display system for single photoreceptor psychophysics. *Biomedical optics express*, *9*(1), 157-172.

Drasdo, N. (1977). The neural representation of visual space. *Nature*, *266*(5602), 554-556.

Drasdo, N., Millican, C. L., Katholi, C. R., & Curcio, C. A. (2007). The length of Henle fibers in the human retina and a model of ganglion receptive field density in the visual field. *Vision research*, *47*(22), 2901-2911.

Dreher, A. W., Bille, J. F., & Weinreb, R. N. (1989). Active optical depth resolution improvement of the laser tomographic scanner. *Applied optics*, *28*(4), 804-808.

Duncan, R. O., & Boynton, G. M. (2003). Cortical magnification within human primary visual cortex correlates with acuity thresholds. *Neuron*, *38*(4), 659-671.

Enoch, J. M., & Hope, G. M. (1973). Interferometric resolution determinations in the fovea and parafovea. *Documenta Ophthalmologica*, *34*(1), 143-156.

Famiglietti, E. V., & Kolb, H. (1976). Structural basis for ON-and OFF-center responses in retinal ganglion cells. *Science*, *194*(4261), 193-195.

Fernández, E. J., Unterhuber, A., Prieto, P. M., Hermann, B., Drexler, W., & Artal, P. (2005). Ocular aberrations as a function of wavelength in the near infrared measured with a femtosecond laser. *Optics Express*, *13*(2), 400-409.

Fernández, E. J., Unterhuber, A., Považay, B., Hermann, B., Artal, P., & Drexler, W. (2006). Chromatic aberration correction of the human eye for retinal imaging in the near infrared. *Optics express*, *14*(13), 6213-6225.

Field, G. D., Gauthier, J. L., Sher, A., Greschner, M., Machado, T. A., Jepson, L. H., Shlens, J., Gunning, D. E., Mathieson, K., Dabrowski, W., Paninski, L., Litke, A. M., & Chichilnisky, E. J. (2010). Functional connectivity in the retina at the resolution of photoreceptors. *Nature*, *467*(7316), 673.

Finkelstein, M. A., & Hood, D. C. (1982). Opponent-color cells can influence detection of small, brief lights. *Vision Research*, *22*(1), 89-95.

Finkelstein, M. A., & Hood, D. C. (1984). Detection and discrimination of small, brief lights: variable tuning of opponent channels. *Vision research*, *24*(3), 175-181.

Finkelstein, M. A. (1988). Spectral tuning of opponent channels is spatially dependent. *Color Research & Application*, *13*(2), 106-112.

Friedman, H. S., Zhou, H., & von der Heydt, R. (1999). Color filling-in under steady fixation: Behavioral demonstration in monkeys and humans. *Perception*, *28*(11), 1383-1395.

Frome, F. S., MacLeod, D. I. A., Buck, S. L., & Williams, D. R. (1981). Large loss of visual sensitivity to flashed peripheral targets. *Vision research*, *21*(8), 1323-1328.

Goldberg, M. E., & Wurtz, R. H. (1972). Activity of superior colliculus in behaving monkey. II. Effect of attention on neuronal responses. *Journal of neurophysiology*, *35*(4), 560-574.

Gollisch, T., & Meister, M. (2010). Eye smarter than scientists believed: neural computations in circuits of the retina. Neuron, 65(2), 150-164.

Gordon, J., Abramov, I., & Chan, H. (1994). Describing color appearance: hue and saturation scaling. *Perception & psychophysics*, *56*(1), 27-41.

Green, D. G. (1970). Regional variations in the visual acuity for interference fringes on the retina. *The Journal of physiology*, *207*(2), 351-356.

Grieve, K., Tiruveedhula, P., Zhang, Y., & Roorda, A. (2006). Multi-wavelength imaging with the adaptive optics scanning laser Ophthalmoscope. *Optics express*, *14*(25), 12230-12242.

Guizar-Sicairos, M., Thurman, S. T., & Fienup, J. R. (2008). Efficient subpixel image registration algorithms. Optics letters, 33(2), 156-158.

Hardy, J. W., Lefebvre, J. E., & Koliopoulos, C. L. (1977). Real-time atmospheric compensation. *JOSA*, *67*(3), 360-369.

Harmening, W. M., Tiruveedhula, P., Roorda, A., & Sincich, L. C. (2012). Measurement and correction of transverse chromatic offsets for multi-wavelength retinal microscopy in the living eye. *Biomedical optics express*, *3*(9), 2066-2077.

Harmening, W. M., Tuten, W. S., Roorda, A., & Sincich, L. C. (2014). Mapping the perceptual grain of the human retina. *Journal of Neuroscience*, *34*(16), 5667-5677.

Hartline, H. K. (1938). The response of single optic nerve fibers of the vertebrate eye to illumination of the retina. *American Journal of Physiology-Legacy Content*, *121*(2), 400-415.

Hass, C. A., & Horwitz, G. D. (2013). V1 mechanisms underlying chromatic contrast detection. *Journal of neurophysiology*, *109*(10), 2483-2494.

Hautus, M. J. (1995). Corrections for extreme proportions and their biasing effects on estimated values of d′. Behavior Research Methods, Instruments, & Computers, 27(1), 46-51.

Herr, S., Klug, K., Sterling, P., & Schein, S. (2003). Inner S-cone bipolar cells provide all of the central elements for S cones in macaque retina. *Journal of Comparative Neurology*, *457*(2), 185-201.

Hofer, H., Carroll, J., Neitz, J., Neitz, M., & Williams, D. R. (2005a). Organization of the human trichromatic cone mosaic. *Journal of Neuroscience*, *25*(42), 9669-9679.

Hofer, H., Singer, B., & Williams, D. R. (2005b). Different sensations from cones with the same photopigment. *Journal of Vision*, *5*(5), 5-5.

Hornstein, E. P., Verweij, J., & Schnapf, J. L. (2004). Electrical coupling between red and green cones in primate retina. *Nature neuroscience*, *7*(7), 745.

Horwitz, G. D., Chichilnisky, E. J., & Albright, T. D. (2007). Cone inputs to simple and complex cells in V1 of awake macaque. *Journal of neurophysiology*, *97*(4), 3070-3081.

Horwitz, G. D., & Hass, C. A. (2012). Nonlinear analysis of macaque V1 color tuning reveals cardinal directions for cortical color processing. *Nature neuroscience*, *15*(6), 913.

Hubel, D. H., & Wiesel, T. N. (1959). Receptive fields of single neurones in the cat's striate cortex. *The Journal of physiology*, *148*(3), 574-591.

Hubel, D. H., & Wiesel, T. N. (1961). Integrative action in the cat's lateral geniculate body. *The Journal of Physiology*, *155*(2), 385-398.

Hubel, D. H., & Wiesel, T. N. (1962). Receptive fields, binocular interaction and functional architecture in the cat's visual cortex. *The Journal of physiology*, *160*(1), 106-154.

Hubel, D. H., & Wiesel, T. N. (1965). Receptive fields and functional architecture in two nonstriate visual areas (18 and 19) of the cat. *Journal of neurophysiology*, *28*(2), 229-289.

Hubel, D. H., & Wiesel, T. N. (1968). Receptive fields and functional architecture of monkey striate cortex. *The Journal of physiology*, *195*(1), 215-243.

Hubel, D. H., & Wiesel, T. N. (1972). Laminar and columnar distribution of geniculo-cortical fibers in the macaque monkey. *Journal of Comparative Neurology*, *146*(4), 421-450.

Hyman, L. (2007). Myopic and hyperopic refractive error in adults: an overview. *Ophthalmic epidemiology*, *14*(4), 192.

Johnson, E. N., Hawken, M. J., & Shapley, R. (2004). Cone inputs in macaque primary visual cortex. *Journal of Neurophysiology*, *91*(6), 2501-2514.

Jung, R., & Spillmann, L. (1970). Receptive-field estimation and perceptual integration in human vision. *Early experience and visual information processing in perceptual and reading disorders*, 181-197.

Kalloniatis, M., & Harwerth, R. S. (1991). Effects of chromatic adaptation on opponent interactions in monkey increment-threshold spectral-sensitivity functions. *JOSA A*, *8*(11), 1818-1831.

Kaplan, E. (2004). The M, P, and K pathways of the primate visual system. *The visual neurosciences*, *1*, 481-493.

Kelly, D. H. (1979). Motion and vision. I. Stabilized images of stationary gratings. *JOSA*, *69*(9), 1266-1274.

Kiely, P. M., Smith, G., & Carney, L. G. (1982). The mean shape of the human cornea. *Optica Acta: International Journal of Optics*, *29*(8), 1027-1040.

King-Smith, P. E., & Carden, D. (1976). Luminance and opponent-color contributions to visual detection and adaptation and to temporal and spatial integration. *JOSA*, *66*(7), 709-717.

King-Smith, P. E., Grigsby, S. S., Vingrys, A. J., Benes, S. C., & Supowit, A. (1994). Efficient and unbiased modifications of the QUEST threshold method: theory,

simulations, experimental evaluation and practical implementation. *Vision research*, *34*(7), 885-912.

Kleinbaum, D., Kupper, L., Nizam, A., & Rosenberg, E. (2013). *Applied regression analysis and other multivariable methods*. Nelson Education.

Kling, A., Field, G. D., Brainard, D. H., & Chichilnisky, E. J. (2019). Probing Computation in the Primate Visual System at Single-Cone Resolution. *Annual review of neuroscience*, *42*.

Klug, K., Herr, S., Ngo, I. T., Sterling, P., & Schein, S. (2003). Macaque Retina Contains an S-Cone OFF Midget Pathway. *The Journal of Neuroscience*, *23*(30), 9881-9887.

Kolb, H., & Nelson, R. (1995). The organization of photoreceptor to bipolar synapses in the outer plexiform layer. In *Neurobiology and clinical aspects of the outer retina* (pp. 273-296). Springer, Dordrecht.

Kolb, H., & Marshak, D. (2003). The midget pathways of the primate retina. *Documenta Ophthalmologica*, *106*(1), 67-81.

Kolb, H. (2012, June). Midget pathways of the primate retina underlie resolution and red green color opponency. *Webvision.* Morgan Eye Center. Retrieved from: https://webvision.med.utah.edu/book/part-iii-retinal-circuits/midget-pathways-of-the-primate-retina-underly-resolution/

Kouyama, N., & Marshak, D. W. (1992). Bipolar cells specific for blue cones in the macaque retina. *Journal of Neuroscience*, *12*(4), 1233-1252.

Krauskopf, J., Williams, D. R., & Heeley, D. W. (1982). Cardinal directions of color space. *Vision research*, *22*(9), 1123-1131.

Krauskopf, J., & Gegenfurtner, K. (1992). Color discrimination and adaptation. *Vision research*, *32*(11), 2165-2175.

Kuffler, S. W. (1953). Discharge patterns and functional organization of mammalian retina. *Journal of neurophysiology*, *16*(1), 37-68.

Lee, B. B., Martin, P. R., & Valberg, A. (1989). Sensitivity of macaque retinal ganglion cells to chromatic and luminance flicker. *The Journal of physiology*, *414*(1), 223-243.

Lee, B. B., Pokorny, J., Smith, V. C., Martin, P. R., & Valbergt, A. (1990). Luminance and chromatic modulation sensitivity of macaque ganglion cells and human observers. *JOSA A*, *7*(12), 2223-2236.

Lee, S. C., & Grünert, U. (2007). Connections of diffuse bipolar cells in primate retina are biased against S-cones. *Journal of Comparative Neurology*, *502*(1), 126-140.

Lennie, P., Krauskopf, J., & Sclar, G. (1990). Chromatic mechanisms in striate cortex of macaque. *Journal of Neuroscience*, *10*(2), 649-669.

Lennie, P., Pokorny, J., & Smith, V. C. (1993). Luminance. *JOSA A*, *10*(6), 1283-1293.

Levi, Dennis M., Stanley A. Klein, and A. P. Aitsebaomo. "Vernier acuity, crowding and cortical magnification." *Vision research* 25.7 (1985): 963-977.

Levi, D. M., & Westheimer, G. (1987). Spatial-interval discrimination in the human fovea: what delimits the interval?. *JOSA A*, *4*(7), 1304-1313.

Levi, D. M., Bai-Chuan, J., & Klein, S. A. (1990). Spatial interval discrimination with blurred lines: Black and white are separate but not equal at multiple spatial scales. *Vision Research*, *30*(11), 1735-1750.

Levi, D. M., & Waugh, S. J. (1996). Position acuity with opposite-contrast polarity features: evidence for a nonlinear collector mechanism for position acuity?. *Vision Research*, *36*(4), 573-588.

Levi, D.M. Visual Crowding. In: The Visual Neurosciences. Second Edition. Werner, J. S. & Chalupa, L.M., Eds. M.I.T. Press, 2013.

Li, P. H., Field, G. D., Greschner, M., Ahn, D., Gunning, D. E., Mathieson, K., Sher, A., Litke, A. M., & Chichilnisky, E. J. (2014). Retinal representation of the elementary visual signal. *Neuron*, *81*(1), 130-139.

Liang, J., & Williams, D. R. (1997). Aberrations and retinal image quality of the normal human eye. *JOSA A*, *14*(11), 2873-2883.

Liang, J., Williams, D. R., & Miller, D. T. (1997). Supernormal vision and high-resolution retinal imaging through adaptive optics. *JOSA A*, *14*(11), 2884-2892.

MacLeod, D. I., & Boynton, R. M. (1979). Chromaticity diagram showing cone excitation by stimuli of equal luminance. *JOSA*, *69*(8), 1183-1186.

MacLeod D. I. A. (2003). Colour discrimination, colour constancy, and natural scene statistics (the Verriest lecture). In Mollon J. D. Pokorny J. Knoblauch K. (Eds.), *Normal and defective colour vision* (pp. 189–218). Oxford, UK: Oxford University Press.

Marcos, S., Burns, S. A., Moreno-Barriusop, E., & Navarro, R. (1999). A new approach to the study of ocular chromatic aberrations. *Vision Research*, *39*(26), 4309-4323.

Marcos, S., Burns, S. A., Prieto, P. M., Navarro, R., & Baraibar, B. (2001). Investigating sources of variability of monochromatic and transverse chromatic aberrations across eyes. *Vision research*, *41*(28), 3861-3871.

Mariani, A. P. (1984). Bipolar cells in monkey retina selective for the cones likely to be blue-sensitive. *Nature*, *308*(5955), 184.

Martinez-Conde, S., Macknik, S. L., & Hubel, D. H. (2004). The role of fixational eye movements in visual perception. *Nature reviews neuroscience*, *5*(3), 229.

Martinez-Conde, S., Macknik, S. L., Troncoso, X. G., & Dyar, T. A. (2006). Microsaccades counteract visual fading during fixation. *Neuron*, *49*(2), 297-305.

Massey, S. C. (2008). Circuit functions of gap junctions in mammalian retina. In: R. Masland & T.D. Albright (Eds), *The Senses: a Comprehensive Reference.* (457-472). San Diego, CA: Academic Press.

Mather, G., & Morgan, M. (1986). Irradiation: Implications for theories of edge localization. *Vision Research*, *26*(6), 1007-1015.

McMahon, M. J., Lankheet, M. J., Lennie, P., & Williams, D. R. (2000). Fine structure of parvocellular receptive fields in the primate fovea revealed by laser interferometry. *Journal of Neuroscience*, *20*(5), 2043-2053.

Merigan, W. H., Byrne, C. E., & Maunsell, J. H. (1991). Does primate motion perception depend on the magnocellular pathway?. *Journal of Neuroscience*, *11*(11), 3422-3429.

Miyahara, E., Smith, V. C., & Pokorny, J. (1993). How surrounds affect chromaticity discrimination. *JOSA A, 10*(4), 545-553.

Morgan, M. J., Hole, G. J., & Glennerster, A. (1990). Biases and sensitivities in geometrical illusions. *Vision research*, *30*(11), 1793-1810.

Müller, J. P. (1844). *Handbuch der Physiologie des Menschen: für Vorlesungen. Bd. 1* (Vol. 2). J. Hölscher.

Mulligan, J. (1998). Recovery of motion parameters from distortions in scanned images. In *NASA Conference Publication* (pp. 281-292). NASA.

Murphy, K. M., Jones, D. G., & Van Sluyters, R. C. (1988). Vernier acuity for an opposite contrast stimulus. *Investigative Ophthalmology and Visual Science*, *29*, 138.

Neri, P., & Levi, D. M. (2006). Receptive versus perceptive fields from the reverse-correlation viewpoint. *Vision research*, *46*(16), 2465-2474.

O'Brien, J. J., Chen, X., MacLeish, P. R., & Massey, S. C. (2004). Connexin 36 forms gap junctions between telodendria of primate cones. *Investigative Ophthalmology & Visual Science*, *45*(13), 1146-1146.

Ogboso, Y. U., & Bedell, H. E. (1987). Magnitude of lateral chromatic aberration across the retina of the human eye. *JOSA A*, *4*(8), 1666-1672.

O'Shea, R. P., & Mitchell, D. E. (1990). Vernier acuity with opposite-contrast stimuli. *Perception*, *19*(2), 207-221.

Platt, B. C., & Shack, R. (2001). History and principles of Shack-Hartmann wavefront sensing. *Journal of refractive surgery*, *17*(5), S573-S577.

Poletti, M., Listorti, C., & Rucci, M. (2013). Microscopic eye movements compensate for nonhomogeneous vision within the fovea. *Current Biology*, *23*(17), 1691-1695.

Prins, N & Kingdom, F. A. A. (2018) Applying the Model-Comparison Approach to Test Specific Research Hypotheses in Psychophysical Research Using the Palamedes Toolbox. Frontiers in Psychology, 9:1250. doi: 10.3389/fpsyg.2018.01250

Privitera, C. M., Sabesan, R., Winter, S., Tiruveedhula, P., & Roorda, A. (2016). Eye-tracking technology for real-time monitoring of transverse chromatic aberration. *Optics letters*, *41*(8), 1728-1731.

Putnam, N. M., Hofer, H. J., Doble, N., Chen, L., Carroll, J., & Williams, D. R. (2005). The locus of fixation and the foveal cone mosaic. *Journal of Vision*, *5*(7), 632-639.

Ramachandran, V. S., & Gregory, R. L. (1991). Perceptual filling in of artificially induced scotomas in human vision. *Nature*, *350*(6320), 699.

Ramachandran, V. S., Gregory, R. L., & Aiken, W. (1993). Perceptual fading of visual texture borders. *Vision research*, *33*(5-6), 717-721.

Ratnam, K., Domdei, N., Harmening, W. M., & Roorda, A. (2017). Benefits of retinal image motion at the limits of spatial vision. *Journal of vision*, *17*(1), 30-30.

Read, S. A., Collins, M. J., & Carney, L. G. (2007). A review of astigmatism and its possible genesis. *Clinical and Experimental Optometry*, *90*(1), 5-19.

Regan, B. C., & Mollon, J. D. (1997). The relative salience of the cardinal axes of colour space in normal and anomalous trichromats. In *Colour vision deficiencies XIII* (pp. 261-270). Springer, Dordrecht.

Rhoades, C. E., Shah, N. P., Manookin, M. B., Brackbill, N., Kling, A., Goetz, G., Sher, A., Litke, A. M., & Chichilnisky, E. J. (2018). Unusual physiological properties of two ganglion cell types in primate retina. *bioRxiv*, 496455.

Riggs, L. A., Ratliff, F., Cornsweet, J. C., & Cornsweet, T. N. (1953). The disappearance of steadily fixated visual test objects. *JOSA*, *43*(6), 495-501.

Roorda, A., & Williams, D. R. (1999). The arrangement of the three cone classes in the living human eye. *Nature*, *397*(6719), 520.

Roorda, A., Romero-Borja, F., Donnelly III, W. J., Queener, H., Hebert, T. J., & Campbell, M. C. (2002). Adaptive optics scanning laser ophthalmoscopy. *Optics express*, *10*(9), 405-412.

Rushton, W. A. H. (1965). Cone pigment kinetics in the deuteranope. *The Journal of physiology*, *176*(1), 38-45.

Rushton, W. A. H., & Henry, G. H. (1968). Bleaching and regeneration of cone pigments in man. *Vision research*, *8*(6), 617-631.

Rushton, W. A. H. (1972). Review lecture. Pigments and signals in colour vision. *The Journal of physiology*, *220*(3), 1-31.

Rynders, M., Lidkea, B., Chisholm, W., & Thibos, L. N. (1995). Statistical distribution of foveal transverse chromatic aberration, pupil centration, and angle ψ in a population of young adult eyes. *JOSA A*, *12*(10), 2348-2357.

Sabesan, R., Hofer, H., & Roorda, A. (2015). Characterizing the human cone photoreceptor mosaic via dynamic photopigment densitometry. *PloS one*, *10*(12), e0144891.

Sabesan, R., Schmidt, B. P., Tuten, W. S., & Roorda, A. (2016). The elementary representation of spatial and color vision in the human retina. *Science advances*, *2*(9), e1600797.

Sakaguchi, Y. (2001). Target/surround asymmetry in perceptual filling-in. *Vision Research*, *41*(16), 2065-2077.

Sakaguchi, Y. (2006). Contrast dependency in perceptual filling-in. *Vision research*, *46*(20), 3304-3312.

Schieting, S., & Spillmann, L. (1987). Flicker adaptation in the peripheral retina. *Vision research*, *27*(2), 277-284.

Schiller, P. H., Malpeli, J. G., & Schein, S. J. (1979). Composition of geniculostriate input ot superior colliculus of the rhesus monkey. *journal of Neurophysiology*, *42*(4), 1124-1133.

Schiller, P. H. (1992). The ON and OFF channels of the visual system. *Trends in neurosciences*, *15*(3), 86-92.

Schmidt, B. P., Boehm, A. E., Foote, K. G., & Roorda, A. (2018a). The spectral identity of foveal cones is preserved in hue perception. *Journal of vision*, *18*(11), 19.

Schmidt, B. P., Sabesan, R., Tuten, W. S., Neitz, J., & Roorda, A. (2018b). Sensations from a single M-cone depend on the activity of surrounding S-cones. *Scientific reports*, *8*(1), 8561.

Schmidt, B., Boehm, A. E., Tuten, W. S., & Roorda, A. (2019). Spatial summation of individual cones in human color vision. *BioRxiv*, 521492.

Shapley, R., & Perry, V. H. (1986). Cat and monkey retinal ganglion cells and their visual functional roles. *Trends in Neurosciences*, *9*, 229-235.

Shapley, R. (1990). Visual sensitivity and parallel retinocortical channels. *Annual review of psychology*, *41*(1), 635-658.

Sheehy, C. K., Yang, Q., Arathorn, D. W., Tiruveedhula, P., de Boer, J. F., & Roorda, A. (2012). High-speed, image-based eye tracking with a scanning laser ophthalmoscope. *Biomedical optics express*, *3*(10), 2611-2622.

Simonet, P., & Campbell, M. C. (1990). The optical transverse chromatic aberration on the fovea of the human eye. *Vision research*, *30*(2), 187-206.

Simons, D., Lleras, A., Martinez-Conde, S., Slichter, D., Caddigan, E., & Nevarez, G. (2006). Induced visual fading of complex images. *Journal of Vision*, *6*(10), 1093-1101.

Sincich, L. C., Zhang, Y., Tiruveedhula, P., Horton, J. C., & Roorda, A. (2009). Resolving single cone inputs to visual receptive fields. *Nature neuroscience*, *12*(8), 967-969.

Smith, V. C., & Pokorny, J. (1975). Spectral sensitivity of the foveal cone photopigments between 400 and 500 nm. *Vision research*, *15*(2), 161-171.

Smith, V. C., & Pokorny, J. (1995). Chromatic-discrimination axes, CRT phosphor spectra, and individual variation in color vision. *Journal of the Optical Society of America. A, Optics, image science, and vision*, *12*(1), 27-35.

Smith, A. T., Singh, K. D., Williams, A. L., & Greenlee, M. W. (2001). Estimating receptive field size from fMRI data in human striate and extrastriate visual cortex. *Cerebral cortex*, *11*(12), 1182-1190.

Spillmann, L., Ransom-Hogg, A., & Oehler, R. (1987). A comparison of perceptive and receptive fields in man and monkey. *Human neurobiology*.

Spillmann, L., & Kurtenbach, A. (1992). Dynamic noise backgrounds facilitate target fading. *Vision research*, *32*(10), 1941-1946.

Spillmann, L., & Werner, J. S. (1996). Long-range interactions in visual perception. *Trends in neurosciences*, *19*(10), 428-434.

Stevenson, S. B., Roorda, A., & Kumar, G. (2010, March). Eye tracking with the adaptive optics scanning laser ophthalmoscope. In *Proceedings of the 2010 symposium on eye-tracking research & applications* (pp. 195-198). ACM.

Stockman, A., MacLeod, D. I., & Johnson, N. E. (1993). Spectral sensitivities of the human cones. *JOSA A*, *10*(12), 2491-2521.

Stockman, A., Sharpe, L. T., & Fach, C. C. (1999). The spectral sensitivity of the human short-wavelength sensitive cones derived from thresholds and color matches. *Vision Research, 39,* 2901-2927.

Stockman, A., & Sharpe, L. T. (2000). Spectral sensitivities of the middle- and long-wavelength sensitive cones derived from measurements in observers of known genotype. *Vision Research*, *40,* 1711-1737.

Thibos, L. N., Cheney, F. E., & Walsh, D. J. (1987a). Retinal limits to the detection and resolution of gratings. *JOSA A*, *4*(8), 1524-1529.

Thibos, L. N., Walsh, D. J., & Cheney, F. E. (1987b). Vision beyond the resolution limit: aliasing in the periphery. *Vision Research*, *27*(12), 2193-2197.

Thibos, L. N., Bradley, A., Still, D. L., Zhang, X., & Howarth, P. A. (1990). Theory and measurement of ocular chromatic aberration. *Vision research*, *30*(1), 33-49.

Thibos, L. N., Ye, M., Zhang, X., & Bradley, A. (1992). The chromatic eye: a new reduced-eye model of ocular chromatic aberration in humans. *Applied optics*, *31*(19), 3594-3600.

Troxler D. Ueber das Verschwinden gegebener Gegenstände innerhalb unseres Gesichtskreises. In: Himly K, Schmidt JA, Jena JA, editors. Ophthalmolgische Bibliothek II, 1804:1–119.

Tsukamoto, Y., Masarachia, P., Schein, S. J., & Sterling, P. (1992). Gap junctions between the pedicles of macaque foveal cones. *Vision research*, *32*(10), 1809-1815.

Tuten, W. S., Tiruveedhula, P., & Roorda, A. (2012). Adaptive optics scanning laser ophthalmoscope-based microperimetry. *Optometry and Vision Science*, *89*(5), 563-574.

Tuten, W. S., Harmening, W. M., Sabesan, R., Roorda, A., & Sincich, L. C. (2017). Spatiochromatic interactions between individual cone photoreceptors in the human retina. *Journal of Neuroscience*, *37*(39), 9498-9509.

Vinas, M., Dorronsoro, C., Cortes, D., Pascual, D., & Marcos, S. (2015). Longitudinal chromatic aberration of the human eye in the visible and near infrared from wavefront sensing, double-pass and psychophysics. *Biomedical optics express*, *6*(3), 948-962.

Vogel, C. R., Arathorn, D. W., Roorda, A., & Parker, A. (2006). Retinal motion estimation in adaptive optics scanning laser ophthalmoscopy. *Optics express*, *14*(2), 487-497.

Volbrecht, V. J., Shrago, E. E., Schefrin, B. E., & Werner, J. S. (2000). Spatial summation in human cone mechanisms from 0° to 20° in the superior retina. *JOSA A*, *17*(3), 641-650.

von der Twer, T., & MacLeod, D. I. (2001). Optimal nonlinear codes for the perception of natural colours. *Network: Computation in Neural Systems*, *12*(3), 395-407.

Wald, G., & Griffin, D. R. (1947). The change in refractive power of the human eye in dim and bright light. *JOSA*, *37*(5), 321-336.

Wang, Q., Tuten, W. S., Lujan, B. J., Holland, J., Bernstein, P. S., Schwartz, S. D., Duncan, J. L., & Roorda, A. (2015). Adaptive optics microperimetry and OCT images show preserved function and recovery of cone visibility in macular telangiectasia type 2 retinal lesions. *Investigative ophthalmology & visual science*, *56*(2), 778-786.

Watson, A. B., & Pelli, D. G. (1983). QUEST: A Bayesian adaptive psychometric method. *Perception & psychophysics*, *33*(2), 113-120.

Webb, R. H., Hughes, G. W., & Pomerantzeff, O. (1980). Flying spot TV ophthalmoscope. *Applied optics*, *19*(17), 2991-2997.

Webb, R. H., & Hughes, G. W. (1981). Scanning laser ophthalmoscope. *IEEE Transactions on Biomedical Engineering*, (7), 488-492.

Webb, R. H., Hughes, G. W., & Delori, F. C. (1987). Confocal scanning laser ophthalmoscope. *Applied optics*, *26*(8), 1492-1499.

Webster, M. A., & Mollon, J. D. (1994). The influence of contrast adaptation on color appearance. *Vision research*, *34*(15), 1993-2020.

Webster, M. A., & Mollon, J. D. (1995). Colour constancy influenced by contrast adaptation. *Nature*, *373*(6516), 694.

Webster, M. A., & Wilson, J. A. (2000). Interactions between chromatic adaptation and contrast adaptation in color appearance. *Vision research*, *40*(28), 3801-3816.

Webster, M. A. (2011). Adaptation and visual coding. *Journal of vision*, *11*(5), 3-3.

Webvision, http://webvision.med.utah.edu/, Creative Commons License: Attribution, Noncommercial 4.0 International (CC BY-NC).

Welchman, A. E., & Harris, J. M. (2001). Filling-in the details on perceptual fading. *Vision research*, *41*(16), 2107-2117.

Werner, J. S., & Schefrin, B. E. (1993). Loci of achromatic points throughout the life span. *Josa a*, *10*(7), 1509-1516.

Wilkinson, M. O., Anderson, R. S., Bradley, A., & Thibos, L. N. (2016). Neural bandwidth of veridical perception across the visual field. *Journal of vision*, *16*(2), 1-1.

Williams, D. R. (1985a). Aliasing in human foveal vision. *Vision research*, *25*(2), 195-205.

Williams, D. R. (1985b). Visibility of interference fringes near the resolution limit. *JOSA A*, *2*(7), 1087-1093.

Williams, D. R., & Coletta, N. J. (1987). Cone spacing and the visual resolution limit. JOSA A, 4(8), 1514-1523.

Whitaker, D., McGraw, P. V., Pacey, I., & Barrett, B. T. (1996). Centroid analysis predicts visual localization of first-and second-order stimuli. *Vision Research*, *36*(18), 2957-2970.

White, B. J., Boehnke, S. E., Marino, R. A., Itti, L., & Munoz, D. P. (2009). Color-related signals in the primate superior colliculus. *Journal of Neuroscience*, *29*(39), 12159-12166.

Wickens, T. D. (2002). Elementary signal detection theory. Oxford University Press, USA.

Winter, S., Sabesan, R., Tiruveedhula, P., Privitera, C., Unsbo, P., Lundström, L., & Roorda, A. (2016). Transverse chromatic aberration across the visual field of the human eye. *Journal of vision*, *16*(14), 9-9.

Woods, E. J., & Frost, B. J. (1977). Adaptation and habituation characteristics of tectal neurons in the pigeon. *Experimental brain research*, *27*(3-4), 347-354.

Wool, L. E., Packer, O., Zaidi, Q., & Dacey, D. M. (2018). Short-wavelength cone signals contribute to sparse, high-dimensional color tuning in primate OFF midget ganglion cells. *bioRxiv*, 482653.

Yang, Q., Arathorn, D. W., Tiruveedhula, P., Vogel, C. R., & Roorda, A. (2010). Design of an integrated hardware interface for AOSLO image capture and cone-targeted stimulus delivery. *Optics express*, *18*(17), 17841-17858.

Yarbus, A. L. (1954). Research on the laws of eye movement in vision. In *Dokl. Akad. Nauk. SSSR* (Vol. 96, pp. 733-735).

Yarbus, A. L. (1967). Eye movements during perception of complex objects. In *Eye movements and vision* (pp. 171-211). Springer, Boston, MA.

Yeh, T., Pokorny, J., & Smith, V. C. (1993). Chromatic discrimination with variation in chromaticity and luminance: data and theory. *Vision research*, *33*(13), 1835-1845.

Yoon, G. Y., & Williams, D. R. (2002). Visual performance after correcting the monochromatic and chromatic aberrations of the eye. *JOSA A*, *19*(2), 266-275.